DEGRADATION OF PHASE TRANSFORMING SMA IN PRESENCE OF A CORROSIVE ENVIRONMENT AND THERMOMECHANICAL LOADS

A Dissertation

by

MAHDI MOHAJERI

Submitted to the Office of Graduate and Professional Studies of
Texas A&M University
in partial fulfillment of the requirements for the degree of

DOCTOR OF PHILOSOPHY

Chair of Committee,	Homero Castaneda-Lopez
Co-Chair of Committee,	Dimitris C. Lagoudas
Committee Members,	Raymundo Case
	Ibrahim Karaman
Head of Department,	Ibrahim Karaman

May 2020

Major Subject: Materials Science and Engineering

ABSTRACT

Shape memory alloys (SMAs) are in class of active materials with the capability to undergo and recover large deformations upon subjecting to certain external stimuli, i.e. temperature and mechanical load. This capability has roots in the martensitic transformation, a solid-to-solid, diffusion-less phase transformation between austenite and martensite. Studying the failure mechanisms in SMAs is rather challenging because of the effect of phase transformation/detwinning and the inherent thermo-mechanical coupling, and there has been a recent interest in investigating the effect of aforementioned phenomena on failure of SMAs. Newer challenges in environmental conditions leads the effort for corrosion assessment and study the parameters influencing metallic degradation. The purpose of these studies was to provide a detailed understanding of Nitinol phases and their effects on corrosion behavior of NiTi SMAs.

In this study, corrosion behavior of NiTi SMAs undergoing detwinning/reorientation, martensitic phase transformation, and in presence of cyclic loadings are investigated using mechano-electrochemical techniques. Uniaxial tensile tests were conducted to determine the mechanical properties such as elongation, ultimate tensile strength, modulus, transformation strain, and plateau stress. Electrochemical corrosion behavior of each phase was investigated using cyclic potentiodyamic polarization, electrochemical impedance spectroscopy, Electrochemical frequency modulation techniques. The mechano-electrochemical experimental techniques coupled with imaging and high-resolution surface analysis helped to quantify parameters

describing the passive-active state properties. The relationship of constant load vs. interfacial characterization gave important insight for understanding SMA performance in a corrosive environment.

DEDICATION

To My Lovely Parents & Teal,

ACKNOWLEDGEMENTS

I would like to express great appreciation to my committee chair, Dr. Castaneda Lopez, for his guidance, vision and support throughout the course of my PhD work. I express my special thanks to him for reviewing the research manuscripts and providing constructive comments and criticism during the past years. He taught me the essentials of critical thinking and scientific research throughout my PhD experience. I would also like to give gratitude to my committee co. chair, Dr. Dimitris Lagoudas. His continued guidance throughout the project was very encouraging. Without his exceptional research abilities and positive outlook this thesis would not have been possible. My gratitude is extended to my dissertation committee members, Dr. Raymundo Case, Dr. Ibrahim Karaman and Dr. Nikolaos Michailidis for their willingness to participate in his process and provided invaluable support and encouragement.

In addition, I would like to thank Behrouz Haghgouyan for his many ontributions and Nitinol expertise involving shape memory alloy material properties. Along with Dr. Ahmad Ivan Karaman, whose localized corrosion experience and direction allowed the tests to be successful.

I would like to thank all my colleagues, fellow students, professors and staff at the materials science and engineering department at Texas A& University for creating a positive and nurturing educational environment. Graduate school at Texas A&M has been the most rewarding and unforgettable experience of my life, and I wholeheartedly thank

all the people who made it possible Finally, thanks to my partner (Teal) for her patience and love.

CONTRIBUTORS AND FUNDING SOURCES

Contributors

This work was supervised by a thesis committee consisting of Professor Homero Castaneda Lopez of the Department of Materials Science and Engineering and Professor Dimitris C. Lagoudas of the Department of Aerospace Engineering.

The analyses depicted in Chapter 3 on Microcapillary corrosion were conducted in part by Dr. Ivan Ahmad Karayan and Lucas Nash of the Department of Materials Science and Engineering.

All other work conducted for the dissertation was completed by the student independently.

Funding Sources

This work was made possible in part by Baker Hughes a GE company Grant.

NOMENCLATURE

SMA	Shape Memory Alloy
M_s	Martensitic start temperature
M_f	Martensitic finish temperature
A_s	Austenitic start temperature
A_f	Austenitic finish temperature
M_d	Temperature above which austenite plastically deforms without forward transformation
PE	Pesudo-Elasticity
SE	Super-Elasticity
SME	Shape Memory Effect
DSC	Differential Scanning Calorimeter
EDM	Electrical Discharge Machining
OCP	Open Circuit Potential
LPR	Linear Polarization Resistance
EIS	Electrochemical Impedance Spectroscopy
AC	Alternating Current
SEM	Scanning Electron Microscope
DIC	Digital image correlation
EFM	Electrochemical Frequency Modulation
R_p	polarization resistance
CPE	Constant Phase Element

R_{pore}	Pore Resistance
$R_{electrolyte}$	Electrolyte Resistance
$R_{polarization\ resistance}$	Resistance representing the charge transfer process
ε_0	Permittivity of free space
c_{ox}	Capacitance of the oxide layer
SCE	Saturated Calomel Electrode
i_{corr}	Corrosion current density or corrosion rate
E_b	Breakdown potential
E_a^A	Energy of corrosion reaction for austenite phase
E_a^M	Energy of corrosion reaction for Martensite phase
EEC	Electrical Equivalent Circuit
W_d	Warburg impedance

TABLE OF CONTENTS

LIST OF FIGURES

Page

LIST OF TABLES

Page

1. INTRODUCTION

1.1 Shape Memory Alloys Behavior and Applications

Shape memory alloys (SMAs) represent a unique class of materials with the ability to retain their previous form upon subjected to certain stimulus. Anny Olander discovered the solid phase transformation in SMA discovered. She determined the Gold-Cadmium (Au-Al) alloys capability to plastically deform at low temperature and recovered the original configuration upon subjected to heat. William Buehler discovered the NiTi alloy and its potential for commercial application became available by William Buehler and Frederick Wang.

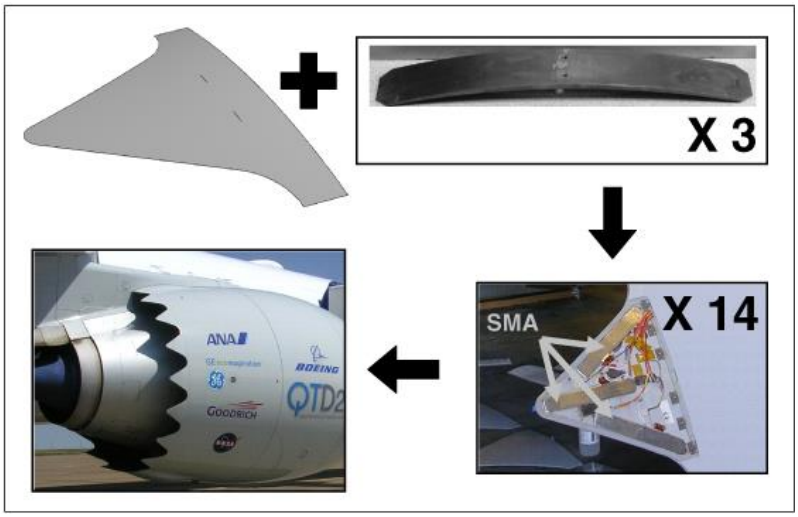

Figure 1.1 Structural configuration of the Boeing Variable Geometry Chevron (from figure 1 of [1], reprinted with permission of IOP Publishing Ltd, DOI: 10.1088/0964-1726/19/1/015020).

The first successful application of SMAs was as pipe coupler in F-14 fighter aircraft. Since then, the engineering and technical applications of NiTi alloys have developed in many commercial fields due to greater demands for lighter and more compact actuator [2, 3]. Some notable engineering applications of SMAs are a variable geometry chevron (VGC) in aerospace application (Figure 1.1) to reduce noise during take-off, a prosthetic hand powered by SMA actuators in robotic application (Figure 1.2) to actuate the robotic finger, and active catheter in biomedical application (Figure 1.2) to enable novel diagnosis and therapy with capability to move with larger bending angles[1, 4].

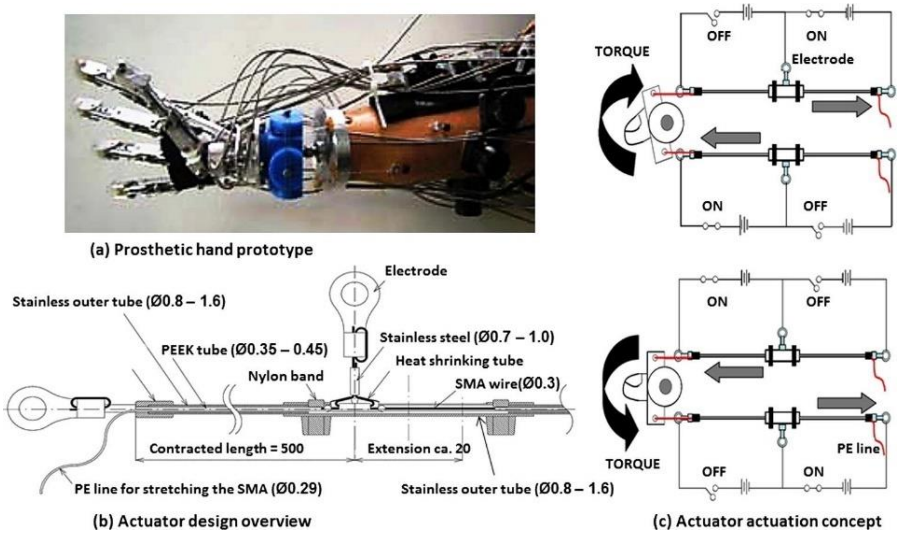

Figure 1.2 (a)The prosthetic hand actuated by heavy and noisy servo motors, (b) design actuator based on SMA to replace the servo motors, and (c) concept for the application of SMA actuator in the actuation of the robotic finger (from figure 16 of [3], ©2013 Elsevier Ltd, reprinted with permission of Elsevier, DOI: 10.1016/j.matdes.2013.11.084).

SMAs can exist in two different phases with a different crystal structure. The stable phase at high temperature called austenite (A) and the stable phase at low temperature called martensite (M). The martensite structure is softer and has a much lower Young's modulus; whereas the austenite phase is relatively hard. The transformation from one structure to the other structure is diffusion-less and proceeds by cooperative movements of the atoms due to shear lattice distortion. This transformation is known as martensitic transformation is a first order solid to solid phase transformation[5]. Martensite phase can have two different crystal structures formed either by combination of "self-

accommodated" martensitic variant (twinned martensite - M_t) or by assembly of a dominant specific variant (detwinned or reoriented martensite - M_d). M_d is the highest temperature that martensite phase can no longer be stress induced and above that material is permanently deformed. When a SMA is heated from the martensitic phase, it begins to transform from martensitic phase into the austenite phase (reverse transformation). Upon cooling the material in the absence of an applied load, it begins to transform from austenite into the martensite phase. This phase transition from austenite to martensite is known as forward transformation. There four characteristic temperature associated with forward and reverse martensitic transformation. The austenite start temperature (A_s) is the temperature where the reverse transformation starts, and the austenite finish temperature (M_f) is the temperature where the reverse transformation is complete. Upon heating a SMA beyond As, it begins to contract and transform into austenite phase and recover into its original shape. The martensite start temperature (M_s) is the temperature where the forward transformation starts. At this temperature, the austenite phase under zero load begins to transform to twinned martensite. The martensite finish temperature (M_f) is the temperature where the forward transformation is complete. At this temperature, under zero load, the material is fully twinned martensite.

These transformations phenomenon and shape change effects are known as the Shape Memory Effect (SME) and can be categorized as follows (Figure 1.1Figure 1.3):

1. One-way shape memory effect: The material has been detwinned by applying an external mechanical load, and then unloaded while at a temperature below

A_s to retain a deformed state. The material recovers its original shape upon heating and transforming back into the parent austenitic phase.

2. Two-way shape memory effect or reversible SME: a two-way SMA can exhibit repeatable shape changes under no applied mechanical load at both high and low temperatures. SMA material with Two-way shape memory effect require the training which material needs to undergo repeated thermomechanical cycling along a specific loading path.
3. Pesudo-elasticity (PE) or Super-elasticity (SE): This behavior is associated with stress generation during mechanical loading and subsequent strain recovery after unloading at temperatures above A_f without any thermal activation. A pseudo-elastic thermomechanical loading path is at temperatures between A_f and M_d. The path starts at the temperature that stable austenite exists and then develops under an applied mechanical load to the state of stable detwinned martensite. Finally, the path returns to the austenitic phase after unloading.

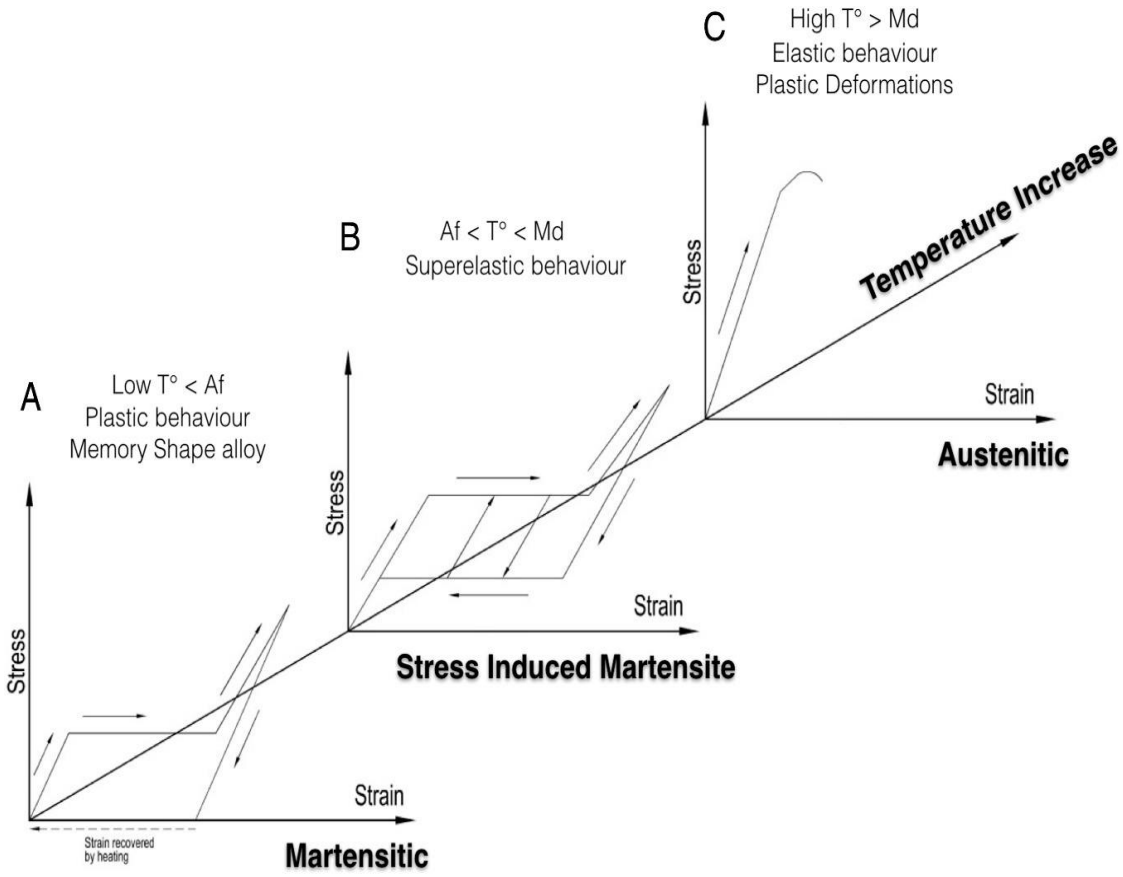

Figure 1.3 A schematic illustrates the variation of the stress-strain curve for an NiTi SMA. From left to right, the environmental temperature is increasing. (A) at the temperature lower than Af, NiTi has the shape memoery martensitic behavior. (B) at the temperature above Af and lower than Md, NiTi shows superelastic behavior and it is possible to have stress-induced martensite. (C) At the temperature above Md, NiTi shows plastic deformation responses without stress-induced martensite formation (from figure 1 of [6], © 2017 American Association of Endodontists, reprinted with permission of American Association of Endodontists, DOI: 10.1016/j.joen.2017.01.040).

1.2 Corrosion of NiTi SMAs

The applications and reliability of NiTi SMAs depends on performance of these material in different environments. Degradation of oxide layer can lead to different forms of corrosion and accelerate failure of NiTi SMAs. Most of the investigations for the NiTi SMAs degradation in corrosive environments belongs to biomedical applications where the biocombability of NiTi SMAs plays an important role. Potential Ni release is the major parameter to compromise safe utility of NiTi alloys in the human body. The electrochemical interaction of the NiTi SMAs with surrounding fluid results Ni release. However, this interaction can lead to formation of an oxide layer, on the surface can protect the subsequent NiTi SMAs from further corrosion or can reduce the corrosion rate of these alloys.

1.2.1 Factors Affecting Corrosion Behavior of SMA

Schiff et al. compared the corrosion behavior of NiTi alloy with titanium alloys. They reported less noble corrosion potential for NiTi compared to pure titanium and titanium alloys. However, their results show NiTi to be less affected by the fluoridated medium in compare to other titanium alloys[7]. Li et al. studied the effect of chloride and fluoride ions on the corrosion behavior of nearly equiatomic nickel-titanium wires. They found the susceptibility of NiTi alloy to localized corrosion in presence of chloride ions and to general corrosion in presence of fluoride ions[8]. Pentlon et al. investigated the effects of temperature on the corrosion behavior of the NiTi. Their study showed a significant effect of increasing the temperature in increasing the passive current density and the reduction of the breakdown potential. Unfortunately, they did not publish the change in

microstructure and the data related to phase transformation temperature so the correlation between the phase changes and corrosion behavior cannot be concluded[9].

Toker, et. al. studied the significant role of dislocation networks on localized oxidation and corrosion behavior of NiTi SMA via static immersion experiments in simulated body fluid solution. They found preferential formation of local oxide particles around dislocation networks which are high-energy zones (Figure 1.4)[10].

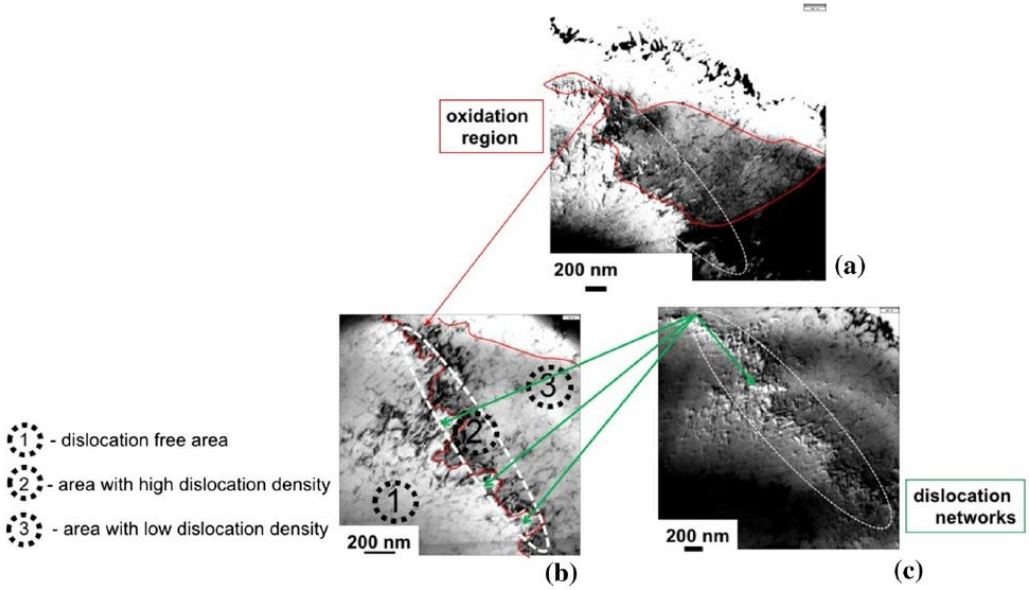

Figure 1.4 SEM images of the areas with different dislocation densities showing an oxidation region on the NiTi wire surface after statically immersed in simulated body fluid for 30 days. (a) Full area of oxidation, (b) higher magnification image of the oxidation region, area 1 is the dislocation free region, area 2 is the region with high dislocation density and area 3 is the low dislocation density region. The white dotted line shows the area with mainly localized oxidation which is the dislocation networks. (c) the high dislocation density area from b shows the formed oxide are preferentially localized around the dislocation network. with the same contrast conditions applied on both sides of the dislocation networks (from figure of [10], reprinted by permission from Springer Nature: [Journal Publisher (Springer)] [Journal of Materials Science] [Toker SM, Gerstein G, Maier HJ, Canadinc D. Effects of microstructural mechanisms on the localized oxidation behavior of NiTi shape memory alloys in simulated body fluid, © Springer (2018), advance online publication, DOI:10.1007/s10853-017-1586-4).

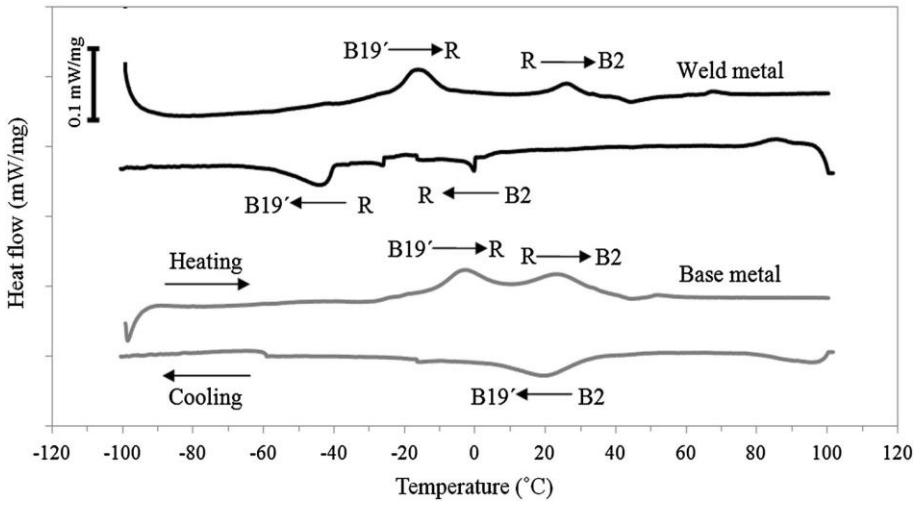

Figure 1.5 DSC curves of the as-received and Nd:YAG laser welded NiTi SMA wire (from figure 4 of [11], reprinted by permission from Springer Nature: [Journal Publisher (Springer)] [Journal of Materials Engineering and Performance] [Mirshekari GR, Kermanpur A, Saatchi A, Sadrnezhaad SK, Soleymani AP. Microstructure, cyclic deformation and corrosion behavior of laser welded NiTi shape memory wires, © 2015, Springer Nature, advance online publication, DOI: 10.1007/s11665-015-1614-y).

Microstructural changes of NiTi SMAs have investigated and the contradictory results obtained from different studies. Mirshekari, et al. demonstrated the corrosion behavior changes of NiTi SMA (Ti-55 wt.% Ni wire) after the Nd:YAG laser welding process. They revealed the better corrosion resistance of the weld metal in comparison with as-received metal. They studied the change in the phase transformation with DSC which shows the base metal is in austenitic phase at room temperature and weld metal is

in martensitic phase. However, their study didn't consider the effect of different existing phases on the corrosion behavior[11].

Es-souni, et al. compared the transformation behavior and mechanical properties of two NiTi SMA wires of close chemical compositions (Ni57.6Ti42.4 %wt and Ni57.8Ti42.2 %wt). They reported the effects of surface topography and surface finish residues on the potentiodynamic corrosion behavior and biocompatibility of the material. They study included the potentiodynamic polarization at two different temperature. Their study correlated the corrosion resistance of NiTi SMA to the surface finish and the amount of surface finish residue. However, they have studied the potential impact of different crystallographic phase on surface finishing process where the sample are polished by electrochemical techniques. In their study the sample with Austenite phase shows lower corrosion resistance compare to the sample with mixture of austenite and martensite[12]. Table 1 shows the characteristic phase transformation temperatures and results of the pitting corrosion potential at two different temperatures.

The localized corrosion events can be associated to the presence of particles in NiTi SMAs. Neelakantan, et al.s investigated the passivity behavior of NiTi SMA with different level of secondary phase particle. They performed potentiodynamic polarization on NiTi SMA with different distribution of titanium carbide as a second phase in an electrolyte of 0.9% sodium chloride at 37˚C. The alloy with lower secondary phase showed a higher breakdown potential and alloy with higher density of larger secondary phase were more susceptible to pitting corrosion. The passive layer on the NiTi SMA with

higher secondary phase density showed lower resistance and poor stability in comparison to NiTi SMA with lower secondary phase density[13].

Table 1 Transition temperatures determined from the DSC curves for two commercial NiTi SMA wires and pitting corrosion potential measured with potentiodynamic polarization at two different temperatures in a Ringer solution (from table 1 of [12], reprinted by permission of © 2002 Elsevier, DOI: 10.1016/S0142-9612(01)00416-1).

	Phase Transformation Temperatures (˚C)				Pitting corrosion potential (V)	
Composition	M_s	M_f	A_s	A_f	at 22˚C	at 37˚C
Ni57.6Ti42.4 %wt (Neosent)	-23	-59	22	33	1.4	1.2
Ni57.8Ti42.2 %wt (SeNiTi)	-72	-80	8	18.5	0.43	0.5

Crone et al. investigated the corrosion behavior of NiTi SMA with variation in phases. They compared the corrosion behavior of specimens with different austenite finish temperature and found the sample with lower austenite finish temperature has the better pitting corrosion resistance than the one with higher austenite finish temperature[14].

1.2.2 Corrosion Mechanism on NiTi SMAs

Tao, et al. studies the corrosion behavior of NiTi SMAs in a 0.9% NaCl physiological solution and proposed a mechanism for the pits forming during pitting corrosion[15]. The Figure 1.6 shows a schematic of proposed mechanism on NiTi SMAs attacked by chloride ions. Figure 1.6 (a and b) shows the early pitting corrosion on many

sites on the surface of NiTi SMAs due to the vulnerability of original oxide layer to attack by chloride ions. The early step of corrosion process occurred on surface defects initially and following the attack by chloride ions which leads to the breakdown of Ni-Ti bond and breakdown of original oxide layer. Figure 1.6-b illustrates the pitting sites propagation and observable pores formation on the surface of NiTi SMAs, as time elapsed.

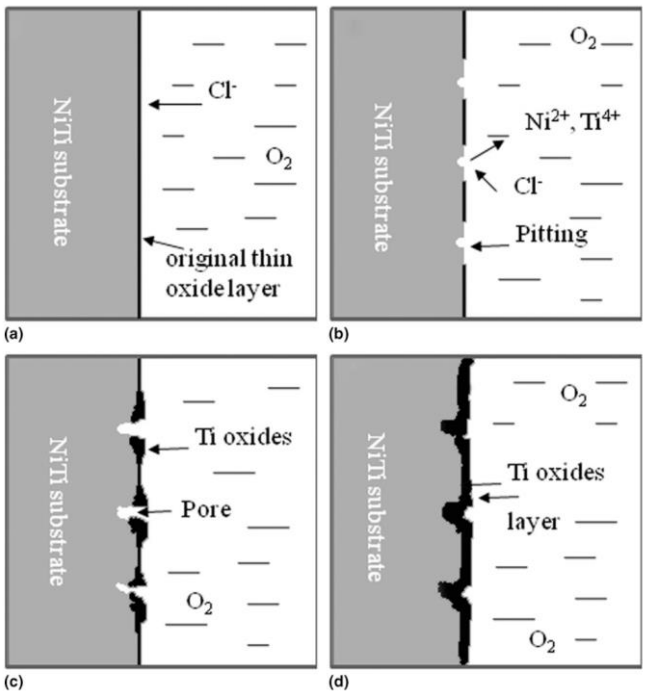

Figure 1.6 Schematic of corrosion product layer formation on NiTi SMAs in the NaCl solution (from figure 8 of [15], © Materials Research Society 2010, reprinted by permission of Cambridge University Press, DOI: 10.1557/JMR.2010.0051).

Figure 1.6 C shows the process to form titanium oxide around the pitting sites and pores. In this step, Ni-Ti bond breakdown causes nickel ions release from the bulk materials into the solution. The latter reduces the local concentration of nickel in the materials. The dissolved oxygen ions in the solution react with the remaining titanium and form titanium oxides around the early stage pitting site and formed pores. As the corrosion process proceeds, the corrosion product layer grows and expands over the entire surface of NiTi SMAs. XPS results (Figure 1.7) reveals that this corrosion product layer is composed of different titanium oxides (TiO, TiO_2, and Ti_2O_3) with relatively depleted Ni. As time elapsed, the growth rate of pores decreases due to possibly being blocked by the corrosion product formed inside the pores. The latter results the formation of a uniform and dense oxide layer on the NiTi SMAs. This uniform and dense titanium oxide layer serves as a passivation film and will retard the corrosion process. Figure 1.6-d demonstrates the titanium oxide film on the NiTi SMAs surface as a barrier against outward diffusion of metal ions from the bulk metal.

Figure 1.7 shows the high-resolution XPS spectra. This measurement can reveal the composition of corrosion product by measuring the Ti and Ni binding energy as a function of the sputtering time. Curve 1 represents the outmost surface of NiTi SMAs and indicates the composition of outer most surface is essentially of Ti^{4+}, Ti^{3+} and Ti^{2+} which are corresponding to TiO_2, Ti_2O_3 and TiO, respectively. After 30 minutes of sputtering, the spectra belongs to the deeper NiTi substrate and the main chemical state of Ti^0 as the intermetallic NiTi state[15].

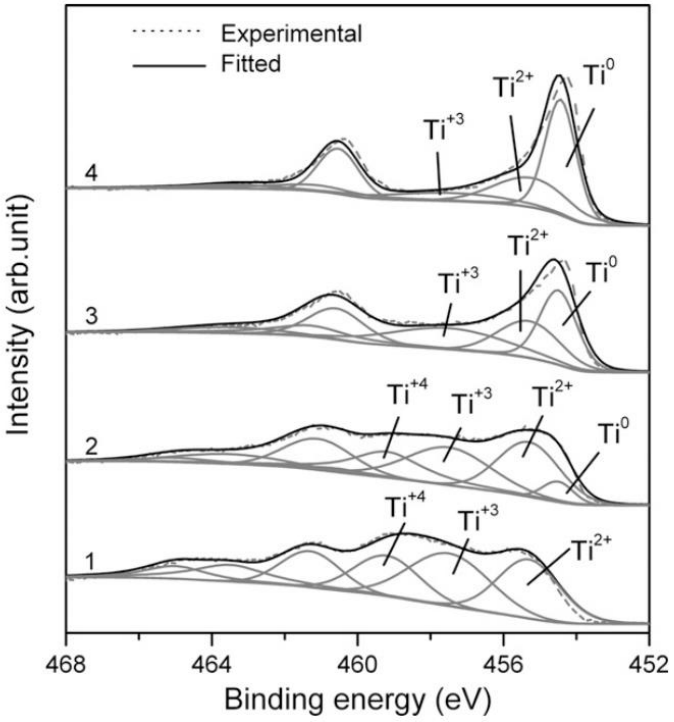

Figure 1.7 High-resolution Ti 2p XPS spectra acquired from the surface of NiTi specimens immersed in the 0.9% NaCl solution at different sputtering times: (1) 0 min, (2) 5 min, (3) 10 min, and (4) 30 min (from figure 5 of [15], © Materials Research Society 2010, reprinted by permission of Cambridge University Press, DOI:10.1557/JMR.2010.0051).

1.2.3 Interaction of Mechanical Load and Corrosion

Shen et al. [16, 17] examined the fatigue behavior of two types of NiTi wires and the impact of a corrosive environment on the fatigue lifetime. All the NiTi wires subjected to rotational bending in NaOCl solution and evaluated based on the number of revolutions before fracture. Their study was qualitative in nature when they showed multiple crack

origins during fatigue cycles, but there were no details about a correlation between the formed cracks with a corrosion mechanism.

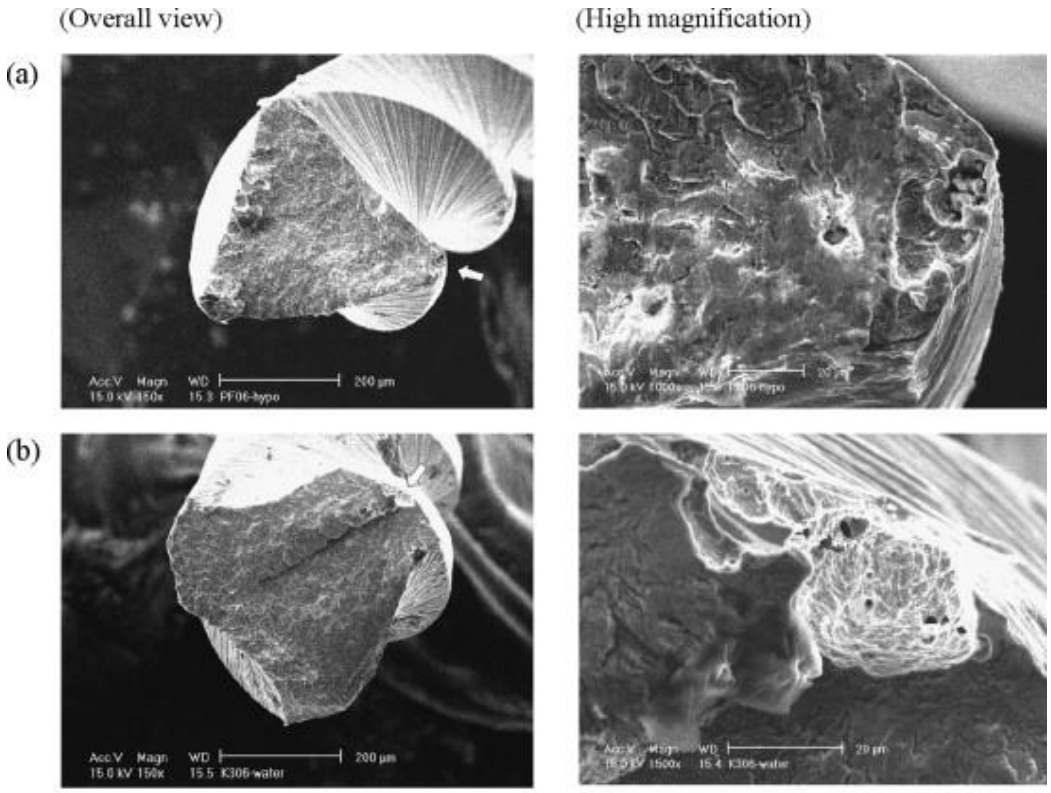

Figure 1.8 NiTi SMAs wire subjected to rotational-bending fatigue test in hypochlorite. High magnification images show the corrosion attack present in the fracture plane and corrosion pits formation are crack origins(from figure 3 of [18], © 2007 Academy of Dental Materials. Published by Elsevier Ltd., reprinted by permission of Elsevier, DOI:10.1016/j.dental.2007.09.004).

Cheung et al. [18, 19] expressed the fatigue life of NiTi in a chlorine-containing solution as a function of strain amplitude at the surface. They revealed that the sensitivity of fatigue lifetime of NiTi SMAs in corrosive environment to temperature. They found the release of latent heat causes the local temperature elevation and leading to a shortened fatigue lifetime. They reported the formation of corrosion pits as a result of localized attack by sodium hypochlorite (Figure 1.8Figure 1.1).

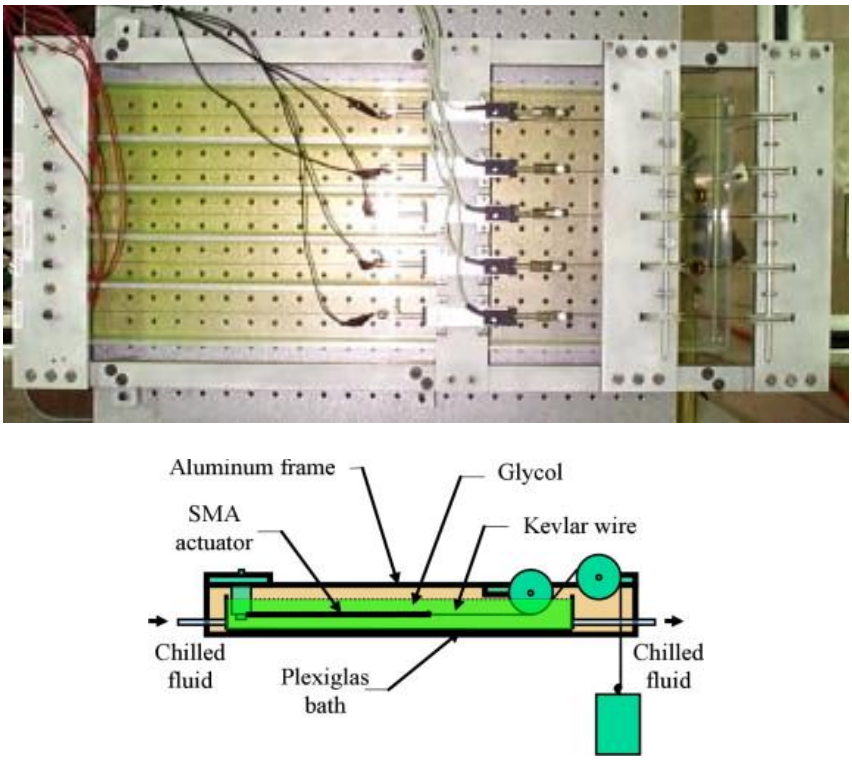

Figure 1.9 Illustration of experimental setup to study the fatigue corrosion of SMA actuators undergoing thermally induced martensitic phase transformation in corrosive environment (from figure 1 and 2 of [20], ©2009 Elsevier, reprinted by permission of Elsevier, DOI:10.1016/j.ijfatigue.2009.04.012).

Lagoudas et al. [20, 21] investigated the influence of corrosion on the fatigue life of SMA actuators undergoing thermally induced martensitic phase transformation (Figure 1.9). They reported a significant reduction of fatigue life in the presence of a corrosive environment. They reported a spallation oxidation occurring at the surface of the actuator, and suggested that formation of a brittle oxide layer on the surface in corrosive environment causes a reduction in lifespan.

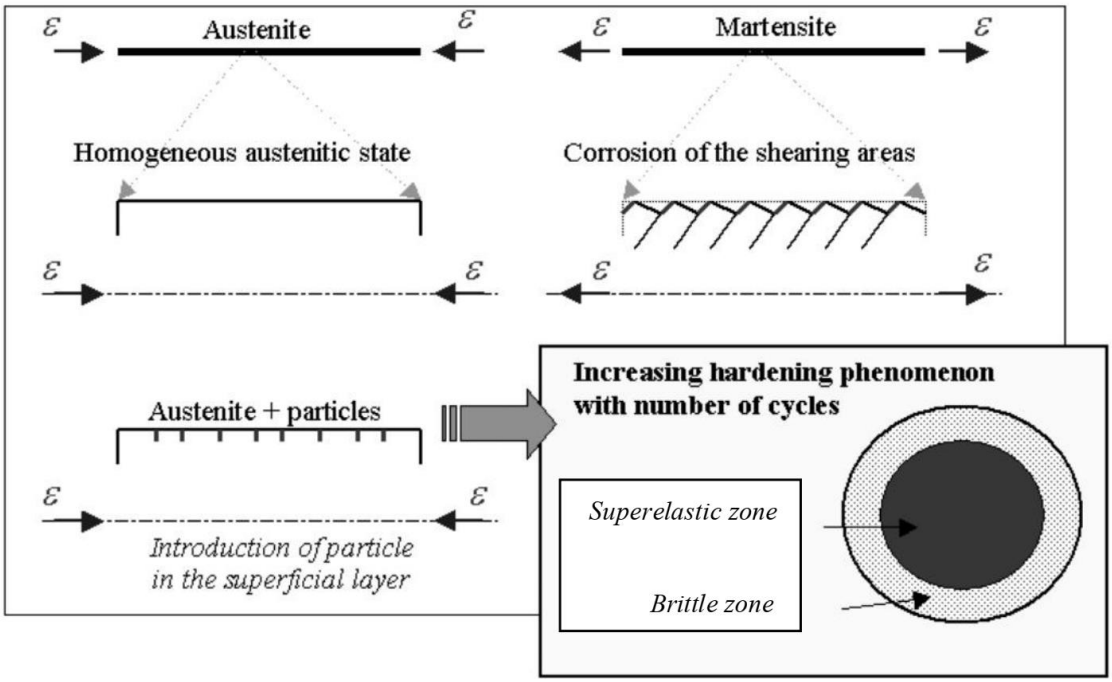

Figure 1.10 Schematic of proposed mechanism for the brittle oxide layer formed on the surface of NiTi SMA wires in corrosive environment (from figure 23 of [22] , ©2003 Society of Photo-Optical Instrumentation Engineers (SPIE), reprinted by permission of SPIE, DOI:10.1117/12.508207).

They proposed a hardening mechanism to explain change in lifespan of NiTi SMA (Figure 1.10). The material is cycled from the austenite phase to martensite phase. The microstructure changes start from surface where a homogeneous austenite transformed to a detwinned martensite. The preferential corrosion spots on the surface formed. This mechanism proposes the expansion of oxide layer based on transferring oxidized particles from outer layer to inner layer during reverse martensite transformation. The cycling process causes further accumulation of oxidized particles in a large outer zone of the NiTi SMA wires. A significant reduction of the fatigue life of actuators in corrosive environment and scattering of the fatigue data observed for the both complete and partial transformation cycles. Their study suggested a relationship between number of cycles and corrosion.

Racek et al. [23, 24] investigated the mechanism of corrosion of NiTi during cyclic mechanical loading. They developed a new setup for an in situ electrochemical study of superelastic NiTi wires/springs in body fluids during cyclic mechanical loading. However, by having a U-bend or spring NiTi as part of the setup that led to a synergic action, the correlation of load vs. electrochemical process was not covered. It is important to notice that most of existing studies on the corrosion of SMAs pertain to mechanical failure analysis and general corrosion in the presence of cyclic loading, rather than the influence of surface/electrolyte mechanisms on the corrosion assessment. There is a strong need to investigate the role of transformation/reorientation on the corrosion behavior of SMAs due to its influential effect of the surface during electrochemical processes, such as active and

passive states, where the latter leads to an integral characterization of corrosion assessment.

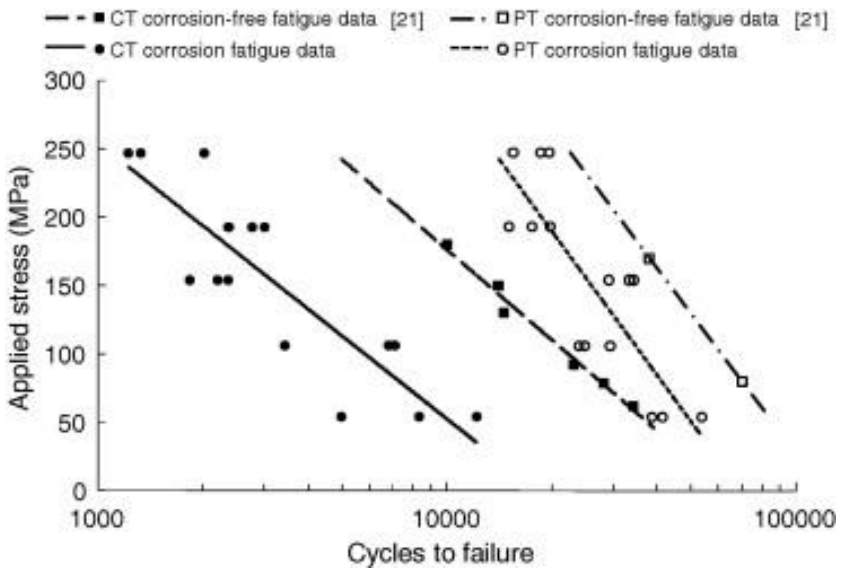

Figure 1.11 Influence of corrosive environment on the stress-life responses of SMA wires actuators for partial and complete transformation cycles (from figure 1 and 2 of [20], ©2009 Elsevier, reprinted by permission of Elsevier, DOI:10.1016/j.ijfatigue.2009.04.012).

2. LOADING INFLUENCE ON THE CORROSION ASSESSMENT DURING STRESS-INDUCED MARTENSITE REORIENTATION IN NICKEL-TITANIUM SMA[1]

2.1 Introduction

Shape memory alloys (SMAs) are a class of active materials with the capability to undergo and recover large deformations upon subjection to certain external stimuli, i.e., temperature and mechanical load. This capability has roots in a martensitic transformation, a solid-to-solid, diffusionless phase transformation between austenite and martensite. Upon loading, SMAs initially in the austenitic phase undergo phase transformation and recover the resulting strain upon unloading (pseudoelasticity). If initially in a martensitic phase, they undergo detwinning/reorientation upon loading. The apparent permanent strain after unloading can be recovered, and SMA can return to the original shape by subsequent heating (shape memory effect) [2]. Due to these unique mechanisms, SMAs, such as nickel-titanium (NiTi), have found applications in the biomedical, automotive and aerospace industries [25, 26].

Despite an endless potential use for this alloy, the application of SMAs has been limited by a lack of knowledge about their failure behavior, which has become a key factor to fulfill safety and reliability requirements. Studying the failure mechanisms of SMAs is rather challenging because of the effects of phase transformation/reorientation and the

[1] Portions of this section are reprinted or adapted from Mohajeri, M., Case, R., Haghgouyan, B., Lagoudas, D. C., & Castaneda-lopez, Loading influence on the corrosion assessment during stress-induced martensite reorientation in nickel-titanium SMA. Smart Materials and Structures, Copyright © 2020 The Author(s). Published by IOP Publishing Ltd. DOI: 10.1088/1361-665X/ab681d

inherent thermomechanical coupling. Despite this, there has been a recent rising interest in investigating the effects of the aforementioned phenomena on the failure of SMAs [27, 28]. The role of corrosive environments in the failure behavior of SMAs has been investigated [16, 18, 19, 29]. Several studies have considered the impact of corrosive environment on performance of NiTi SMAs by measuring the change in fatigue lifetimes and studying the fracture surface. Shen et al. [16, 17] studied the impact of a corrosive environment on the fatigue lifetime for NiTi wires subjected to rotational bending and recorded the number of revolutions before fracture. Their study was qualitative in nature when they showed multiple crack origins during fatigue cycles, but there were no details about a correlation between the formed cracks with a corrosion mechanism. Cheung et al. [18, 19] expressed the fatigue life of NiTi in a chlorine-containing solution as a function of strain amplitude at the surface. They reported the formation of corrosion pits as a result of localized attack by sodium hypochlorite. Likewise, Lagoudas et al. [20, 21] investigated the influence of corrosion on the failure of SMAs and reported a significant reduction of fatigue life in the presence of a corrosive environment. Their study suggested that this reduction in lifespan was due to a brittle surface oxide layer formed in such an environment. Racek et al. [23, 24] investigated the mechanism of corrosion of NiTi during cyclic mechanical loading. They developed a new setup for an in situ electrochemical study of superelastic NiTi wires/springs in body fluids during cyclic mechanical loading. However, by having a U-bend or spring NiTi as part of the setup that led to a synergic action, the correlation of load vs. electrochemical process was not covered. It is important to notice that most of existing studies on the corrosion of SMAs pertain to mechanical

failure analysis and general corrosion in the presence of cyclic loading, rather than the influence of surface/electrolyte mechanisms on the corrosion assessment. There is a strong need to investigate the role of transformation/reorientation on the corrosion behavior of SMAs due to its influential effect of the surface during electrochemical processes, such as active and passive states, where the latter leads to an integral characterization of corrosion assessment.

In this chapter, I investigate the effects of mechanical loading and martensite reorientation during a corrosion assessment for NiTi SMAs. Following an electrochemical cell set up designed to characterize the interfacial response while mechanical loading is imposed, experimental techniques coupled with imaging and high-resolution surface analysis helped to quantify parameters describing the passive-active state properties. The relationship of constant load vs. interfacial characterization gave important insight for understanding SMA performance in a corrosive environment. To the best of the authors' knowledge, this is the first time that multiple nondestructive in situ measurements have been reported to characterize the impact of an NiTi SMA crystallographic reorientation during a corrosion assessment. This includes an investigation on the changes in the passive oxide layer during stress-induced martensite reorientation by using digital image correlation (DIC) along with OCP and EIS techniques.

2.2 Experimental

2.2.1 Material characterization

The NiTi specimens utilized in this study were provided by ATI Inc., we cut 4 mm^2 samples from an as-received commercial equiatomic NiTi in a sheet form. A Perkin-Elmer Pyris 1 differential scanning calorimeter (DSC) was utilized for measuring the phase transformation temperatures [30].

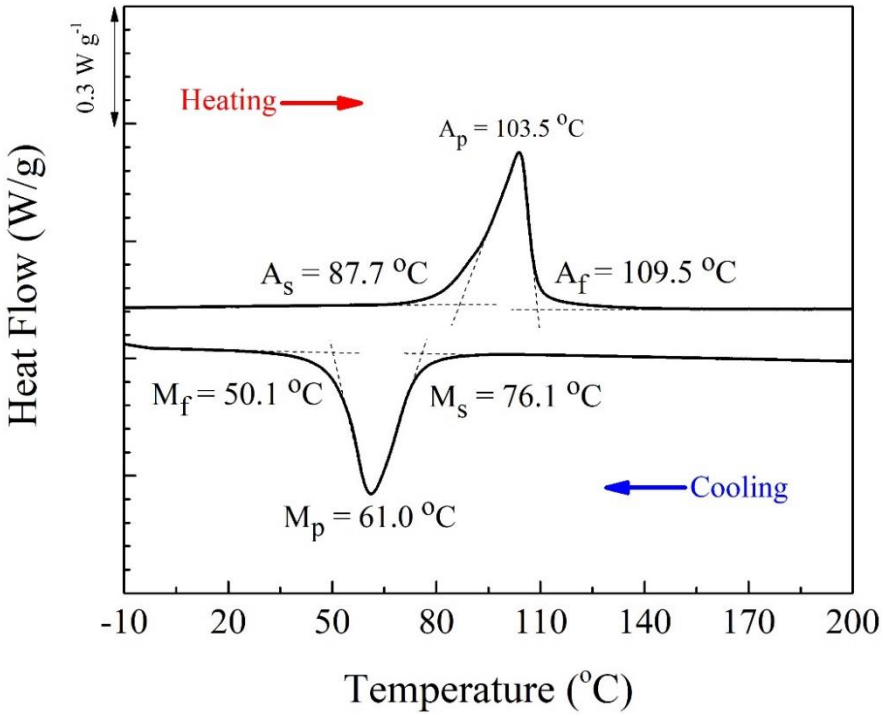

Figure 2.1 DSC curve and transformation temperatures for NiTi.

Figure 2.1 shows the DSC curve for the heating and cooling of the sample. The exothermic and endothermic DSC peaks on cooling and heating are characteristics of the

forward and reverse martensitic transformation of NiTi, respectively. The tangent method was used to obtain martensite start (M_s) and martensite finish (M_f) temperatures during cooling and austenite start (A_s) and austenite finish (A_f) temperatures during heating [2]. The transformation temperatures on Figure 2.1 indicate that the material state at room temperature was fully martensite.

For mechanical characterization, a flat ASTM E8/E8 M sample [31] with a gauge length of 60 mm and a width of 9 mm were cut by using electrical discharge machining (EDM). The uniaxial tensile test was carried out at room temperature in a servo-hydraulic MTS test frame equipped with a 100 kN max load cell. Tension was applied to the sample with a loading rate of 0.2 mm/min until failure.

2.2.2 Experimental design

In this study, the corrosion behavior of martensitic NiTi SMA was studied under an isothermal loading condition due to a microstructure reorientation. The mechanical properties of the NiTi SMA were evaluated by using a uniaxial tensile test in air. The detwinned/reoriented martensite region was determined with tensile test results (Figure 2.2).

Figure 2.2 plots the engineering stress-strain curve for NiTi at room temperature. Since room temperature was below M_f, the material was in a twinned martensitic state at zero load. Upon loading, the twinned martensite was elastically deformed up to ~1% strain. A deviation from linearity was observed at close to 200 MPa, indicating the start of the detwinning/reorientation process. Given that a stress plateau can involve both twinning

and detwinning, as well as some slip/plastic deformation [32, 33], the term "reorientation" is used for the rest of this article. A stress plateau was observed at ~240 MPa during which the deformation was dominated by a reorientation of martensite variants. At the end of reorientation (approximately 4% strain), reoriented martensite predominantly deformed elastically. This was followed by the start of plastic deformation at approximately 600 MPa, after which the deformation was dominated by slip plasticity with final failure of the material at close to 900 MPa [30, 34-36].

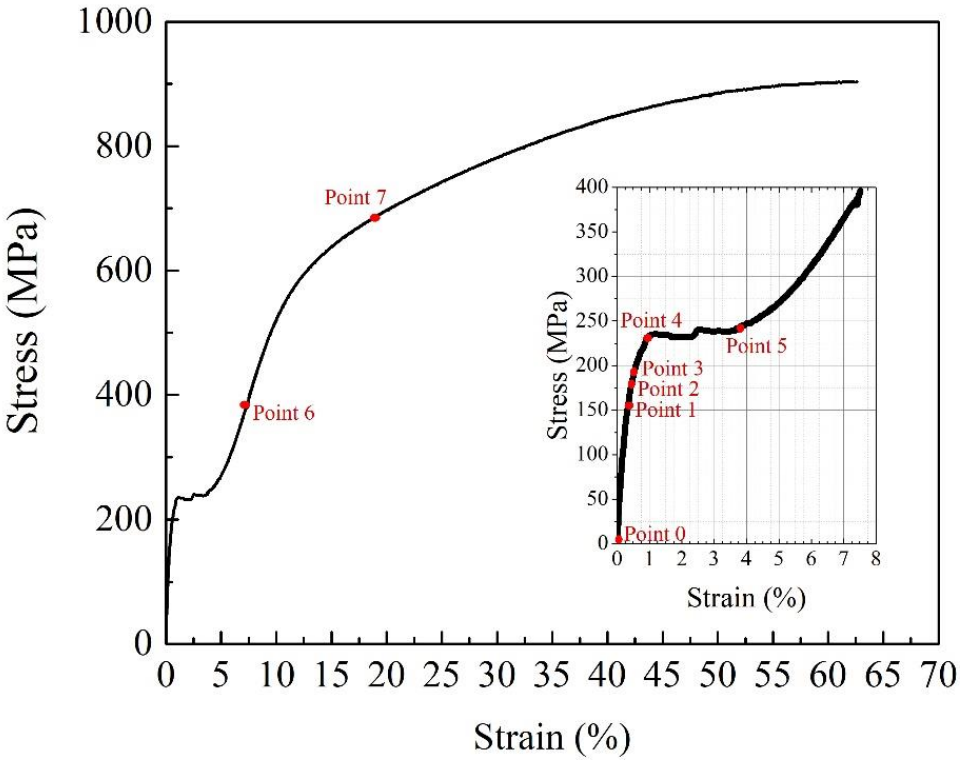

Figure 2.2 Stress-strain curve of the NiTi sample with an initial martensite phase.

Due to the presence of nonlinear deformation mechanisms, the specimen underwent a large elongation (more than 60%). The corrosion measurements were conducted at different load levels ranging from an elastic region of twinned martensite to a detwinned martensite (~ 240 MPa), and then up to a plastic flow of a mechanically detwinned martensite. A schematic of the load steps is shown in Figure 2.3. Different load steps were chosen to study corrosion behavior of the elastic deformation of twinned martensite (from point 0 to point 3), inelastic martensite reorientation (from point 4 to point 5), elastic deformation of detwinned martensite (point 6) and plastic deformation of detwinned martensite (point 7). The values of stress and strain at each step are presented in Table 2.

Table 2 Stress and strain value of the NiTi dog bone at different load steps.

Load step	0	1	2	3	4	5	6	7
Stress (MPa)	0	160	178	190	232	244	386	683
Strain (%)	0	0.36	0.45	0.52	0.9	3.8	7.4	18.8
Material state	Tw	Tw	Tw	Tw	Tw & DTw	Tw & DTw	DTw	DTw

Tw: Twinned Martensite DTw: Detwinned Martensite

The corrosion response of the SMA material was evaluated using electrochemical methods. The electrode kinetics at different load levels was studied by using the following sequence of techniques.

Open Circuit Potential (OCP): The value of OCP can be used to characterize the active or passive nature of the surface at the electrolyte/substrate interface over time. The surface can undergo an active state (metal dissolution), a passive state, or a mix of both states over time[37].

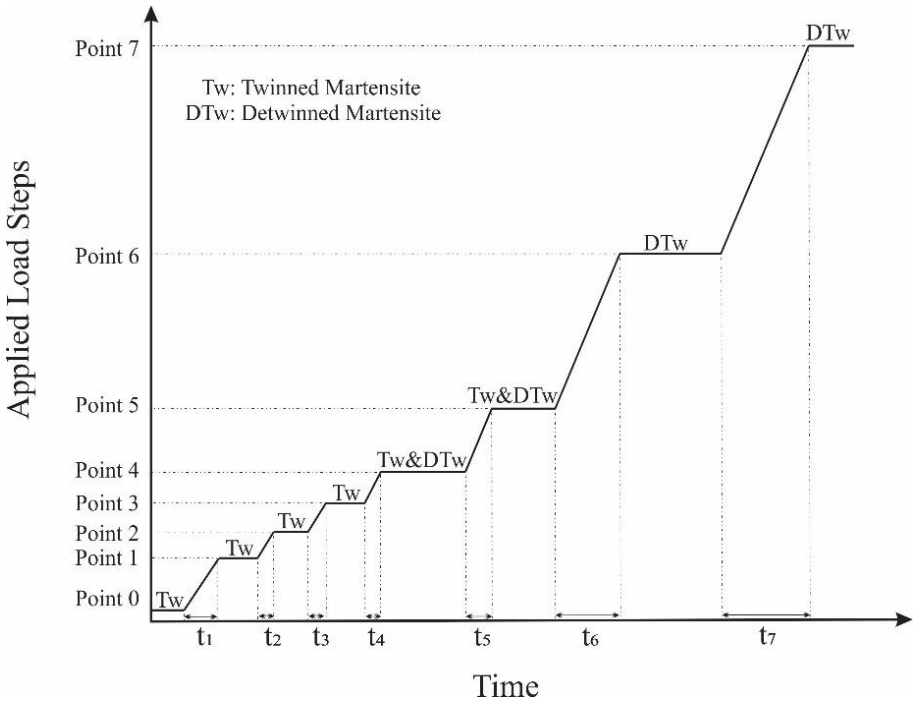

Figure 2.3 Schematic diagram of the electrochemical loading.

Linear Polarization Resistance (LPR): The polarization resistance is a technique that characterizes the surface activation conditions on the interface by assuming that the charge transfer resistance is inversely proportional to the corrosion rate, which can be used to determine the surface active state of the NiTi sample under constant mechanical loads.

Electrochemical Impedance Spectroscopy (EIS): EIS is a technique based on a transfer function principle including the introduction and measurement of a small current/potential amplitude in an electrochemical system. The spectra evolution with different loading reflects the interfacial mechanisms and characterizes the corrosion of the alloy surface. The oxide film formation and breakdown characteristics (charge transfer and mass transfer mechanisms) can be studied by utilizing a small amplitude alternating current (AC) source. EIS technique follows the linear system theory in which electrical passive elements can be used to characterize each element of the electrochemical system formed by associating each element with either charge transfer, mass transfer or simply the properties of the materials [38].

Electrochemical Frequency Modulation (EFM): The spectra evolution with different loading reflects the corrosion progression of the electrode surface. EFM is a nondestructive method that applies a simultaneous dual-frequency potential wave to a metallic sample. The quality of results and validity of the EFM measurements can be verified by the experimental values of causality factors [39, 40].

A surface characterization was implemented by using a JCM-6000Plus Versatile Benchtop scanning electron microscope (SEM). The surface was examined before exposure to corrosion and following electrochemical testing.

2.2.3 Experimental methodology

Imaging method

Digital image correlation (DIC) was used to measure the 2D strain field on the gauge section. To this end, white spray paint was first applied to the specimen surface. Black speckles were then sprayed on to produce a random pattern. Images were recorded with a rate of 1 Hz and using a Point Gray camera fitted with a Tokina ATX Pro lens, resulting in an optical resolution of 0.037 mm/pixel. The DIC subset size was selected as a 21x21 pixel based on the strain error (<0.1%) from the rigid body translation experiment; the step size was five pixels. The recorded images were postprocessed using Vic-2D-6 software provided by Correlated Solutions. Further details on DIC can be found in another reference [41].

Electrochemical testing methods

To investigate the interaction between mechanical and surface effects due to chemical dissolution effects, a uniaxial pseudostatic tensile test was performed for an ASTM E8/E8 M sample in a modified Ringer's solution with a composition of 9.0 g l^{-1} NaCl, 0.42 g l^{-1} KCl, 0.24 g l^{-1} $CaCl_2$ and 0.2 g l^{-1} NaHCO [42]. The Ringer's solution was used to simulate the body fluids.

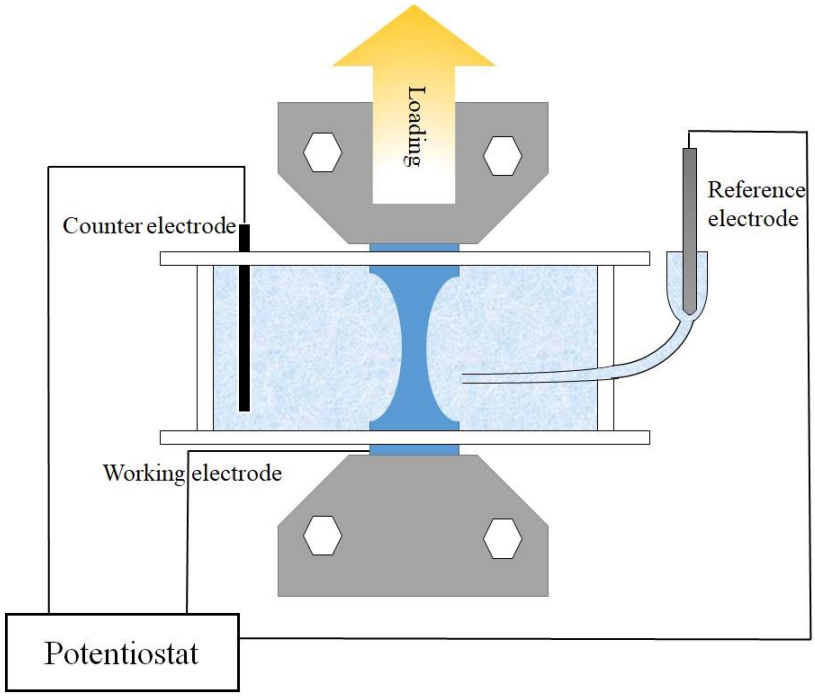

Figure 2.4 Schematic of the experimental setup for the electrochemical measurements.

Figure 2.4 shows the schematic of the mechanical-electrochemical setup.

Figure 2.5 and

Figure 2.6 shows the electrochemical cell used includes a conventional three electrode configuration with a graphite rod as the counter electrode and a saturated calomel electrode with a Lugging capillary as the reference electrode [43, 44].

A metallic ASTM tensile sample was the working electrode (Figure 2.6). The sequence of experiments included the immersion of the specimen in the electrolyte for 30 minutes prior to mechanical testing in order to reach a dynamic steady state condition.

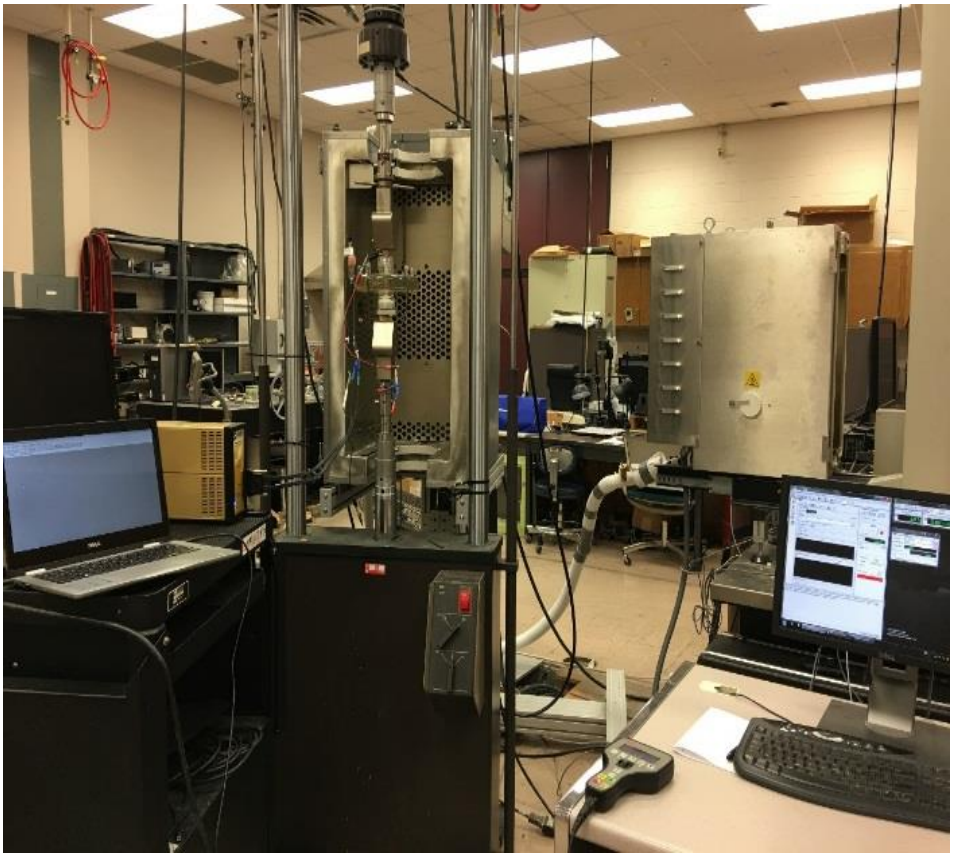

Figure 2.5 The mechanical-electrochemical setup.

The OCP was measured with respect to time during loading conditions. Measurements were performed with a Gamry Instrument Potentiostat/Galvanostat (600+). The OCP was continuously measured at each load level until stable potential values were achieved. The other electrochemical techniques (EFM, LPR and EIS) were carried out upon reaching a stable potential at time t_0 (immediately after the achievement of a stable potential value) and at each load level.

Figure 2.6 The mechanical-electrochemical setup includes a conventional three electrode configuration with a graphite rod as the counter electrode, a saturated calomel electrode with a Lugging capillary as the reference electrode ,and a metallic ASTM tensile sample was the working electrode.

EIS measurements were carried out at the open circuit potential with an amplitude of 10 mV in a frequency range of 10 kHz to 30 mHz. EFM was carried out using two frequencies, 2 and 5 Hz, and a perturbation signal with an amplitude of 10 mV [40]. LPR was performed as the last electrochemical method at each load step in order to avoid the

negative effects of potential perturbation and polarization on the EFM and EIS methods. The selected potential range was ±20 mV from stable potential values achieved during the incubation period. The scan rate employed for the LPR test was 0.125 mVs^{-1}.

2.3 Results and discussion

Figure 2.7 represents the open circuit potential of the SMA specimen measured continuously during a pseudostatic applied loading in a Ringer's solution and at different stress and strain levels.

In the elastic deformation stage of twinned martensite (from point 0 to point 3), the open circuit potential remains constant (-189 ± 2.5 mV vs SCE). There are quick drops in the OCP of the metal alloy that coincide with the martensite reorientation region (point 4 and 5), the elastic deformation state of detwinned martensite (point 6) and the plastic deformation of detwinned martensite (point 7). The steep drop indicates a transition to an active dissolution state on the surface of the metal alloy. Upon increasing the applied load, the OCP drops quickly and then gradually reaches a relatively steady-state value at the end of each increment. The potential magnitude indicates the activation and repassivation stages when the alloy faces loading conditions.

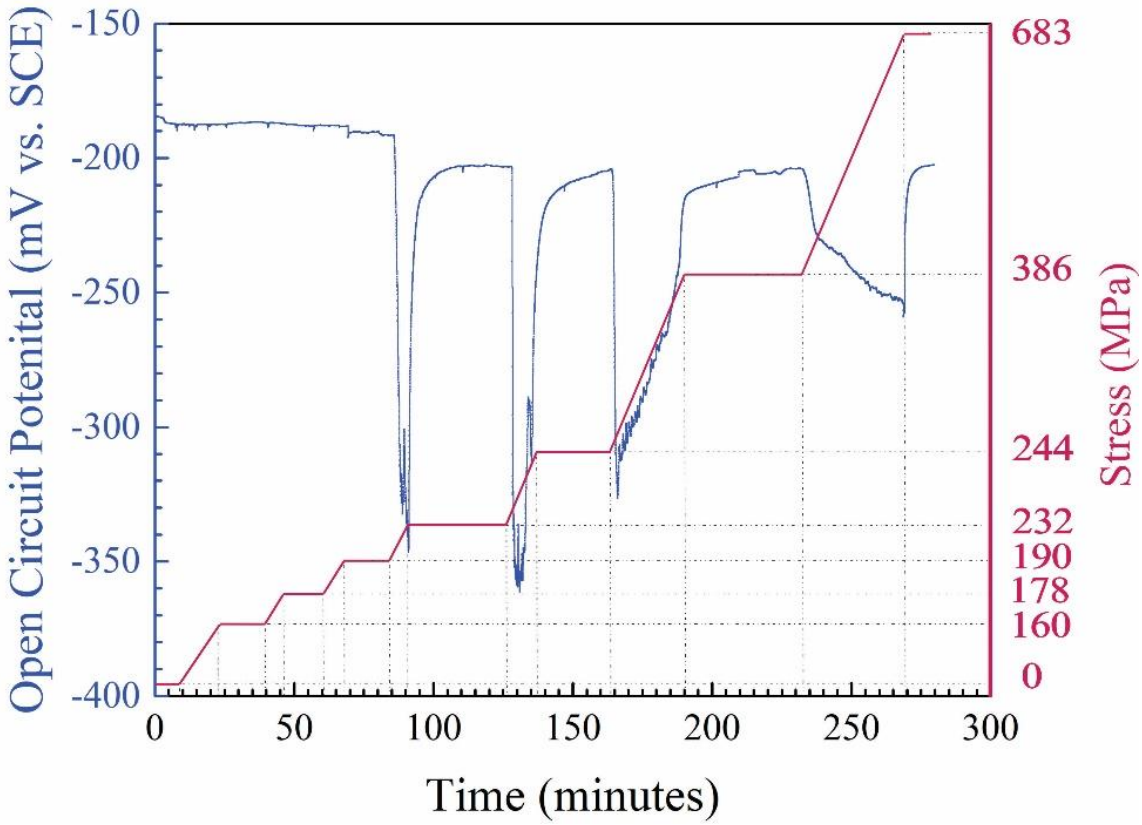

Figure 2.7 OCP of NiTi-SMA in a Ringer's solution during pseudostatic loadings.

Figure 2.8 and Figure 2.9 show the SEM images from the surface of the sample before and after the experiment, respectively. Figure 2.9 shows an active site formed on the surface due to the applied stress and the corrosive environment. Extensive cracking is found on the surface after applying stress. This shows that a passivity breakdown has taken place by applying a load and reaching roughly a 20% strain level. Spots of dark pores formed on the surface can be observed on the surface of NiTi-SMA following the electrochemical/mechanical testing. The latter is in accordance with previous works on the formed passive layer in the elastic stress state, and the passivity breakdown and

localized attack susceptibility in chloride solutions [45-47]. A passive film formed in the presence of elastic stress has a higher donor and acceptor concentration than that of a passive film formed in a stress-free state. The higher concentration of acceptor and donor sites promote the local attack susceptibility and breakdown of the passive film in an elastic stress state [48].

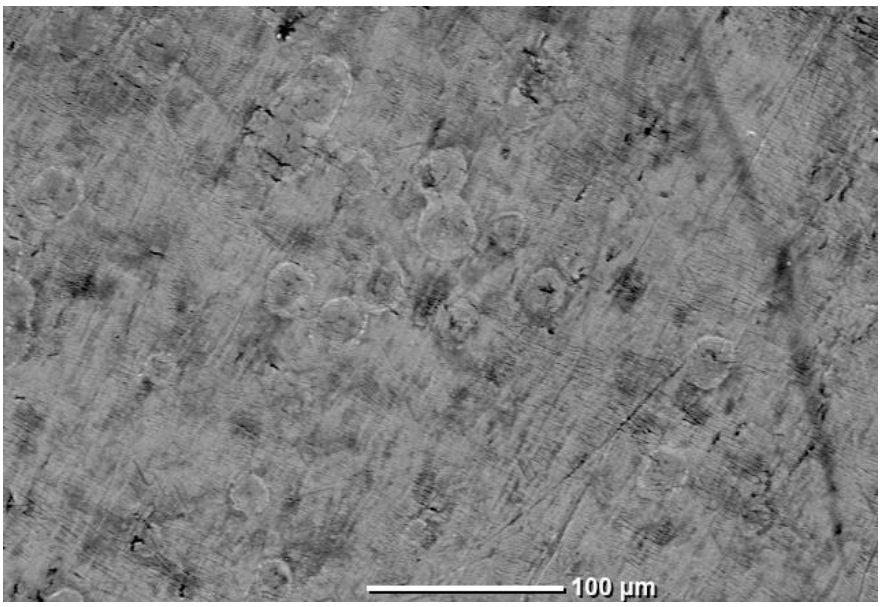

Figure 2.8 SEM images from the surface of the as received NiTi-SMA.

The EIS measurement results in Ringer's solution at different stress levels are shown in Figure 2.10 and Figure 2.11.

Table 3 shows the EDS results of the as received material and the material after corrosion testing. The EDS analyses reveal an increase in the ratio of Ti/Ni from 3.92 for as-received NiTi to 4.34 for NiTi after corrosion testing. This trend has been reported in previous studies [49, 50]. The passive film breakdown and subsequent repassivation influence the titanium content in the passive film. The chemical ratio increases for the titanium content takes into consideration some sites where the activation and repassivation are occurring, while the rest of the surface coverage maintains the layer at steady state conditions.

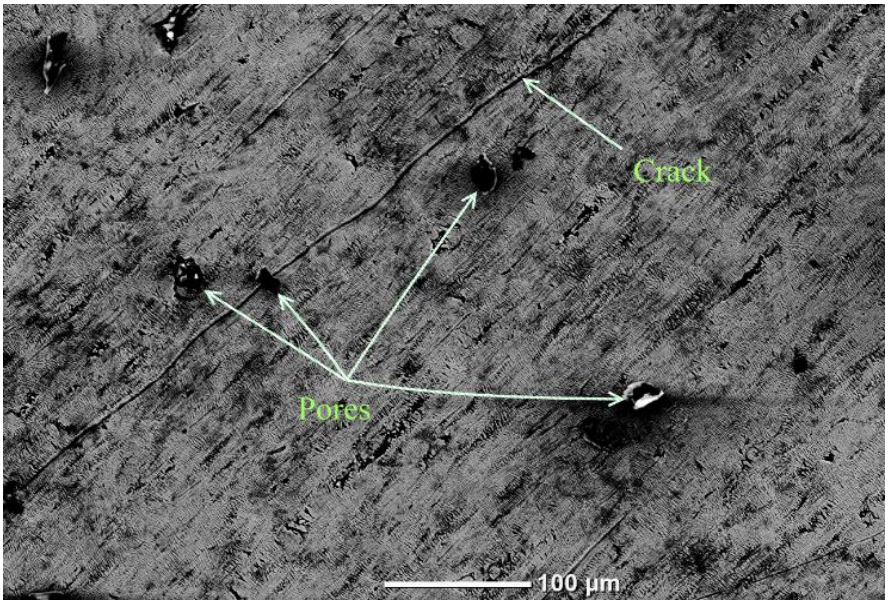

Figure 2.9 SEM images from the surface of the NiTi SMA after corrosion testing in Ringer's solution during pseudostatic loading at room temperature.

The EIS measurement results in Ringer's solution at different stress levels are shown in Figure 2.10 and Figure 2.11.

Table 3 Surface analysis of NiTi-SMA, before and after corrosion testing in Ringer's solution.

	Nickel (at%)	Titanium (at%)	Oxygen (at%)	Titanium/Nickel
As-received	14.49	56.80	28.71	3.92
After corrosion testing	13.90	60.32	25.78	4.34

In the EIS signature plot (Figure 2.10), the logarithm of the impedance and phase shift are plotted with respect to the logarithm of frequency. The EIS plots at medium and low frequencies represent the response associated with mechanisms occurring in the passive layer and interfacial reactions at the substrate/solution interface, respectively. Figure 2.10 gives the phase angle signature from the NiTi sample at different loading conditions while under continuous strain and exposed to Ringer's solution. For different stress levels, the phase angle magnitudes of the impedance response at medium frequencies are close to 80 degrees. The above magnitude resembles a pseudocapacitance behavior that can be attributed to a dense passive oxide film, such as titanium in steady state conditions [51-53].

The phase angle magnitude decreases slightly during different stress levels between point 0 to point 6 followed by a slight increase. The latter could be due to a passivation and repassivation process. The phase magnitude at medium frequencies

illustrates the stability of the passive layer formed, while the total impedance at low frequencies in Figure 2.10 illustrates the charge transfer process at the interface. The formed passive layer on the surface of the NiTi sample is composed mainly of titanium oxide (TiO_2) with a small mixture of nickel [53]. The composition of the passive layer formed during oxidation of the titanium alloy is directly related to the alloying elements and temperature. The presence of NiO and $NiTiO_3$ in addition to the TiO_2 has been reported as the temperature increased to above 700°C [54, 55].

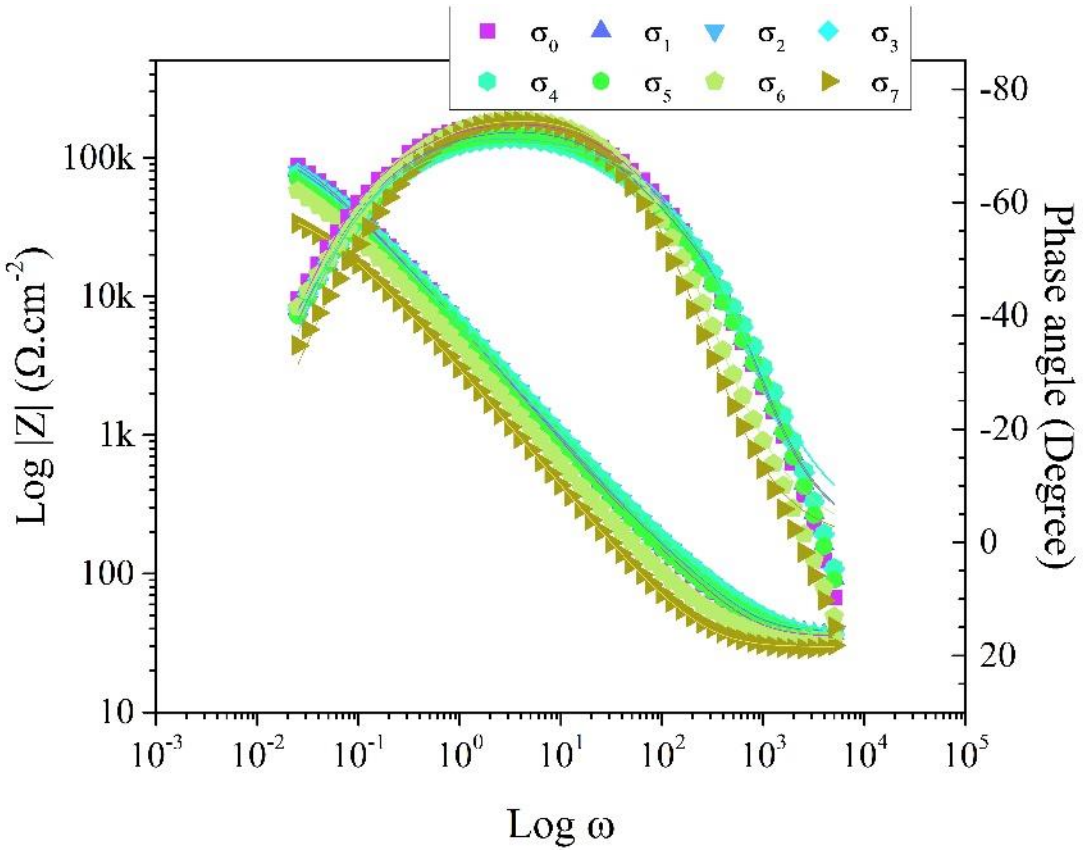

Figure 2.10 Bode plots of the NiTi SMA specimen under different stress levels in Ringer's solution at room temperature.

Figure 2.11 shows the Nyquist plot representations for the NiTi SMA at different loads as previously described. In the Nyquist plots, the negative imaginary part of impedance is plotted versus the real impedance. The Nyquist plot is used to create an electrically passive analog circuit that characterizes an electrochemical system. The predominant mechanism is a charge transfer at the interface due to the dissolution of the metallic alloy in the corrosive environment. The passivation and repassivation is based on the interfacial reactions and layer breakdown occurring when the constant load is applied. The semicircle magnitude denotes surface activation (charge transfer mechanism) as the load increases. The last stress level σ_7, ε_7 indicates the lowest impedance magnitude. The diameter of the semicircle decreases when the load (stress) is higher. The latter takes into consideration the charge transfer mechanism being influenced by the activation or creation of active sites and the passivation-repassivation process. The semicircle magnitude agrees with the phase angle trend in which the passive layer breaks down (surface activation) and produces defects allowing the electrolyte into the passive layer.

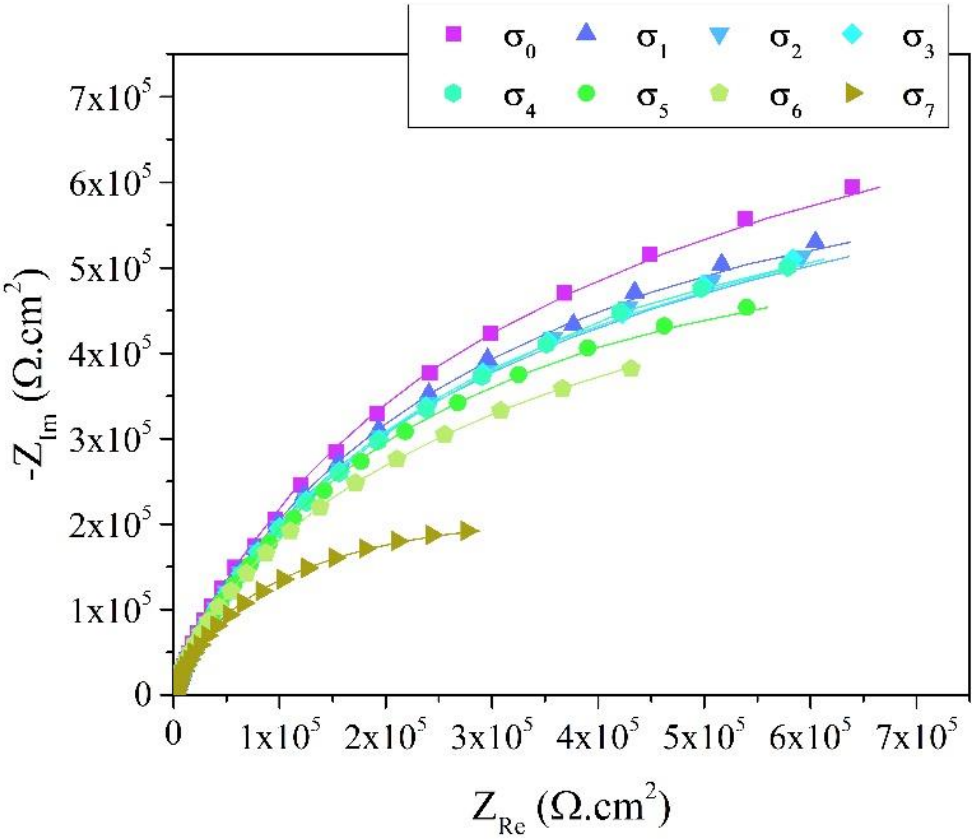

Figure 2.11 Nyquist plots of the NiTi SMA specimen under different stress levels in Ringer's solution at room temperature.

The electrochemical system can be characterized by an equivalent circuit analog to qualitatively and quantitatively assess the effects of the stress level and the martensite reorientation influencing the active-passive corrosion behavior of NiTi in Ringer's solution. The electrochemical elements are represented as electrical passive elements illustrated in Figure 2.12. The proposed electric equivalent analog includes a solution resistance, $R_{electrolyte}$, in series with a parallel circuit of a constant phase element (representing a passive layer and pore resistance), R_{pore}, and finally a resistance representing the charge transfer process $R_{polarization\ resistance}$ and a constant phase element

(CPE) for the interface between the passive porous layer with the metallic substrate. The $R_{polarization\ resistance}$ can characterize the surface activity and corrosion resistance under various stress levels.

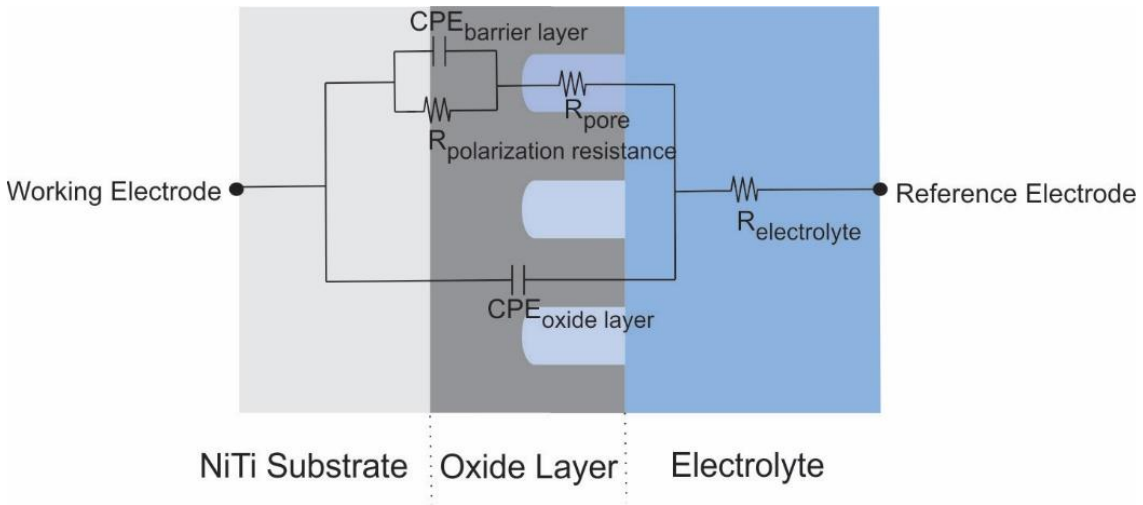

Figure 2.12- Equivalent circuits proposed for fitting the electrochemical impedance response of NiTi SMA for various stress levels in Ringer's solution at room temperature.

The CPE parameter is defined as [53, 56]:

$$Z_{CPE} = \frac{1}{Y_0 (j\omega)^{\alpha}} \qquad (1)$$

where Y_0 is a constant in $Scm^{-2}s^{\alpha}$ and α is related to the angle of rotation of a purely capacitive line on the complex plane plots.

The CPE represents a parameter that characterize an electrochemical surface by considering the physical properties of the surface. The alpha parameter correlates to the roughness of the surface and represents the forming of a dense and packed dielectric

material when it is close to one. In addition, porosity and decreased compactness influences the magnitude close to zero, turning the surface into a resistor when the porosity permits current leakage through the system.

The values of the electrochemical equivalent circuit elements obtained for each stress level are presented in Table 4. α_1 and α_2 represent the exponent values for the CPE element due to the passive or barrier layer and substrate-passive layer interface respectively.

The solution resistance remains constant and does not change after applying various loads on the metallic sample. There is a decrease in polarization resistance upon applying load, which can be related to the passivation-breakdown of the oxide layer. This layer is mainly composed of TiO_2 [56]. A decrease can be observed in the polarization resistance (Rp) values when the applied loads increased. The formed corrosion product could lose adhesion in some local sites during loading conditions and reorientation. This loss in adherence is associated with changes in the abovementioned potential due to the surface characteristics [57]. R_{ct} magnitudes from 160 kΩ to 49 kΩ denote higher current exchange at the interface due to an increase in active or dissolution sites following the passive layer breakdown and repassivation at the substrate/barrier oxide interface. The pore resistance agrees with the active-passive behavior of the passive layer where the physical properties of the layer are modified during the loading conditions. Due to an increase in nickel content within the layer following loading conditions, as illustrated in Table 4, the resistivity dropped and the porosity could be increased, with the pore resistance decreasing from 140 Ω to 100 Ω.

Table 4 The values of the electrochemical equivalent circuit elements from the results of EIS tests at various stress levels.

	Stress level (MPa)							
Components	0	160	178	190	232	244	386	683
$R_{electrolyte}$ ($\Omega.cm^{-2}$)	1.78	1.9	1.7	1.7	1.8	1.6	1.6	1.5
R_{pore} ($\Omega\ cm^{-2}$)	140.2	141.8	153.6	152.8	128.8	143.4	124.4	100.8
$R_{polarization\ resistance}$ ($k\Omega\ cm^{-2}$)	160.7	145.5	142.4	141.5	125.8	118.8	100.7	49.8
$Q_{barrier\ layer}$ ($S\times s^{n}\times 10^{-4}$)	5.52	5.85	5.58	5.66	6.57	6.55	7.5	10.4
α_1	0.77	0.76	0.75	0.75	0.76	0.75	0.75	0.74
$Q_{oxide\ layer}$ ($S\times s^{m}\times 10^{-4}$)	1.54	1.36	1.76	1.71	1.47	2.7	2.73	4.36
α_2	1	1	0.95	0.954	1	0.97	1	1

Figure 2.13 shows the capacitance magnitude for the oxide layer measured by using CPE element parameters and the thickness based on expression 3.

The capacitance of the oxide layer associated with the CPE element is given by [58]:

$$c_{ox} = (Q_{oxide\_layer})^{\frac{1}{\alpha}} R_{pore}^{\frac{1-\alpha}{\alpha}} \qquad (2)$$

where Q, R and m are estimated by the CPE element expression.

The thickness of the surface oxide layer has been calculated to form the values of the capacitance oxide layer according to the following relation:

$$d = \frac{\varepsilon \varepsilon_0}{c_{ox}} \qquad (3)$$

where ε is the dielectric constant of the titanium oxide (100), ε_0 is the permittivity of free space (8.854×10^{-14} F cm^{-1}) and c_{ox} is the capacitance of the oxide layer [58, 59].

The comparison of the capacitance of the oxide layer and the thickness of the oxide layer is presented in Figure 2.13 and Figure 2.14. This trend is influenced by the loading introduced to the sample. The capacitance shows a decrease in magnitude, which is considered to be a current leakage when the capacitance is no able to store charges, rather than the current passing within the more conductive or defect interface or the substrate–passive interface. The latter might include the deterioration of the mechanical physical properties of the passive layer, or bonding with the substrate. The displayed thickness shows a decrease in magnitude. The layer not only shows a pathway for the current but also less resistance due to pore formation or breakdown as previously explained.

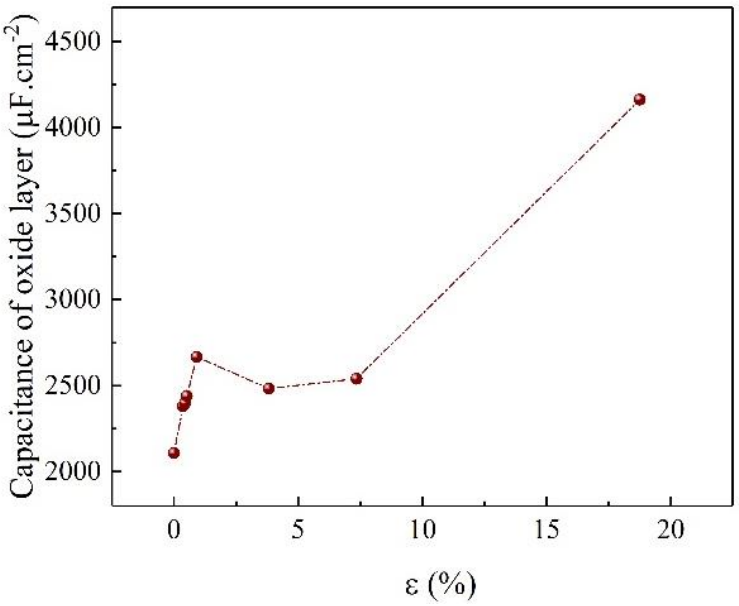

Figure 2.13 Calculated capacitance of the NiTi oxide layer under different strain level applications.

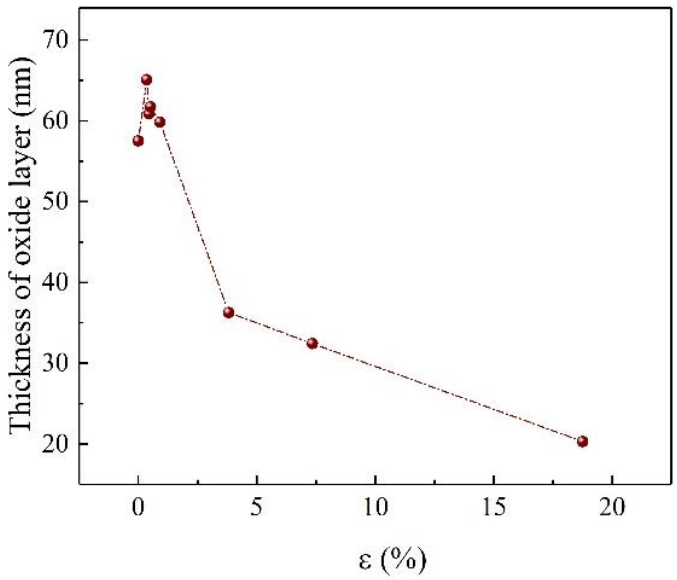

Figure 2.14 Thickness of oxide layer of NiTi under different strain level applications.

The passive layer changes can be correlated to inelastic deformation and strain distribution on the surface.

The strain distribution in the loading direction (ε_{yy}) for the ASTM E8/E8 M specimen subjected to uniaxial tension was measured using DIC and is presented in Figure 2.15-c. The contour plots correspond to overall uniaxial strain values from 1% to 4% (Figure 2.15-a) during which the martensitic NiTi undergoes martensite reorientation [60, 61]. According to the images, the strain distribution is nearly uniform throughout the specimen at the beginning. As the loading continues, strain bands oriented at approximately 45 degree, with respect to the loading direction, start to appear throughout the specimen. The localization becomes more pronounced near the bottom of the specimen at 1.7% strain. Further loading results in the broadening of the strain localization band at the bottom, and more pronounced localization of the band near the top at 2.5% strain. The bands then coalesce, and again a nearly uniform distribution is attained at 4% overall strain. The localized strain band would lead to a localized passive layer breakdown due to reorientation. The changes in the OCP are shown in Figure 2.15-b. The existence of potential drop upon loading at the beginning of reorientation is related to changes on the strain filed on the surface.

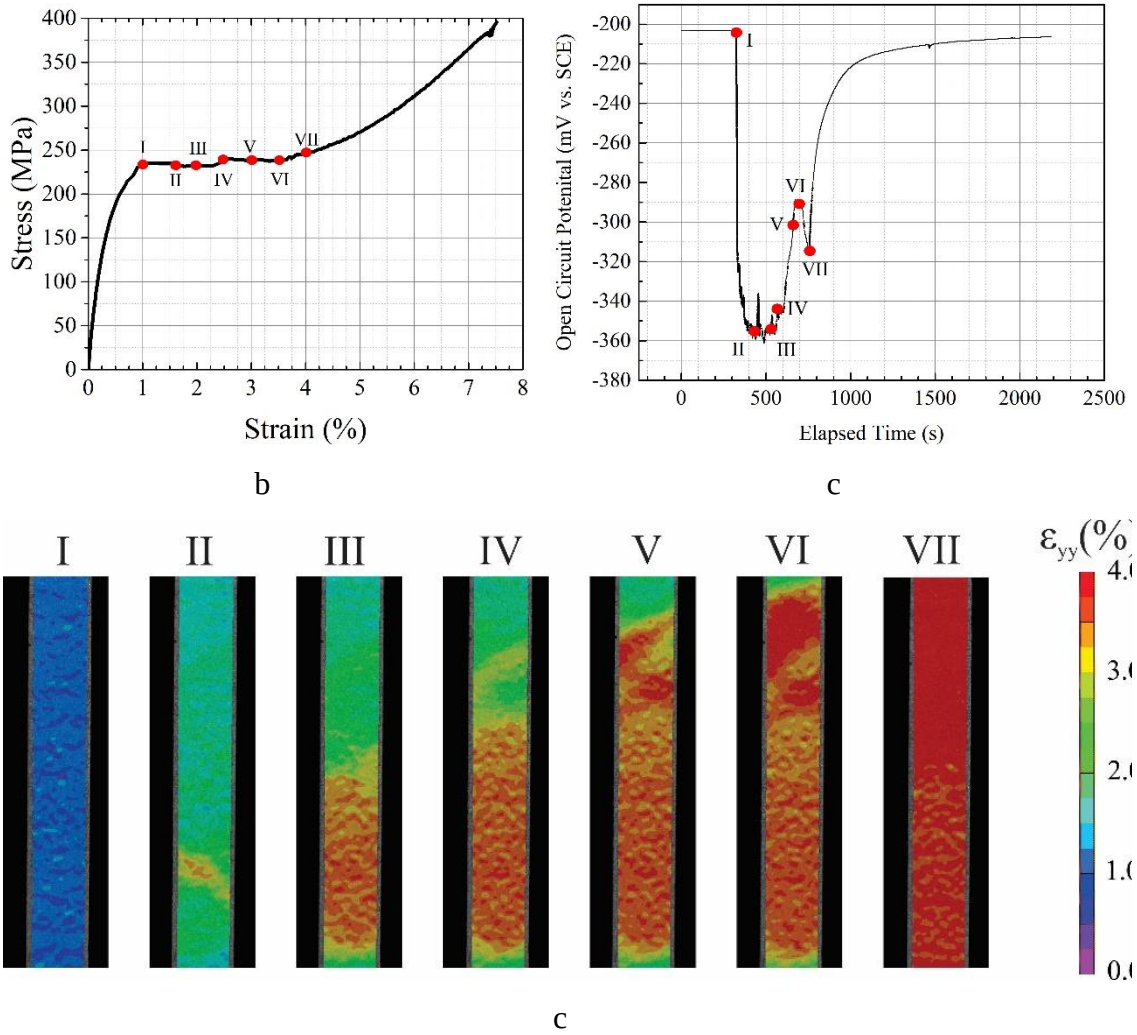

Figure 2.15 (a) stress-strain relationship for NiTi dogbone samples with (b) OCP measured during martensite reorientation (mechano-electrochemical test), and (c) the corresponding strain field from the tensile test during martensite reorientation.

Figure 2.16 shows the schematic of the passive layer changes and illustrates the passive layer breakdown and formation of a new passive layer. A stable passive layer exists on the surface of twinned martensite. The localized passive layer breakdown occurs

during the martensite reorientation due to the strain localization (b) and active dissolution sites formed on the surface. It is worth noting that while a majority of the sample experiences strains in the range 1-2%, local strains can go up to 4% due to martensite reorientation. These large strains can lead to failure of the brittle passive oxide layer on the surface. The metal dissolution rate increases inside the localized breakdown (c) and a new passive layer starts forming on the surface of the NiTi detwinned martensite.

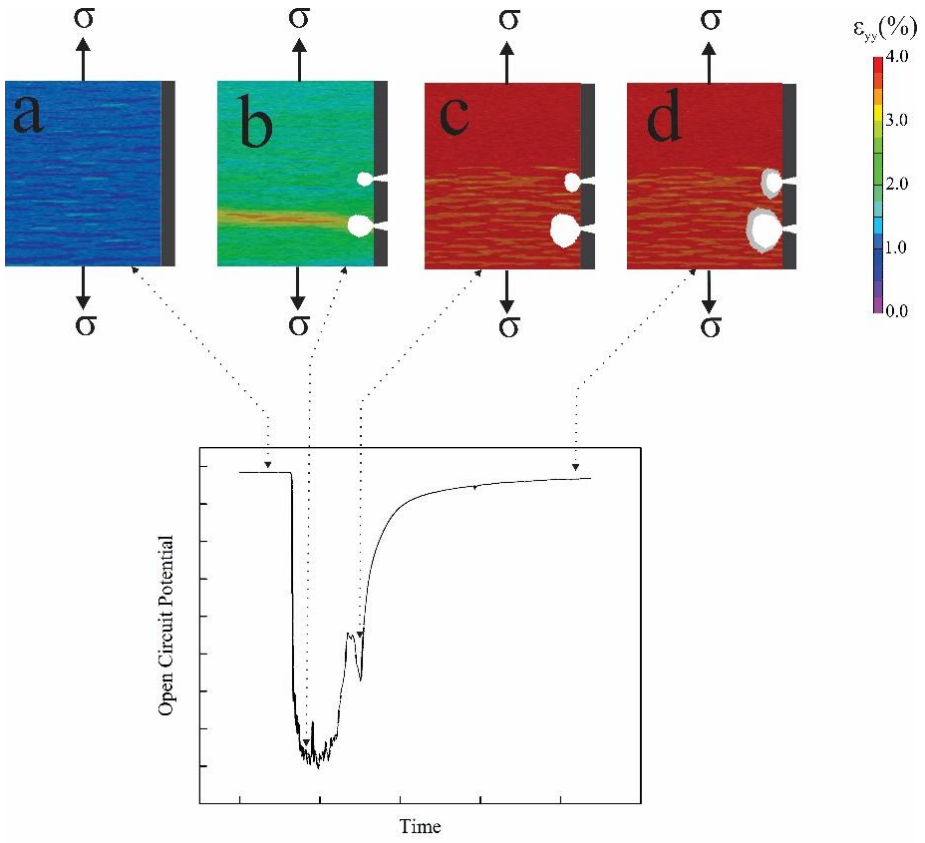

Figure 2.16 Schematic of passive layer: (a) before martensite reorientation, (b) the passive layer breakdown at the start of the martensite reorientation, (c) the martensite reorientation, (d) and the formation of the new passive layer.

To further corroborate the performance of the interface, the polarization resistance values and the corresponding E_{corr} values served as a function of the strain in a Ringer's solution, as shown in

Figure 2.17. The results indicate that there is an important change in E_{corr} values based on two different regions (elastic-plastic) and crystallographic transition (twinning-detwinning). The beginning of the deformation is the most influential parameter in the formation of the passivation layer at the surface of the substrate. Castaneda et al. [62] describes the influence of the strain rate on the mechanical breakdown of a formed passive layer. The strain rate is faster than that of the formation of the layer at the local attack sites; this latter favors and influences the passive layer breakdown. The OCP and the Rp are increasing with stress within steps 0 to 6 (Table 2), validating the influence of the elastic region for twinned martensite in the stress-strain curve.

Upon mechanical loading up to the inelastic region and after the martensite reorientation region, the E_{corr} values stay relatively constant, but the LPR and Rp slopes decrease monotonically with the applied strain. The behavior of the polarization resistance results across this range of applied strain suggests that, after martensite reorientation, the passive layer breakdown in some regions makes a porous layer where actives sites are formed, and charge transfer reactions occur during the martensite reorientation. The available sites on the porous layer are due to the passive layer breakdown and show an activation control mechanism at the interface. Both LPR and OCP magnitudes validate the correlation of loading vs. surface activation in this solution.

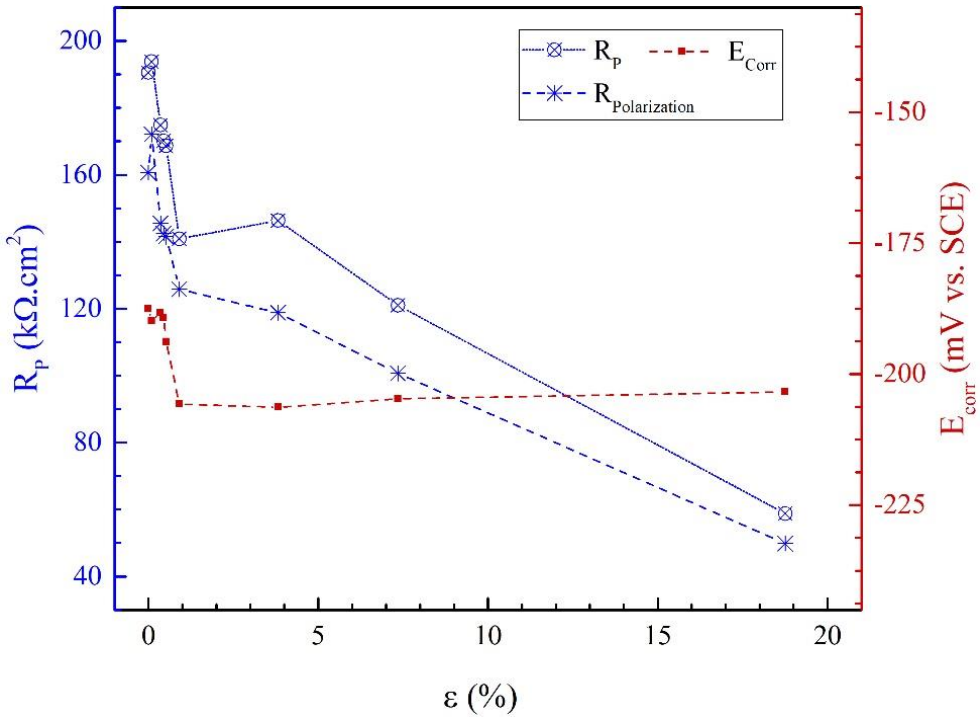

Figure 2.17 Variation of measured polarization resistance under different strain levels.

Figure 2.18 shows the calculated Tafel constants at each stress level by EFM techniques. The Tafel constants are calculated by using the current peaks obtained at the harmonic and intermodulation frequencies. The experimental values are the causality factors (CF-2 and CF-3) obtained during each EFM measurement. The mathematically established theoretical values of CF-2 and CF-3 are 2 and 3, respectively. The calculated causality factor values are approximately equal to the theoretical values and show the measured EFM data are reliable. The derived equation for mathematical calculation of the Tafel constants and causality factors are provided in Appendix I [39].

As shown in Figure 2.18, the anodic and cathodic Tafel slope values follow the same trend at the elastic region where the cathodic Tafel slopes are higher than the anodic

ones. These results suggest that the anodic reaction kinetics (metal dissolution) are consistently faster than the corresponding cathodic reaction.

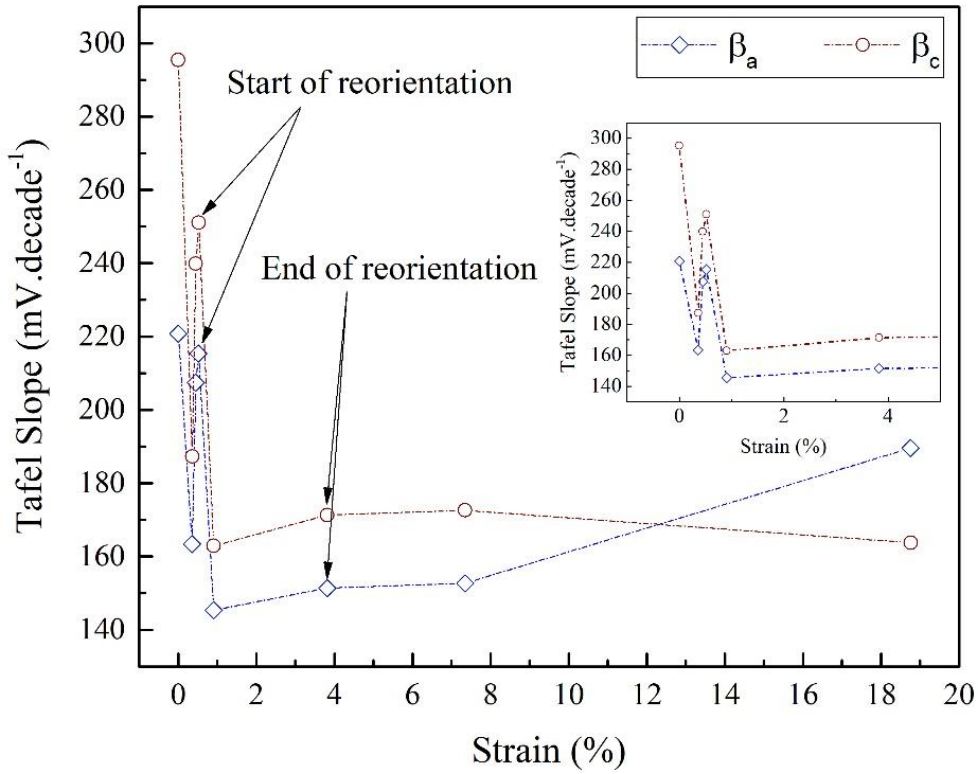

Figure 2.18 (a) Anodic and cathodic Tafel slope values obtained by electrochemical frequency modulation (EFM) for NiTi under different strain levels.

Under a uniform dissolution model, the trend followed by the cathodic Tafel slopes value are consistent with the results shown in Figure 10, indicating the increase in the corrosion rate at the passive surface in open circuit conditions. As shown in the results presented in both

Figure 2.17 and Figure 2.18, the shift to a more active condition coincides with the onset of the martensite reorientation and the loading conditions. The strain rate is faster than the repassivation kinetics; thus, the MO_x layer becomes more susceptible to breakdown when the load is increased and the strain affects the surface and the passive layer bonding. Martensitic reorientation becomes negligible for the global classical EIS or DC measurement. The localized effect due to phase transition can be characterized by local electrochemical techniques and methods, but that is beyond the scope of this work.

The relative difference between the cathodic and anodic electrode kinetics as indicated by the Tafel slopes, suggest that particularly at higher strain levels (within the plastic region), localized attack (i.e., passive layer breakdown) is possible since at open circuit conditions the higher anodic reaction kinetics would need to be sustained by a slower cathodic reaction that occurs over a larger fraction of the exposed surface.

The collective result of the electrochemical tests performed indicates that as the strain applied on the specimen increases toward the plastic range (post reorientation) the passive layer produced by the alloy is broken down in an ability to reduce the general dissolution rate at the surface. The reduction in dissolution rate is due to an increase in anodic activity and is expressed as a corrosion attack.

2.4 Summary

The effect of stress-induced martensite reorientation on the corrosion behavior of a nickel-titanium (NiTi) shape memory alloy (SMA) was characterized by mechanical-electrochemical techniques. This martensite reorientation influenced the passive state of NiTi SMA. These passive to active state transitions could be sensed by the global interfacial electrochemical measurements, such as electrochemical impedance spectroscopy (EIS), open circuit potential (OCP) and linear polarization resistance (LPR) methods. The increase in the loading when exposed to a corrosive environment resulted in the breakdown of the passive layer. A later repassivation stage was reached due to the formation rate becoming more dominant than the breakdown rate during loading conditions. The integration of the mechanical loading by tensile testing, strain distribution by digital image correlation (DIC) and electrochemical methods by OCP and EIS, characterized and detected the influence of the mechanical effect in the corrosion assessment and interfacial mechanisms.

3. CHARACTERIZING INTERFACIAL MECHANISMS OCCURRING IN SHAPE MEMORY ALLOY BY CONSIDERING THE PASSIVE REGION

3.1 Introduction

Near equiatomic nickel titanium alloys a unique combination of super elasticity, and shape memory effect properties. Their unique mechanical properties come from a reversible change between two stable microstructural phases (austenitic and martensitic). The variation in microstructural phases depends upon the temperature, pass of mechanical loading or thermal loading. Unique characteristics for this NiTi alloys set the conditions for wide range of applications such as aerospace, automobile and biomedical among others [26, 63, 64]. The mechanical properties have been the main focus of the SMA studies. The mechanical properties of NiTi under mechanical and thermal loading have been studied for the last two decades. The influence of applied loading [65, 66], applied temperature [67], environment, mechanical cycling [68] and thermal cycling [69, 70] are characterized quantitatively by constitutive models [71-75] to predict the NiTi behavior in various conditions. The change in mechanical properties due to change in microstructure has been subjected for numerous studies [69, 75, 76]. Challenge in application of SMA in corrosive environment leads to effort on study the corrosion behavior of SMA.

NiTi SMAs are recognized as corrosion-resistant materials as a result of the naturally formed passive film on their surface. This passive film mostly contains titanium oxide which is the product of oxidation of Titanium element on the surface of NiTi SMAs. The formation and breakdown of this Titanium Oxide layer on the surface of NiTi alloys were subject of many research approaches. Schiff et al. compared the corrosion behavior

of NiTi alloy with titanium alloys. They reported less noble corrosion potential for NiTi compared to pure titanium and titanium alloys. However, their results show NiTi to be less affected by the fluoridated medium in compare to other titanium alloys[7]. Li et al. studied the effect of chloride and fluoride ions on the corrosion behavior of nearly equiatomic nickel-titanium wires. They found the susceptibility of NiTi alloy to localized corrosion in presence of chloride ions and to general corrosion in presence of fluoride ions[8]. Yokoyama et al. examined the influence of pH and presence of chloride ions on the corrosion behavior and fracture of NiTi superelastic alloy by a sustained tensile-loading test in physiological saline solution containing hydrogen peroxide. They reported the longer time to fracture for the sample immersed in the solution with phosphoric acid than in the solution without acid [77, 78]. Crone et al. investigated the corrosion behavior of NiTi SMA with variation in phases. They compared the corrosion behavior of specimens with different austenite finish temperature and found the sample with lower austenite finish temperature has the better pitting corrosion resistance than the one with higher austenite finish temperature[14]. Es-Souni et al. investigated the corrosion behavior of two NiTi alloys with very close chemical composition and completely different transformation behavior and microstructure. They found a significant difference in corrosion current density due to different transformation behaviors. They showed the sample with higher austenite finish temperature has the better corrosion resistance and correlate the corrosion resistance to a smooth and homogenous martensitic/austenitic surface structure[12]. Pentlon et al. investigated the effects of temperature on the corrosion behavior of the NiTi. Their study showed a significant effect of increasing the

temperature in increasing the passive current density and the reduction of the breakdown potential. Unfortunately, they did not publish the change in microstructure and the data related to phase transformation temperature so the correlation between the phase changes and corrosion behavior cannot be concluded[9].

However, there is a lack of information to interpret the detailed aggregative effect of microstructural changes on corrosion behavior of NiTi-SMA and no specific work has clarified whether different mechanisms exist regarding the corrosion behavior of NiTi in chloride containing solution during phase transformation. Consequently, it is of importance to identify the mechanisms, in order to provide an in depth understanding of the corrosion resistivity of NiTi during thermal cycling and offer significant guidance for structural application of NiTi alloys in corrosive environment.

From the best of our knowledge the authors proposed an original microstructure characterization during thermal cycling with corrosion resistance properties. Potentiodynamic polarization technique is used to calculate corrosion potential, passive potential region and corrosion rate at each temperature. An microcapillary electrochemical system was used to investigate the localized impact of different phase distribution on corrosion behavior of NiTi alloy. The corrosion behavior of the NiTi alloy in a 3.5 wt% NaCl solution is characterized using Electrochemical Impedance Spectroscopy (EIS). The change of corrosion current density during exposure in corrosive solution is compared at different temperatures. Rule of phase transformation during thermal cycling is complement the electrochemical characterization.

3.2 Experimental

3.2.1 Material preparation and characterization

The near-equiatomic super elastic NiTi (Ni 55.8 wt%) alloy was used for this study. The test specimens were cut from a sheet of NiTi alloy 55.8 wt % Ni in composition. Specimens were polished mechanically to mirror finish and rinsed with distilled water. The phase transformation behavior was characterized by using Differential Scanning Calorimeter (DSC) in the temperature range from -40°C to 90°C at a rate of 10 °C/min. The samples weighing approximately 10 mg were gently cut and ultrasonically cleaned in acetone before testing. A base line was recorded before each test run. Three batches were tested for NiTi SMA with reproducible results in the range of accuracy of the system (1°C). The samples surface was examined using optical microscopy after mechanical polishing and etching. As-received material is characterized by the DSC chart. The calorimetric curve for the sample is shown in Figure 3.1. Two distinct peaks (30.7°C and 20.4°C) correspond to the reverse martensitic transformation on heating and the forward martensitic transformation on cooling, respectively [79]. The one peak temperature for reverse and forward transformations indicate a one-step transformation [80]. The start and the end of DSC peak on cooling corresponds to the forward transformation start temperature (M_s) at 35.7°C and finish temperature (M_f) at 6.2°C. The start temperature (As) and finish temperature (A_f) associate to the reverse transformation are 16.5°C and 41.7°C, respectively.

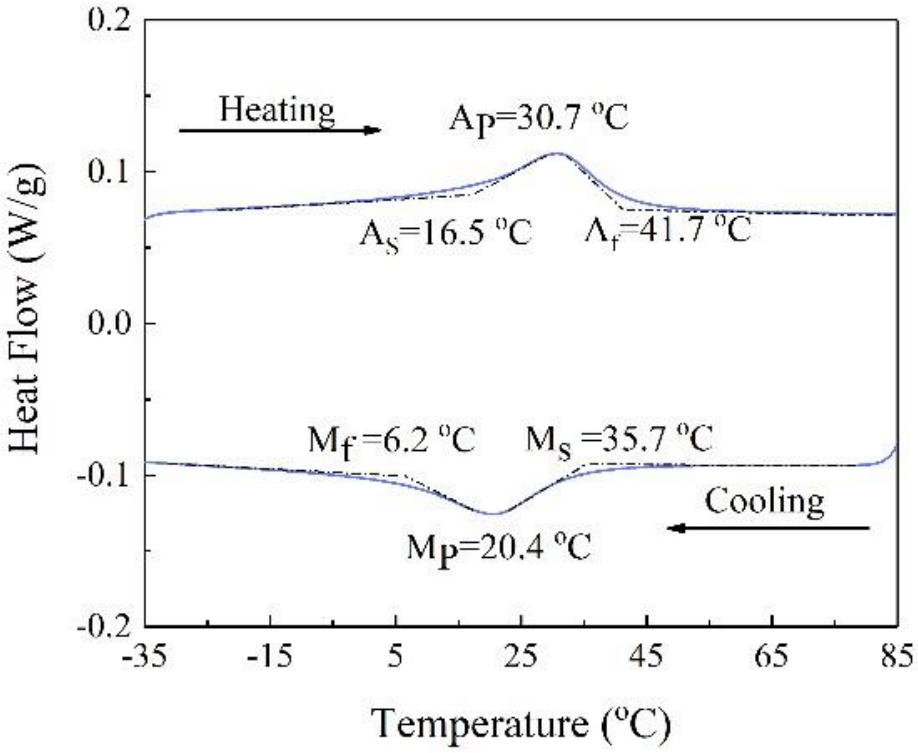

Figure 3.1 DSC charts son heating and cooling of Ni-Rich NiTi SMA with 55.8 %wt Ni.

3.2.2 Electrochemical set-up

General corrosion study: Figure 3.2 shows a schematic of electrochemical cell for thermal cycling under zero load. An Avesta three-electrode configuration (Figure 3.3) was used to study general corrosion properties. A filter water/paper ring was used in the Avesta cell to prevent crevice corrosion of specimen [28]. NiTi samples as working electrode with an area of 5 cm^2 and a rode graphite as auxiliary electrode were employed. A saturated calomel electrode served as a reference electrode. The temperature was controlled to ± 0.5°C using a closed-circuit cooler/heater (Julabo). NaCl solution (3.5 wt%) was used for electrolyte and all the solutions were N_2 deaerated.

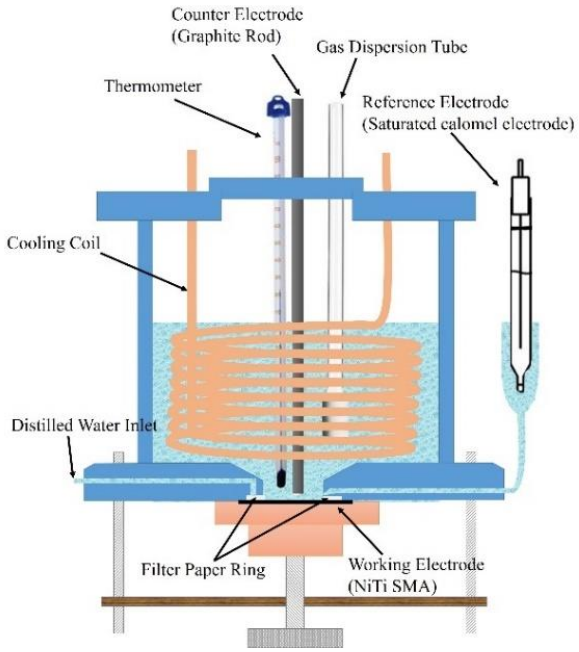

Figure 3.2 Schematic drawing of the Avesta Cell

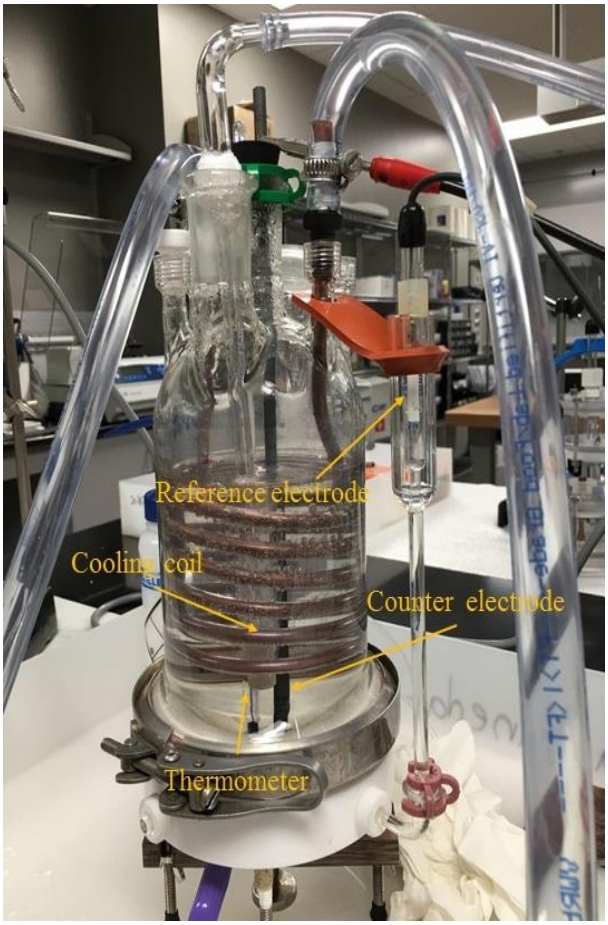

Figure 3.3 An Avesta three-electrode configuration includes NiTi samples as working electrode with an area of 5 cm^2 and a rode graphite as auxiliary electrode were employed. A saturated calomel electrode served as a reference electrode.

Microelectrochemical study: The setup for microelectrochemical investigations based on the microcapillary cell is shown in Figure 3.4. The entire setup is mounted on a microscope allowing for positioning of the capillary on the sample.

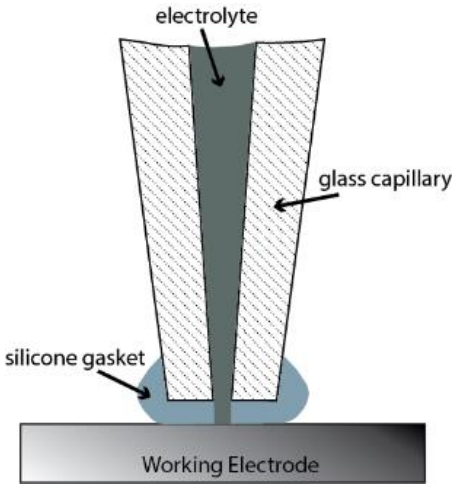

a

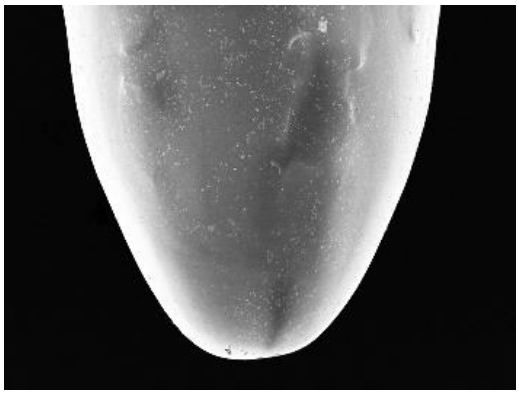

b

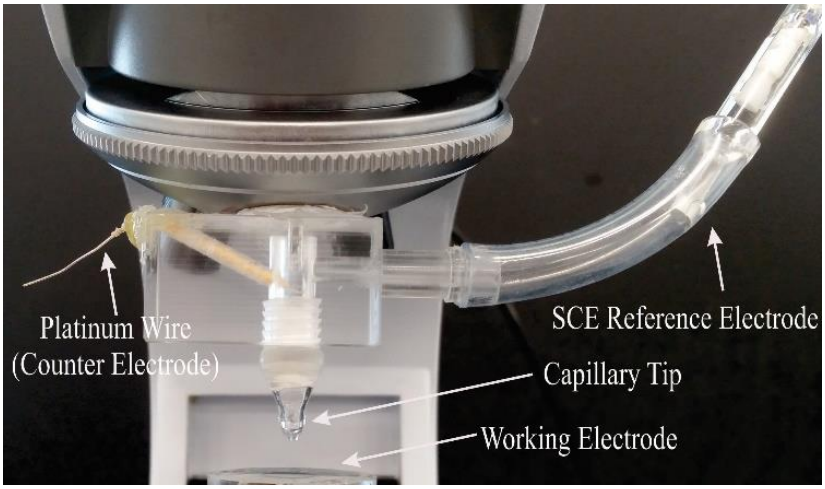

c

Figure 3.4 (a) Microcapillary set-up including the SCE reference electrode, platinum wire counter electrode, and capillary tip, (b) a schematic of the microcapillary set-up showing the silicon gasket at the end of the glass capillary tip, (c) an SEM image of silicon gasket at the end of the glass capillary tip.

A microcapillary cell mainly consists of a pulled microcapillary filled with 3.5% NaCl electrolyte. The tip diameter of our capillary was around 70 μm. A layer of silicone rubber is applied as the sealant between the front end of the microelectrode and the surface of interest. The microcell is fixed at the revolving nosepiece, replacing an objective, and the specimen is mounted on the microscope stage. This setup enabled the search of a site with different magnification before switching to the microcapillary. In this way, simple, precise, and fast positioning of the microcell is possible. The three-electrode configuration includes a saturated calomel electrode (SCE) and platinum wire are connected to the capillary as a reference electrode and a counter electrode, respectively, and NiTi sample as a working electrode. A thin microcapillary is obtained by heating borosilicate glass tube with plasma and pulling them when they reach the glass melting temperature. For sealing, the glass capillaries are dipped in a one-component silicone lacquer. A stream of air is passed through the glass microcapillary in order to flush out the silicone inside the capillary and producing a circle opening. Very thin layers of silicone are applied to the capillary tip by repeating this process three times.

3.2.3 Test Matrix

Effect of temperature and phase transformation

Samples were heated up to 90ºC to reach fully austenite state in the Avesta cell and cooled down to desired temperature (0, 10, 20, 30 and 40ºC) for electrochemical measurements. Potentiodynamic electrochemical measurements were carried out using a Solartron 1280B Potentiostat. The test procedure consisted of monitoring the Open Circuit Potential (OCP) for 60 min and then generating cathodic and anodic polarization curves. The applied potential is changed from cathodic potential ($\Delta E=E-E_{corr}$=-200 mV) to anodic potential ($\Delta E=E-E_{corr}$=1600 mV) with scanning rate (0.167 mV/sec) and direction was reversed with same sweep rate until the corrosion potential was reached. The corrosion current density (i_{corr}) was calculated by extrapolating intersect of the anodic and cathodic Tafel lines to the corrosion potential.

Current measured at corrosion potential is the corrosion current density (i_{corr}) then $i_{corr} = i_a = |i_c|$. The modified Butler-Volmer equation is described the experimental results of cyclic potentiodynamic polarization [81-83].

$$i_{net} = i_{corr}[e^{\frac{2.303(E-E_{corr})}{\beta_a}} - e^{\frac{-2.303(E-E_{corr})}{\beta_c}}] + c(\frac{\partial E}{\partial t}) \qquad \text{Eq.1}$$

Where i_{net} is net current density (external current density),i_a and i_c are the anodic and cathodic Tafel slope, respectively and c is the double layer interfacial capacitance. At low voltage scan rate (here 0.167 mV/sec), the second term of expression in right hand side of equation 1 approaches zero value. High-field corrosion potential, the logarithm of

the net current density has linear relation with the over potential ($E - E_{corr}$) in both anodic and cathodic branches. The anodic and cathodic Tafel slope can be measured as:

$$\eta_a (or) \eta_c = \left| \frac{\partial E}{\partial \log(i_{net})} \right| \qquad \text{Eq.2}$$

Effect of different phase distribution

The electrochemical tests that include EIS and potentiodynamic polarization tests were performed in the microcapillary cell. NiTi sample was experienced two step of heat treatment to achieve different distribution of austenite and martensite phases. In the step one, NiTi sample was heated up to 90ºC to reach fully austenite state and cooled down to room temperature in air. For the second step, the sample was cooled down below -10ºC to reach fully martensite state and heated up to room temperature. At each step, the EIS test was first performed and followed by potentiodynamic polarization test. The OCP measurement was always carried out prior to each electrochemical test (EIS and potentiodynamic polarization).

Thermal cycling

Sample were heated up to 90ºC to reach fully austenite state in the Avesta cell, prior to start the thermal cycling. The thermal cycling was carried by changing the solution temperature from 0ºC to 60ºC in elapsed of 10ºC. Electrochemical impedance spectroscopy (EIS) measurements were conducted over a frequency range from 5kHz down to 100mHz at 100 cycles per decade, with an amplitude of 10mV (rms) sine wave. The EIS tests were initiated 30 minutes after temperature stabilized. The equipment was a Solartron 1280B Potentiostat. The impedance data were interpreted on the basis of

equivalent electrical circuits, using the Echem Analyst Gamry program for fitting the experimental data.

3.3 Results and discussion

Figure 3.5 shows the Cyclic potentiodynamic polarization curves obtained in 3.5 wt% NaCl solution at different temperature from 0°C to 40°C for the NiTi specimens. It is possible to observe the presence of a wide passivation plateau for the NiTi samples at all temperatures. The measured current density remains constant with increasing applied potential at passivation region and indicates the growth of formed passive surface oxide at this region. A shorter range of passivation potential for the sample at for the samples at 10°C and 40°C indicates a higher tendency to localized corrosion. This may justify by high strain on the surface due to the forward martensitic phase transformation and its consequence on the breakdown the passive layer with brittle nature of oxide layer formed on the surface of NiTi samples. Moreover, the tendency to localized corrosion may be related to the presence of different ratio of martensite and austenite phases may lead to have higher cathodic sites and less anodic sites. Figure 3.5 shows that no significant difference in passivation current densities are detected for the samples at 0ºC, 20ºC, and 30 ºC. However, the higher current density at 40ºC is probably due to the change on corrosion reaction rate by temperature. All the samples have shown no evidence of crevice corrosion.

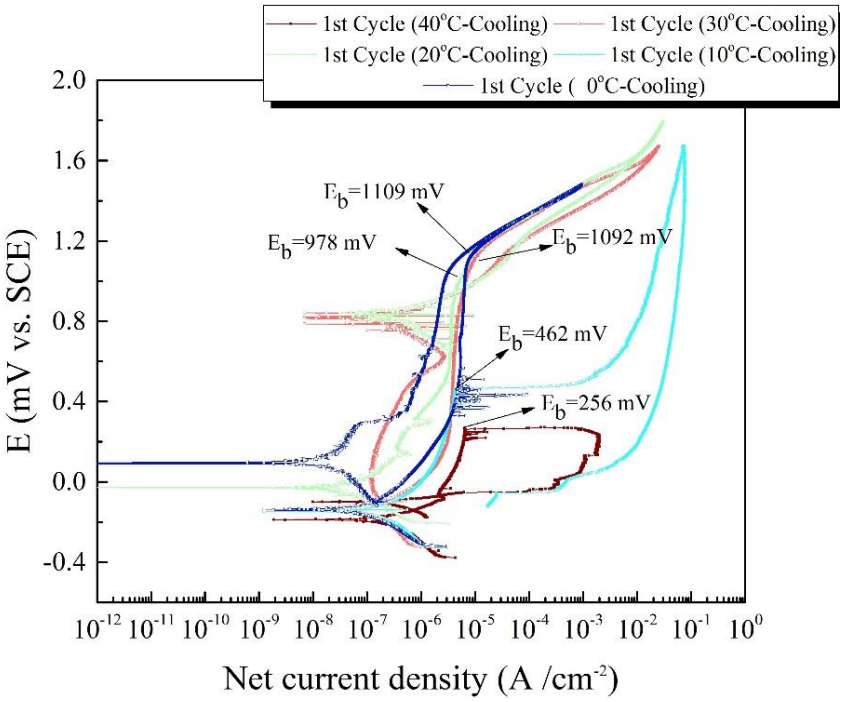

Figure 3.5 cyclic polarization curves for NiTi samples preformed in 3.5 wt% NaCl solution at different temperature from 0°C to 40°C.

The potentiodynamic polarization parameters are shown in Table 5. It was observed that a significant change in OCP values causes by changing temperature from 40 to 0°C. The increase in OCP value at 20°C follows by peak of forward martensitic transformation (M_P). This change would be explained by evaluation of martensite crystalline structure inside austenite phase and change in anodic and cathodic sites at different temperatures [84]. The value for OCP remains about -125±5 mV vs SCE at 30°C, 10°C and 0°C. The E_{corr} is following the same trend as OCP for all the temperatures. The difference between the OCP and corrosion potential is coming from the effect of scan rate

on the potentiodynamic polarization. This difference is increase with increasing the scan rate.

The breakdown potential (i.e. the pitting potential) at each temperature is the lowest potential that anodic current increases significantly after passivation and indicates the pit initiation [7, 81, 85]. Complete austenite phase at 40°C shows the lower passive layer breakdown potential in comparison to the breakdown potential of the complete martensite phase (0°C and 10°C) and mixture of austenite and martensite phases (20°C and 30°C). The change in the values of E_b at different temperatures appears to be related to a corrosion resistance of the material rather than the change in the oxygen evolution potential. The more noble pitting potential shows the more resistant is alloy to pitting corrosion [9].

A decrease in corrosion rate (i_{corr}) was detected at 20°C where the higher martensite sites and lower austenite sites exist on the sample surface. This corrosion rate drop would be associated to localized corrosion due to micro-galvanic coupling between the high ratio of anodic sites (martensite phase) and less cathodic sites (austenite phase).

Table 5 Polarization parameters for NiTi in 3.5 wt% NaCl at different temperatures.

Temperature (°C)	Microstructure phase	Potentiodynamic polarization parameters					
		β_a (mV dec^{-1})	β_c (mV dec^{-1})	i_{corr} (μA cm^{-2})	E_{ocp} (mV vs. SCE)	E_{corr} (mV vs. SCE)	E_b (mV vs. SCE)
40	A	260	224	0.032	179	188	256
30	M+A	228	293	0.016	-130	137	1092
20	M+A	213	160	0.006	-8	31	978
10	M	337	234	0.019	-127	136	462
0	M	248	178	0.012	-120	146	1109

The results of experimental measurement of cyclic potenitodynamic polarization are used to calculate the activation energy of corrosion reaction for austenite (E_a^M) and martensite (E_a^A) phases. The Arrhenius-type plot (Figure 3.6) shows the correlation between the corrosion current density and temperature for the NiTi alloy. In general, the rate of electrochemical reactions increases with temperature where the temperature favors the kinetics of anodic dissolution of the metal. The Arrhenius equation is represented in equation:

$$i_{\text{corr}} = A\exp\left(\frac{-E_{\text{a}}}{RT}\right) \qquad \text{Eq.3}$$

E_a is the activation energy, i_{corr} is corrosion current density, R and T are universal gas constant and temperature, respectively.

The activation energy is calculated for each phase from the slopes of the Arrhenius lines. Values obtained of E_a^A (63.913 kJ.mol^{-1}) and E_a^M(29.505 kJ.mol^{-1}) for Austenite and Martensite phases, respectively. The high E_a value indicates low corrosion rate value [84]. In this case, the corrosion rate of Austenite phase is lower than Martensite phase. The latter proofs the hypothesis for the micro-galvanic corrosion in presence of mixture of martensite and austenite phases, where martensite phase forming the anodic sites and austenite phase forming the cathodic sites.

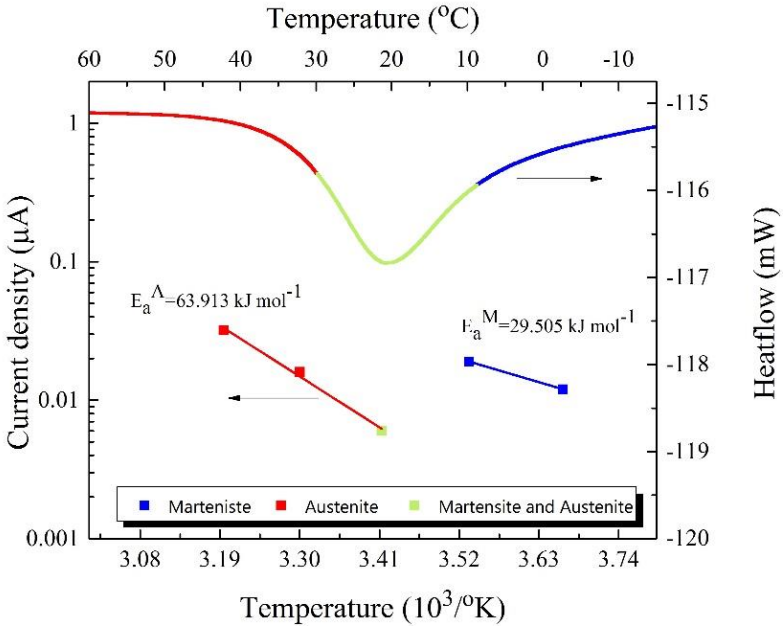

Figure 3.6 Arrhenius plot of NiTi in 3.5 wt% NaCl during cooling cycle from 40°C to 0°C.

In order to clarify the impact of the presence of different ratio of Martensite and Austenite phases, the electrochemical tests that include EIS and potentiodynamic polarization tests were performed in the microcapillary cell in two steps. In step one, the sample was heated above 90ºC and cooled down to room temperature in air to and for the step two, the sample was cooled down below -10ºC and heated up to room temperature. After step one, the sample had higher ratio of austenitic phase and after step two, the sample had higher ratio of martensitic phase.

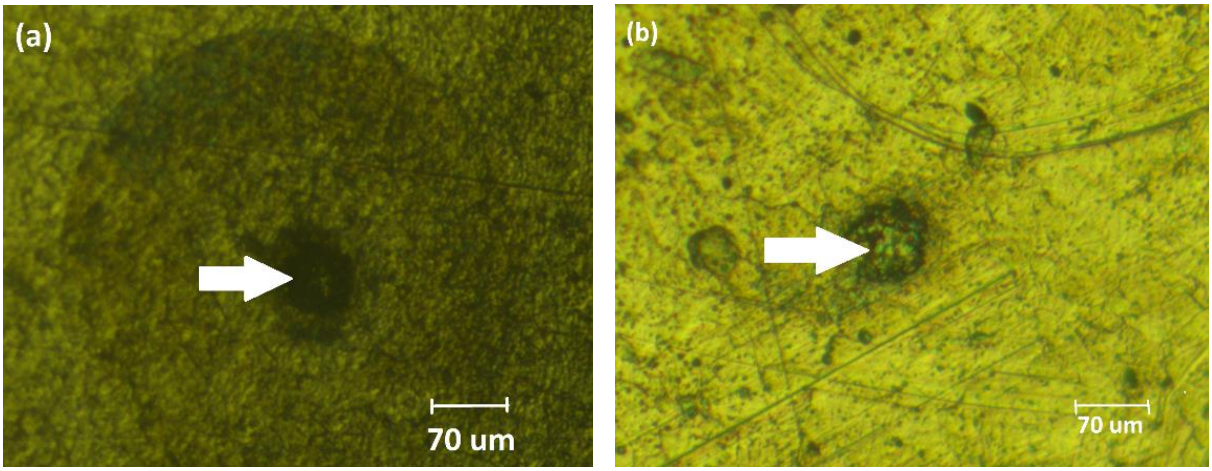

Figure 3.7 Tested point on the surface of NiTi sample for (a) step one with mostly austenitic phase and (b) step two with mostly martensitic phase in the 3.5 wt% NaCl solution with microcapillary cell.

Figure 3.7 (a) and (b) show the tested points of austenite and martensite, respectively, obtained in the microcapillary cell. The diameter of tested point is ~70 µm.

Figure 3.8 shows the potentiodynamic polarization curves for NiTi alloy in both steps. The polarization curve of the sample in step one with mostly austenitic phase is characterized by higher passivation current density. The corrosion potential of mostly martensite phase (step two) is found to be slightly nobler than the one for mostly martensite phase (step one), indicating that martensite phase is nobler than austenite in this material.

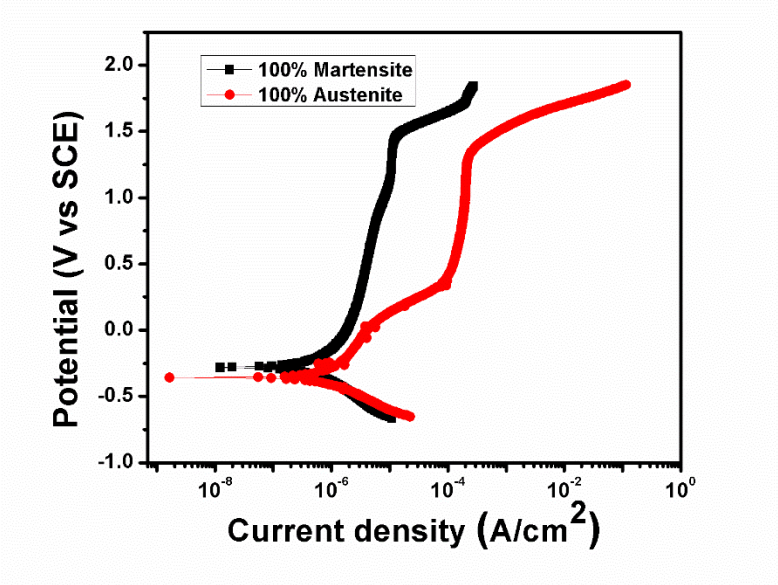

Figure 3.8 Potentiodynamic polarization curves for mostly martensite and mostly austenite tested in the microcapillary cell in 3.5% NaCl solution.

The values of E_{corr}, i_{corr} and passivation current density (i_{pass}) are extracted from the curves and shown in Table 6. The corrosion potential of martensite phase is ~ -250 mV vs SCE while the one for austenite is ~ 400 mV vs SCE. Passive film is more easily

formed on the mostly martensite in 3.5 wt% NaCl, as suggested by its lower passive current density (Figure 3.5). The passive current density of the mostly martensite phase is ~ 2.1 µA.cm^{-2} while the one for austenite is 2.9 µA.cm^{-2}. The passive window in the martensite phase is more stable over a wide range of potential up to ~1500 mV vs SCE where the oxygen evolution may occur at this potential in the microcapillary cell. In contrast, the austenite phase presents a breakdown potential at a lower potential (~ 100 mV vs SCE) that might be attributed to the oxidation of corroding species (Titanium and Nickel) to a higher oxidation state. The material then repassivate at ~300 mV SCE before it shows a breakdown potential at a higher potential (~1500 mV SCE) corresponding to oxygen evolution. The wide range of passivation of martensite phase, lower passive current density of martensite, and lower breakdown potential of austenite obtained in the microcapillary cell are in agreement with the ones obtained in the Avesta cell in Figure 3.8.

Table 6 Potentiodynamic polarization parameters for NiTi in 3.5 wt% NaCl with microcapillary test setup.

	Phase	i_{corr} (µA.cm^{-2})	i_{pass} (µA.cm^{-2})	$E_{B,low}$ (V vs SCE)
Step one	Mostly Austentie	1.1	2.1	N/A
Step two	Mostly Martensite	2.1	2.9	0.1

The impedance spectra in Figure 3.9 shows three different regions referring to values of the high, medium 10 <f < 103 and low frequencies [86]. The high frequency values of complex impedance |Z| shows the capacitance loop (semicircle) which includes the 160 electrolyte resistance [87], current and potential distribution due to geometry of cell [88], impedance of the electronic components of the potentiostat [89] and the reference electrode.

The time constant at high frequency dominates in the region of 10kHz. There is an uncertainty about origin of the capacitive loop at high frequency for passivated film on the surface of titanium alloys. It would be associated to the uncompensated ohmic resistance due to electrolyte solution [90, 91], the porous layer formation on the surface of electrolyte [92] and affected data because of potentiostat setting [93].

NaCl is acting as supportive electrolyte because solution anion (Cl^-) and cation (Na^+) do not form special compounds. However high concentration Chloride anions in acidic solution (low pH) can promote passivation and surface oxide layer break down, according to the reaction 1 and 2, respectively [94, 95]:

$$Ti \xrightarrow{+4Cl^-} TiCl_4{}^4 \xrightarrow{+2H_2O} TiO_2 + 4Cl^- + 4H^+ (1)$$

$$TiO_2 + 4H^+ + xCl^- \rightarrow Ti4^+ + 2H_2O + xCl^- (2)$$

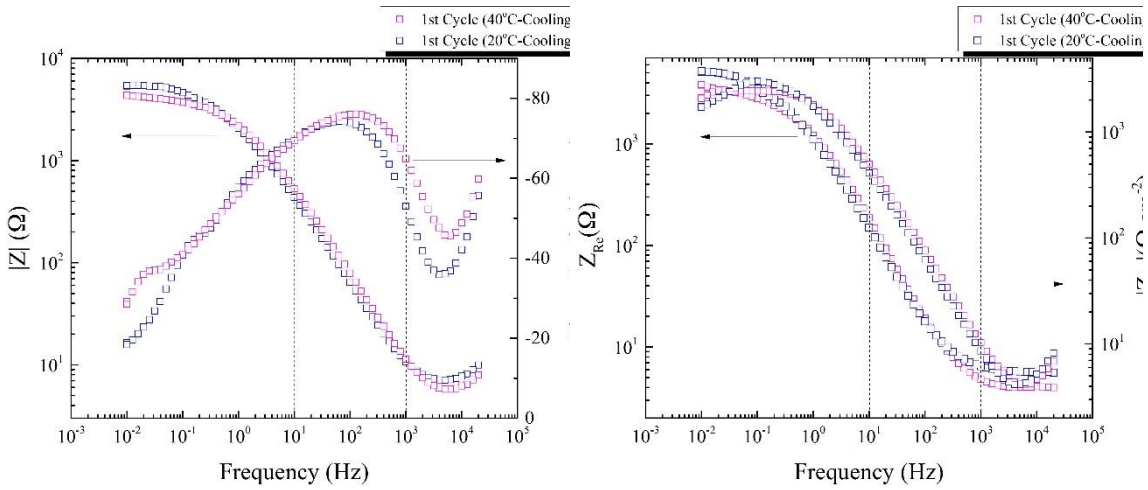

A B

Figure 3.9 (A) Bode plot of EIS spectra and (B) Imaginary and real part of impedance data vs. frequency obtained during cooling in first thermal cycle at 20°C and 40°C

Figure 3.9-A shows a capacitance typical behavior at medium frequency range that represents a time constant describing the formation of stable film on the surface NiTi sample. The time constant has shifted towards lower frequencies as the temperature of the electrolyte solution decreasing from 40°C to 20°C. Figure 3.9-A represents a deviation for phase shift responses of NiTi at 20°C and 40°C. This deviation presence of a second time constant at 40°C where the phase transformation is starting with respect to DSC results. Forward martensitic transformation leads to passive layer breakdown which conclude to higher charge transfer at 40°C and presenting the second time constant at lower frequency.

To investigate the sensitivity of electrolyte to temperature, the resistance of bulk electrolyte measured from EIS results at each temperature. The real part of impedance data

considers to be related to the conductive aqueous solution resistance. Figure 3.10-A shows the real impedance values in frequency above the 5 kHz at different temperature.

The electrolyte ohmic resistance value is $6.5 \pm \omega^{-1}$ during thermal cycling. The imaginary values reveal the presence of higher admittance objects which would cover the value of outer porous layer in titanium alloys [43].

In case of presence of high conductive supporting electrolyte, the media electrical conductivity (reciprocal of electrolyte resistance) are following Arrhenius equation (Figure 3.10-B). The activation energy for charge transport process of supporting electrolyte ions is changing with temperature and is not interfering with applied AC potential [96, 97]. The impedance data above the 5 kHz is not included in high frequency data analysis due to avoid difficult fitting analysis [39, 44].

Figure 3.9 shows the Nyquist diagram for the NiTi sample during cooling at first thermal cycle from 40°C to 0°C with 10°C decrement. Impedance spectra of NiTi alloys in 3.5 wt% NaCl solution shows one depressed semicircle for all temperatures which is characteristic of passivated Titanium based alloy [98, 99]. The impedance responses in medium frequency region (103 to 10 Hz) has the maximum phase angle (Figure 3.9-A). This increasing in phase angle with decreasing frequency exhibits the near-capacitive behavior of the electrode [100]. The dielectric properties of the surface film can be described at high to medium frequencies [86].

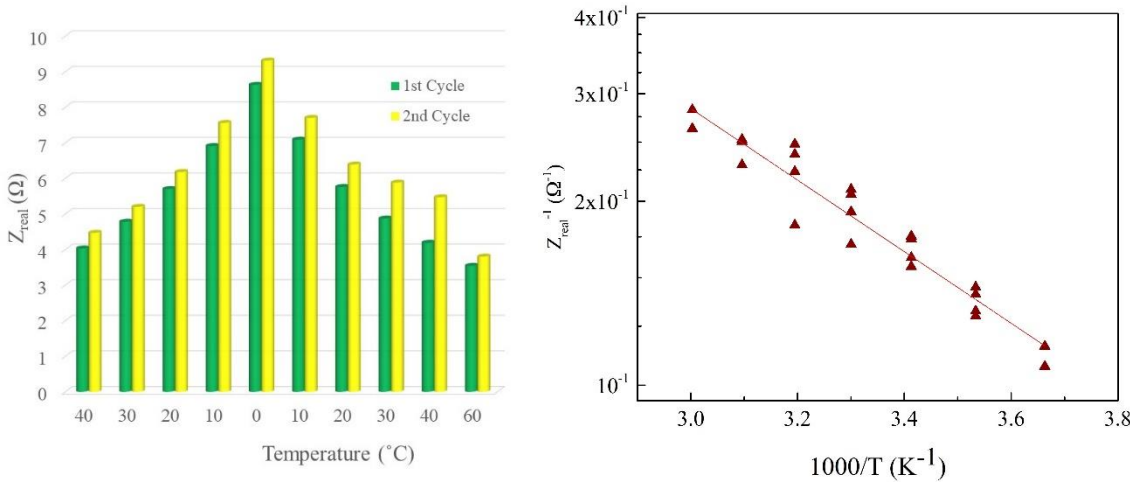

A B

Figure 3.10 (A) Real part of impedance vs temperature during thermal cycling between 0°C and 60°C. (B) The reciprocal of the real impedance at high frequency with temperature during thermal cycling.

The electron charge transfer (faradic charge transfer) and the mass transfer processes at the film-electrolyte interface appear at low frequency region (less than 10 Hz). The diameters of the depressed semicircle are increased (at low frequency) with decreasing of temperature, indicating the increase in resistance of ions transfer and faradic reaction on the surface of electrode. The bode plots of NiTi (Figure 3.11-B) at different temperatures has a time constant in range of medium frequency.

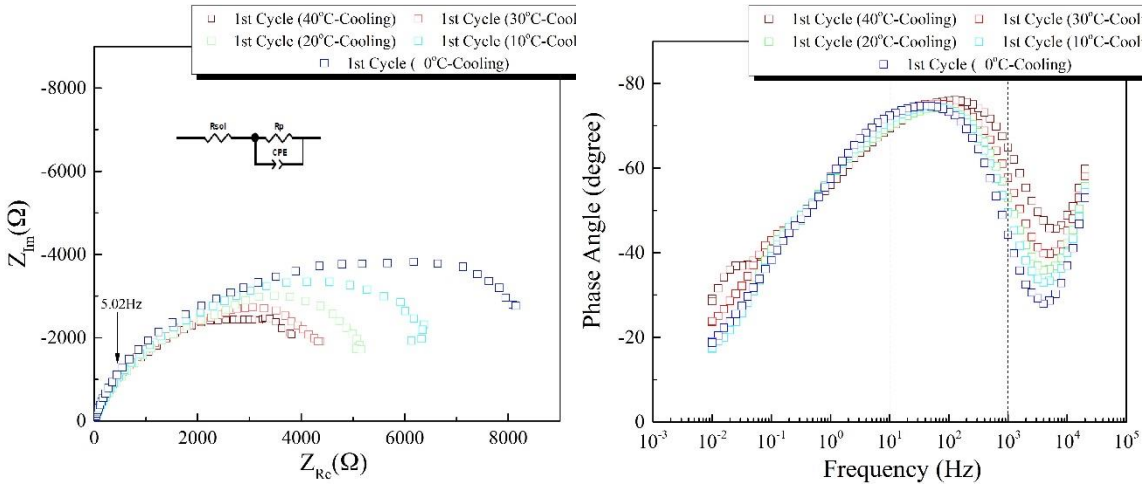

A B

Figure 3.11 (A) Nyquist diagram and (B) Bode plot of NiTi alloy in 3.5 wt% NaCl solution during thermal cycling from 40°C to 0°C.

Figure 3.11 shows the capacitive charge with temperature. The capacitance magnitude decreased with temperature. The formed passive layer is a semiconductor formed by the austenite phase presented at the surface. Decreasing the temperature influence the thickness and passive layer formation.

The electrochemical system can be modeled by an electrical equivalent circuit which is adopted to the impedance data. In the model, solution resistance and faradic charge transfer (polarization resistance) are represented by R_{sol} and R_p respectively. The following equation describes the impedance of the electrical equivalent circuit shows in Figure 3.11-A [101].

$$Z(\omega) = R_{sol} + \frac{R_p}{1 + Q(j\omega)^{\alpha} R_p} \qquad \text{Eq.4}$$

A Constant Phase Element (CPE) represents the pseudocapacitive behavior of electrode in parallel with polarization resistance [102]. The impedance of CPE is expressed by equation (5).

$$Z_{CPE}(\omega) = \frac{1}{Q}(j\omega)^{-\alpha} = \frac{\omega^{\alpha}}{Q}[\cos(\frac{\alpha\pi}{2}) - j\sin(\frac{\alpha\pi}{2})] \qquad \text{Eq.5}$$

where $\omega = 2\pi f, 0 < \alpha < 1$, and Q is the CPE constant in $\Omega^{-1}cm^{-2}s^{n}$ [103].

For Ω = 1 CPE stands for resistance and for Ω = 0 it represents ideal capacitance. The physical meaning of CPE is not clear. The different physical source has been proposed to be the origin of this capacitance distribution e.g. electrode porosity, surface roughness and inhomogeneity, slow adsorption reactions and Non-uniform potential and current distribution [104].

The CPE parameters (α and Q) are estimated from two principal approaches in literature: the complex nonlinear-least-squares (CNLS) fitting of impedance to the electrical equivalent circuit and the analysis the of the imaginary part of the impedance in frequency region from 10 to 103Hz [105, 106].

CNLS software Echem analyst from Gamry are used to find α_{EQ} and Q_{EQ} from analyzing all data with the electrical equivalent circuit (Table 7).

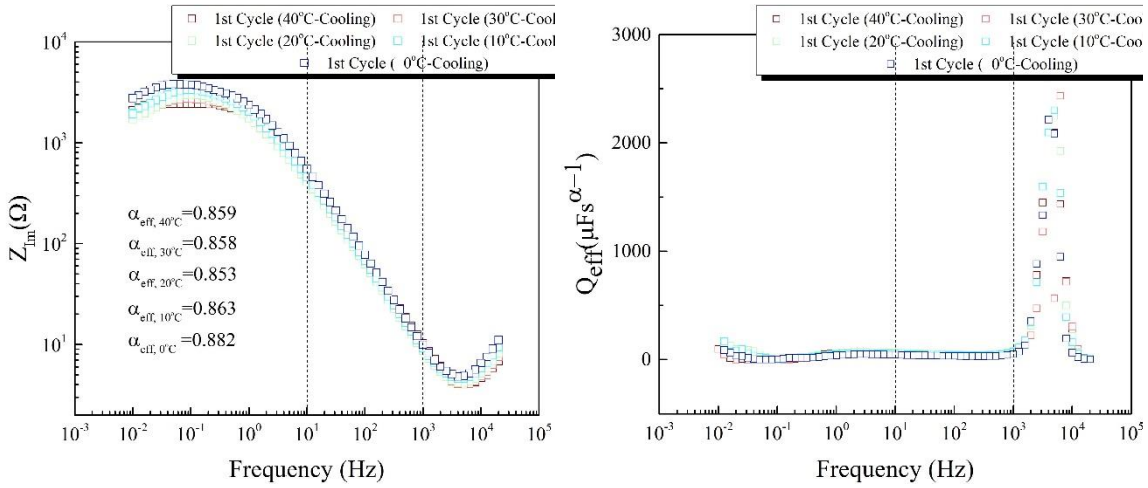

A B

Figure 3.12 (A) the plot of the logarithm of the imaginary part of the impedance and (B) effective CPE coefficient versus frequency.

An effective CPE coefficient (or an effective capacitance when α= 1) my obtained according to equation (6) [107].

$$Q_{eff} = sin(\frac{\alpha_{eff}\pi}{2})\frac{-1}{(2\pi f^{\alpha_{eff}} Z_{\mathrm{Im}}}] \qquad \text{Eq.6}$$

The effective CPE exponent (α_{eff}) can be calculated from the slope of the logarithmic plot of imaginary part of the impedance by [56]:

$$Q_{eff} = sin(\frac{\alpha_{eff}\pi}{2})\frac{-1}{(2\pi f)^{\alpha_{eff}} Z_{\mathrm{Im}}} \qquad \text{Eq.7}$$

The characteristic frequency is defined by presence of maxima where the slopes before and after this frequency are +α and -α, respectively.

The calculated effective constant coefficient with equation (7) and (8) shows in the Figure 3.12-B as a function of frequency on logarithmic scale for the first cooling cycle.

The double layer capacitance (C_{dl}) can be calculated from Q_{eff} and α_{eff} in the system inducing one CPE from the following equation [108]:

$$C_{dl} = Q_{eff}\omega_m^{'} \qquad \text{Eq.8}$$

Where ω is the characteristic angular frequency.

Table 7 The constant phase element (CPE) parameters are calculated by CNLS fitting of equivalent circuit at different temperatures between 0°C and 60°C for thermal cycling of NiTi alloy in 3.5 wt% NaCl solution.

Temperature (˚C)	Cycling	α_{EQ}	Q_{EQ} (μFs$^{\alpha-1}$)	R_p (kOhm)
40	Cooling	0.816	67.9	2829
30		0.833	71.97	3326
20		0.804	88.93	4463
10		0.812	77.62	5308
0		0.826	62.19	5750
10	Heating	0.828	59.8	5521
20		0.824	57.43	5354
30		0.814	62.87	5002
40		0.790	75.76	5002
50		0.776	91.36	4022
60		0.759	104.9	3693
50	Cooling	0.767	100.5	3973
40		0.807	71.94	5664
30		0.824	62.09	5679
20		0.822	63.09	7080
10		0.826	58.45	7517
0		0.835	48.54	7537
10	Heating	0.832	50.62	7540
20		0.823	51.71	7180
30		0.823	49.08	7251
40		0.822	48.45	7315
50		0.784	75.6	4603
60		0.786	75.44	3340

The trend for α values in Table 7 and Table 8 indicate a good capacitive behavior of the surface layer where the calculated values by each method are close to unity. The values show the magnificence change at temperature 40˚C during heating, where the material is completely austenite. The Austenite finish temperature can be considered as a critical point where the roughness of surface is changing with changing by having fully austenite material. This is in agreement with the studies on changing on the roughness of NiTi during thermal cycling [109, 110].

The changes in α value and deviation from idea capacitive behavior ($\alpha = 1$) is consequence of surface disorder upon the forward and reverse transformations [111]. The different crystallographic orientations of austenite and martensite lead to different capacitive and conductive properties could cause a time constants distribution.

Cdl values obtained at martensite phase (lower temperatures) has the lower values compare to austenite values (higher temperatures) which is related to decreasing of the effective surface area of samples at lower temperature (martensite). Figure 3.13 shows the EIS signal obtained at step one and two for mostly austenitic and martensitic phases, respectively. Nyquist plots (Figure 3.13) of mostly martensite and austenite phase show one capacitive behavior and a Warburg impedance for each phase. The diameter of capacitive loop for the mostly martensite phase was found bigger than the one for the mostly austenite which roughly indicate that the mostly martensite phase is more corrosion resistant. From the phase angle plots (Figure 3.14), both plots show only one time constant plus a Warburg impedance.

Table 8 presents the calculated CPE parameters and characteristic angular frequency during thermal cycling at different temperatures. C_{dl} values obtained at different temperature follow the order similar to that obtained for i_{corr}.

The trend for α values in Table 7 and Table 8 indicate a good capacitive behavior of the surface layer where the calculated values by each method are close to unity. The values show the magnificence change at temperature 40˚C during heating, where the material is completely austenite. The Austenite finish temperature can be considered as a critical point where the roughness of surface is changing with changing by having fully austenite material. This is in agreement with the studies on changing on the roughness of NiTi during thermal cycling [109, 110].

The changes in α value and deviation from idea capacitive behavior ($\alpha = 1$) is consequence of surface disorder upon the forward and reverse transformations [111]. The different crystallographic orientations of austenite and martensite lead to different capacitive and conductive properties could cause a time constants distribution.

Cdl values obtained at martensite phase (lower temperatures) has the lower values compare to austenite values (higher temperatures) which is related to decreasing of the effective surface area of samples at lower temperature (martensite). Figure 3.13 shows the EIS signal obtained at step one and two for mostly austenitic and martensitic phases, respectively. Nyquist plots (Figure 3.13) of mostly martensite and austenite phase show one capacitive behavior and a Warburg impedance for each phase. The diameter of capacitive loop for the mostly martensite phase was found bigger than the one for the mostly austenite which roughly indicate that the mostly martensite phase is more corrosion

resistant. From the phase angle plots (Figure 3.14), both plots show only one time constant plus a Warburg impedance.

Table 8 The constant phase element (CPE) parameters at different temperatures between 0°C and 60°C for thermal cycling of NiTi alloy in 3.5 wt% NaCl solution.

Temperature (˚C)	Cycling	α_{eff}	ω_{eff} (radian.s^{-1})	Q_{eff} (μF$s^{\alpha-1}$)	Cdl (μF)
40	Cooling	0.859	0.158	49.6	64.32
30		0.858	0.5	47.27	52.16
20		0.853	0.63	51.22	54.83
10		0.863	0.5	44.93	49.03
0		0.882	0.315	35.7	40.91
10	Heating	0.878	0.5	34.73	37.79
20		0.873	0.5	32.96	35.99
30		0.857	0.793	37.14	38.39
40		0.827	0.5	42.91	48.37
50		0.817	0.5	48.75	55.34
60		0.795	0.5	54.92	63.31
50	Cooling	0.81	0.63	51.55	56.29
40		0.851	0.998	41.63	41.64
30		0.859	0.315	38.61	45.43
20		0.869	0.63	37.59	39.93
10		0.867	0.397	36.31	41.06
0		0.881	0.63	30.5	32.22
10	Heating	0.87	0.5	33.31	36.45
20		0.866	0.5	30.76	33.75
30		0.861	0.5	29.91	32.93
40		0.863	0.5	31.17	34.28
50		0.82	0.5	41.05	46.5
60		0.812	0.63	51.04	55.68

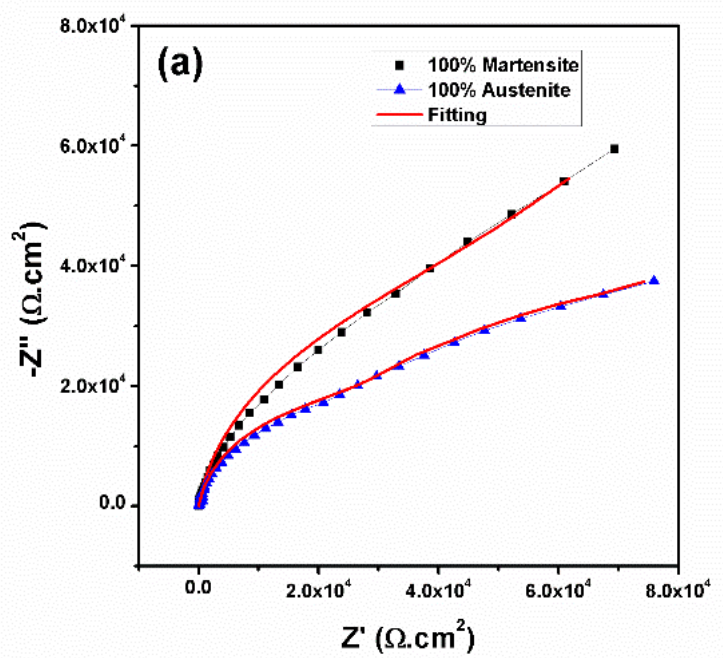

Figure 3.13 Nyquist plot for mostly martensite and mostly austenite tested in the microcapillary cell in 3.5% NaCl solution.

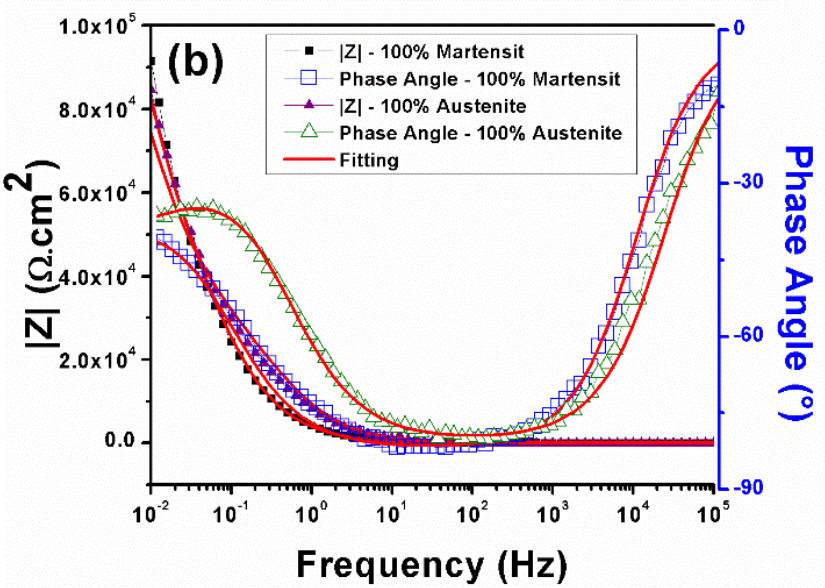

Figure 3.14 Bode plot for mostly martensite and mostly austenite tested in the microcapillary cell in 3.5% NaCl solution.

The electrochemical system can be modeled by an electrical equivalent circuit (EEC) which is adopted to the impedance data. In the model, solution resistance and polarization resistance (faradic charge transfer) are represented by R_s and R_p respectively. A Warburg impedance *(W_d)* is related to the diffusional impedance of electrochemical system. A Constant Phase Element (CPE) represents the pseudocapacitive behavior of electrode in parallel with polarization resistance [102]. The physical meaning of CPE is not clear. The different physical source has been proposed to be the origin of this capacitance distribution e.g. electrode porosity, surface roughness and inhomogeneity, slow adsorption reactions and Non-uniform potential and current distribution [104]. Figure 3.15-a shows the EEC used to analysis the impedance spectra obtained from electrochemical measurement by microcapillary setup.

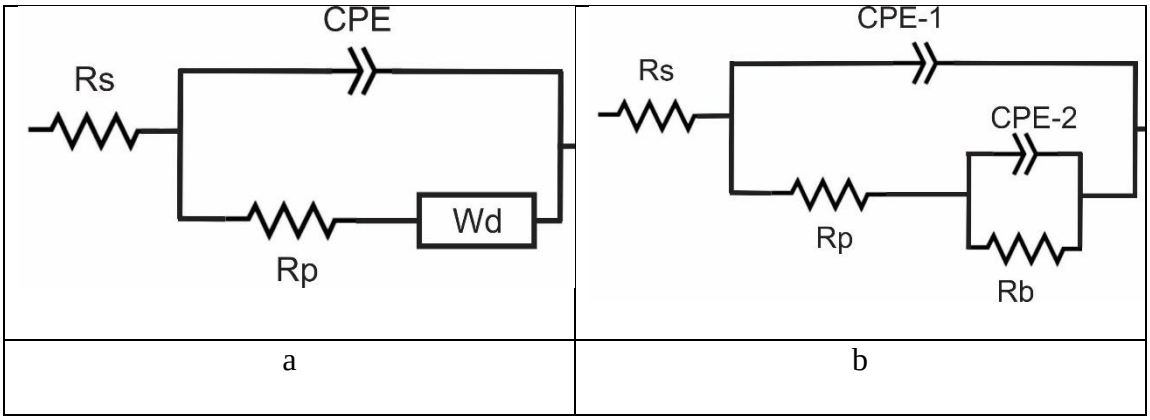

Figure 3.15 Equivalent circuit used for representing the impedance response of the NiTi alloy in 3.5 wt% NaCl solution from (a) Microcapillary, and (b) Thermal cycling.

The impedance magnitude of the mostly martensite phase which is found to be higher than the one for the mostly austenite phase indicates that the martensite is more resistant to corrosion (Figure 3.14).

The higher R_p value, which is inversely proportional to the corrosion rate, for the mostly martensite (50.160 $k\Omega.cm^2$) phase suggests that the corrosion rate of martensite is lower than the austenite (28.424 $k\Omega.cm^2$) (Table 9).

NiTi sample has lower capacitance value after step one (mostly austenite phase) in comparison with step two (mostly martensite phase). The inverse relation between capacitance value and oxide layer thickness indicates that the NiTi sample mostly in martensite phase has a thick passive film compared to mostly in austenite phase.

The corrosion current density of 1.1 $\mu A.cm^{-2}$ (Table 6), the corrosion rate of sample when the martensite phase is lower than the austenite phase that has a corrosion current density of 2.1 $\mu A.cm^{-2}$. This trend is in agreement with the R_p values obtained by EIS (Table 9).

Table 9 Electrochemical parameters obtained from EIS of NiTi alloy in 3.5 wt% NaCl solution at room temperature after step one (cooling) and step two (heating)

	Phase	Rs $\Omega.cm^2$	Y_0 ($\mu F*S^{n-1}*cm^{-2}$)	α	Rp $k\Omega.cm^2$
Step one	Mostly Martensite	1.7	0.01	0.9	50.160
Step two	Mostly Austenite	1.1	42.6	0.9	28.424

In order to clarify the effects of phase transformation and temperature on the corrosion behavior of NiTi, EIS were performed in 3.5 wt% NaCl solution during thermal cycling from 0°C to 60°C. These different temperatures were used with the aim of differentiating the impact of temperature and presence of different phases while material experiencing reverse and forward martensite transformation. Figure 3.16 to Figure 3.19 shows the Nyquist diagrams for the NiTi sample during thermal cycling. Impedance spectra of NiTi alloys in 3.5 wt% NaCl solution shows two depressed semicircles for all temperatures which is characteristic of passivated Titanium based alloy [98, 99]. The electron charge transfer (faradic charge transfer) and the mass transfer processes at the film-electrolyte interface appear at low frequency region (less than 10 Hz). The diameters of the depressed semicircle are increased (at low frequency) with decreasing of temperature, indicating the increase in resistance of ions transfer and faradic reaction on the surface of electrode(Figure 3.16 and Figure 3.17). The presence of second depressed semicircle is more obvious during second thermal cycling (Figure 3.18 and Figure 3.19). This would be due to growing the oxide layer by time and forming new protective passive layer. The new formed passive layer at the end of first cycle can resist the strain due to phase transformation during second thermal cycling (Figure 3.18 and Figure 3.19).

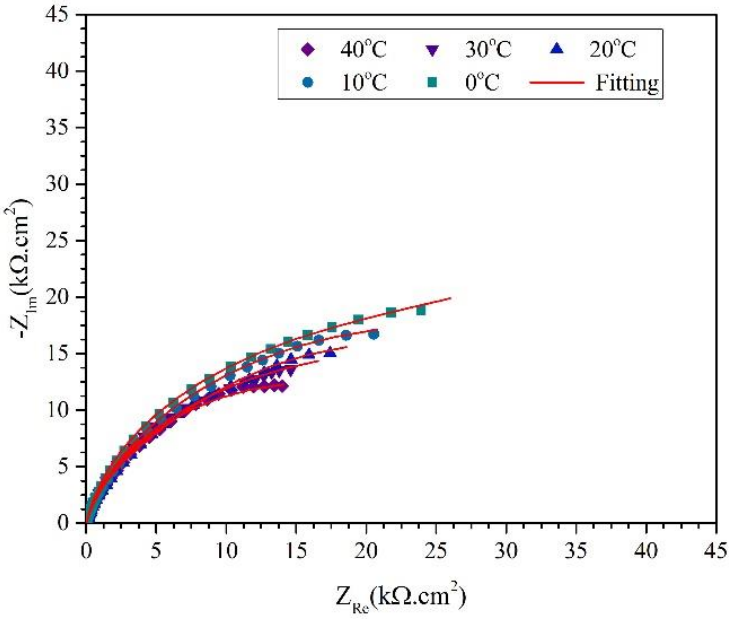

Figure 3.16 Nyquist diagram of NiTi alloy in 3.5 wt% NaCl solution during thermal cycling from 40°C to 0°C (First cycle cooling).

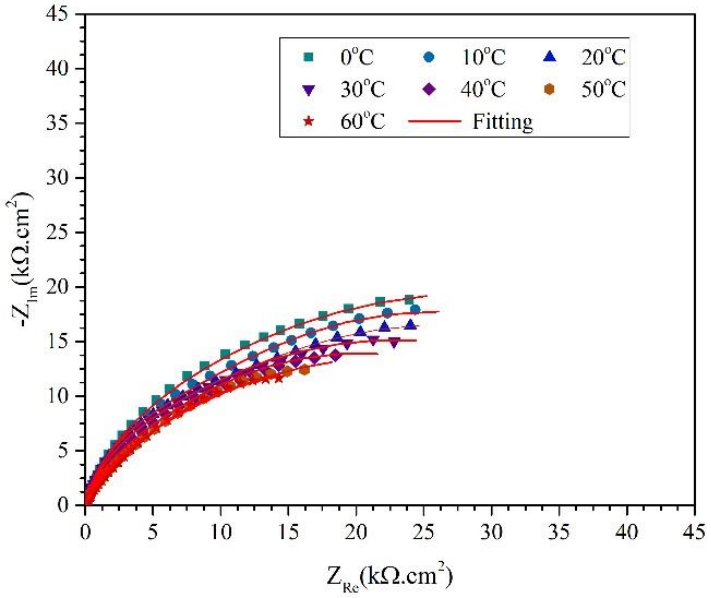

Figure 3.17 Nyquist diagram of NiTi alloy in 3.5 wt% NaCl solution during thermal cycling from 0°C to 60°C (First cycle heating).

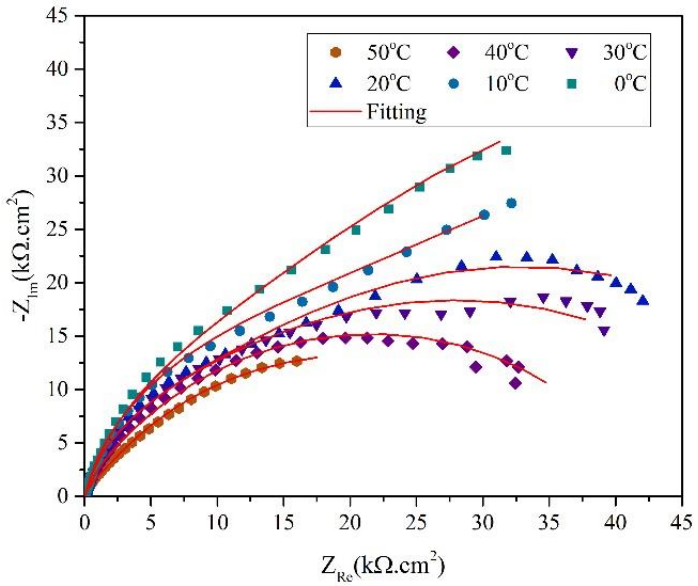

Figure 3.18 Nyquist diagram of NiTi alloy in 3.5 wt% NaCl solution during thermal cycling from 60°C to 0°C (Second cycle cooling).

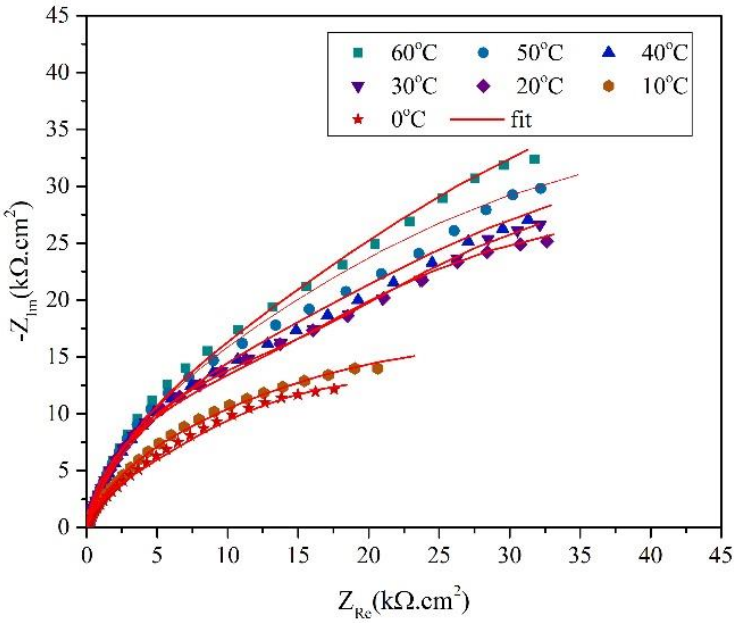

Figure 3.19 Nyquist diagram of NiTi alloy in 3.5 wt% NaCl solution during thermal cycling from 0°C to 60°C (Second cycle heating).

Table 10 Electrochemical parameters obtained from EIS of NiTi alloy in 3.5 wt% NaCl solution at different temperatures between 0˚C and 60˚C during thermal cycling.

Temperature (˚C)	Cycling	R_s ($\Omega.cm^2$)	R_{pore} ($k\Omega.cm^2$)	R_p ($k\Omega.cm^2$)	Q_1 ($S\times s^n\times10^{-4}$)	α_1	Q_2 ($S\times s^n\times10^{-4}$)	α_2
40		2.542	0.82	5.50	4.14	0.89	2.61	0.85
30		3.123	3.93	4.51	4.10	0.76	1.80	0.89
20	Cooling	3.873	4.74	3.59	2.32	0.86	1.42	0.89
10		5.776	5.60	4.90	2.31	0.60	1.46	0.87
0		6.899	5.92	5.28	2.31	0.75	1.06	0.89
10		5.509	5.04	4.29	2.22	0.91	0.84	0.92
20		4.594	4.64	4.88	2.84	0.85	0.95	0.87
30	Heating	3.72	4.51	4.00	2.24	0.81	0.92	0.90
40		2.706	4.15	3.42	1.99	0.84	1.11	0.87
50		2.47	4.73	3.64	2.80	0.73	1.40	0.82
60		3.548	4.18	3.01	2.01	0.76	2.10	0.80
50		2.971	4.87	1.16	1.48	0.70	1.12	0.83
40		3.207	5.01	3.35	1.90	0.79	1.70	0.85
30	Cooling	5.407	5.68	4.89	4.31	0.78	1.92	0.90
20		5.862	6.72	5.22	4.82	0.86	1.95	0.89
10		7.963	12.8	7.72	2.76	0.83	0.80	0.90
0		7.569	12.7	9.00	1.63	0.89	0.86	0.88
10		6.62	10.7	7.59	1.48	0.83	0.74	0.89
20		3.263	9.84	7.89	2.02	0.89	0.75	0.86
30	Heating	4.445	9.29	6.18	2.22	0.95	0.61	0.93
40		3.946	9.43	5.12	1.82	0.88	0.55	0.95
50		2.909	8.04	3.63	2.34	0.61	0.89	0.83
60		2.666	6.07	2.07	2.37	0.73	0.91	0.86

Table 10 shows the EIS parameters obtained from fitting the EIS spectra with EEC (Figure 3.15-b). The different values of CPE parameters observed for different

temperatures attribute to the different phase distribution on the surface. CPE values obtained at martensite phase (lower temperatures) has the lower values compare to austenite values (higher temperatures) which is related to decreasing of the effective surface area of samples at lower temperature (martensite).

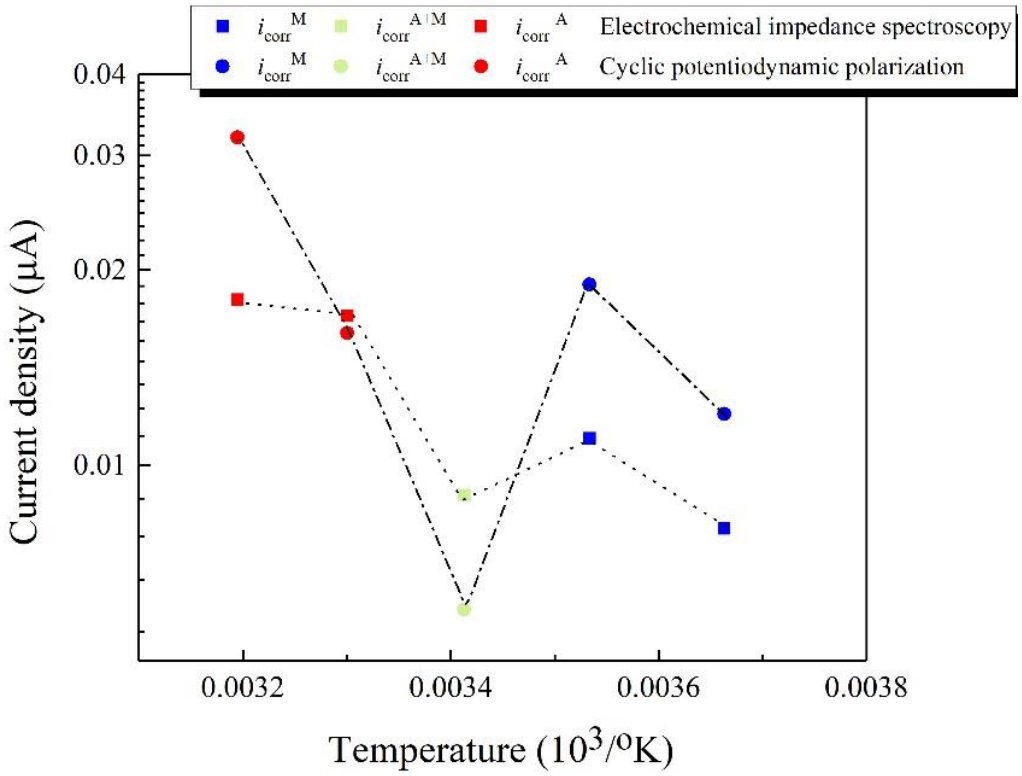

Figure 3.20 Arrhenius plots of the corrosion rate calculated from results of cyclic potentiodynamic polarization and electrochemical impedance spectroscopy.

Figure 3.20 displays the Arrhenius plot for the corrosion current density of NiTi SMA.

Figure 3.20 represents the corrosion current density values calculated using both EIS (during first cooling cycle) and cyclic potentiodynamic polarization methods. A sharp dropped is observed in the corrosion current densities from both methods in Figure 3.20. This deviation from Arrhenius type dependency is observed between the corrosion current density and temperature during martensitic phase transformation. The difference among corrosion current densities calculated with EIS and measured from cyclic potentiodynamic polarization in

Figure 3.20 is coming from the nature of current applied for each method. EIS is measured by polarizing the NiTi sample 10 mV vs. E_{OCP} where in cyclic potenitodynamic polarization, the NiTi sample is polarized -200mV vs E_{OCP} in cathodic branch and 1600 mV vs E_{OCP} in Anodic branch. Therefore, corrosion current density is measured in virgin surface with EIS method and in polarized surface with cyclic potentiodynamic polarization method.

Studies shows the metal dissolution of titanium alloys in NaCl solution is following the Arrhenius law where there is a linear relation between corrosion current density and temperature. The observed deviation from Arrhenius behavior in this study is related to change in surface roughness due to phase transformation and changing in crystallographic orientation from martensite to austenite phase. The deviation from Arrhenius behavior could be related to the breakdown of the formed passive oxide layer on the surface upon the changing phase during phase transformation. Moreover, two dissimilar crystallographic structure presenting can lead to increase corrosion rate with forming local galvanic corrosion cell on the surface.

3.4 Summary

The current investigation aims in understanding the effect of phase transformation on the corrosion behavior of nickel-titanium (NiTi) shape memory alloy (SMA). The interfacial mechanisms of passive oxide formation or dissolution in presence of different phases at different temperature is studied by general and localized electrochemical measurements. Localized assessment and passive oxide film behavior of NiTi SMA after exposure to a corrosive media are investigated by cyclic potentiodynamic polarization. The cyclic potentiodynamic test results have showed that the change in temperature has a significant influence on the corrosion parameters of the NiTi. The Results show the corrosion rate is controlled by both the metal oxidation and phase transformation process. An electrochemical microcapillary cell has been used to characterize the local vs. general behavior based on two phase transformations. It is observed that the martensite phase has lower passive current density and higher breakdown potential in comparison with austenite phase.

4. EFFECT OF THERMOMECHANIL TRANSFORMATION ON THE CORROSION BEHAVIOR OF SHAPE MEMORY ALLOY

4.1 Introduction

Slightly Ni-rich compositions of about 50.1–52 at. % Ni merged as a popular material for the biomedical industry because of their distinctive super elastic properties and shape memory effects at body-temperature. The corrosion resistance of NiTi relies heavily on the surface oxide film which acts as a barrier against corrosive species (e.g. Cl^-). The characteristics and composition of the oxide film on NiTi can be significantly altered by fabrication process and depend on the type of process that materials experienced (e.g. preheating, heat treatment, surface finishing, etc.) [7]. The surface oxide layer is principally amorphous TiO_2 with small amounts of Ti sub-oxides (TiO and Ti_2O_3) and Ni oxidized species. The protection of NiTi surface against anodic corrosion or hydrogen embrittlement relies heavily on this oxide film [6].

While the mechanical properties, fatigue lifetime in air, fracture properties of NiTi SMA have been studied extensively [22, 30, 112-117], there is little information regarding the corrosion behavior of SMA under fatigue and the mechanism of the corrosion fatigue of SMA is not known yet.

Studies have indicated the presence of liquids and ions decrease lifetime of the SMAs. Pyramik et al examined the fatigue resistance of NiTi and CuNiTi orthodontic wires subjected to dynamic stress while immersed into different fluids at constant temperature has been investigated. Their study found lower lifetime for NiTi wires immersed in fluids compared to the same type of wires in air[118]. Raceck et al studied

the corrosion fatigue of super-elastic NiTi subjected to cyclic mechanical loading in a simulated body fluid. Their study correlated the open circuit potential measurement to cyclic mechanical loading. They showed the localized strain in shear bands causes passive oxide layer on the surface cracked locally during the fatigue cycle. The crack opening/closing and passivation mechanisms are competing of opened cracks on the surface oxide upon the cyclic loading[23].

Chan investigated the corrosion fatigue fracture of laser welded NiTi using bending rotation fatigue test in the Hank's solution at constant body temperature. Their works showed the change of the oxide film composition as a consequence of film rapture and repasssivation during fatigue cycles[119].

Darvell et al discussed the low-cycle fatigue (LCE) behavior of NiTi in different corrosive and non-corrosive environment. They reported that the testing in solution contains chloride ions produced the shortest fatigue life and the solution contains chloride was more detrimental to fatigue lifetime [18, 19, 120]. Lagoudas et al studied the interaction between thermally induced transformation fatigue lifetime CuNiTi and presence of corrosive environment. They found the combination of corrosive environment and thermally induced phase transformation lead to reduction of fatigue lifetime of CuNiTi. Their study revealed that the corrosion is more severe in the case of partial transformation cycles compare to the complete transformation cycles [20, 22]. In spite of the attention paid to study the corrosion of NiTi, it is not still clear how the surface oxide layer changes are exactly related to the corrosion fatigue. Reliable experimental data that

considers the correlation among the surface oxide layer changes due to microstructure evolution and corrosion performance during structural fatigue are still missing.

The existing studies on corrosion fatigue of SMA focus mainly on stress level and exclude the effect of temperature on corrosion behavior of SMA. Therefore, the aim of this study was to investigate the corrosion behavior of NiTi SMA under actuation fatigue while is immersed in corrosive fluid. Particular focus is devoted to elucidating the role of surface oxide films on NiTi in the corrosion actuation fatigue process in Ringer's solution. The SMA material is actuated by heating while specimen is subject to constant stress and is thermally cycled. The corrosion responses of NiTi SMA during Thermal actuation allow to take into account the cumulative impacts of mechanical force, temperature and phase transformation on breakdown the passive layer, forming pits and repassivation of SMA.

4.2 Experimental

4.2.1 Materials characterization

In the present study a binary NiTi alloy was provided by ATI Inc, with a nominal composition of Ni 49.5 at% - Ti 50.5 at%. The transformation temperatures of as-received material were measured by a Perkin-Elmer Pyris 1 Differential Scanning Calorimeter (DSC). The specimen was heated up to 200ºC and cooled down to -40ºC with a rate of 10ºC/min for three cycles. The specimen was held for 1 minutes at the highest and the lowest temperature to establish thermal equilibrium.

The measured transformation temperatures of the NiTi-SMA are reported in Table 11. The martensite start (M_s) and Martensite finish (M_f) are associate to the forward

martensite transformation temperatures of NiTi-SMA on cooling. The Austenite start (A_s) and Austenite finish (A_f) temperatures identify the reverse martensite transformation temperature during on heating.

Table 11 Transformation temperatures for NiTi-SMA from DSC measurement.

Austenitic transformation temperatures	Martensitic transformation temperatures
A_s = 87.7 ˚C	M_s = 76.1 ˚C
A_f = 109.5 ˚C	M_f = 50.1 ˚C

The mechanical properties of NiTi SMA were evaluated by using uniaxial tensile test in air. A flat sample was cut by using electrical discharge machining (EDM) according to ASTM-E8/E8M-08[121]. The uniaxial tensile test was carried out with a loading rate of 0.2 mm/min at room temperature in a servo-hydraulic MTS test frame equipped with a 100 KN max load cell.

The DSC results for the transformation temperatures ensure that the material is fully martensite at room temperature and in twinned martensitic state at zero load. Figure shows the mechanical properties of the studied SMA. The inelastic deformation of the martensitic NiTi SMA begins at 200 MPa leading to the stress plateau region. Liu et al suggested that the inelastic deformation of martensite twins started at the very early stage of deformation[122].

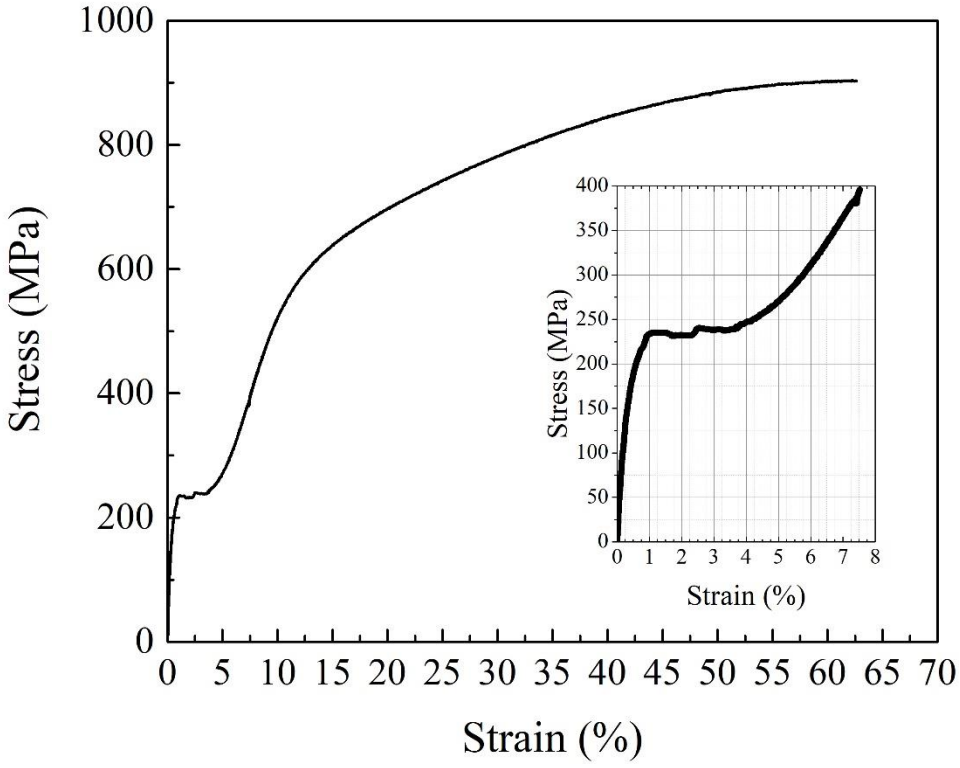

Figure 4.1 Stress-strain curve of NiTi sample with initial state of martensite phase.

The phase transformation characteristics of the NiTi SMA was obtained by isobaric experiments. The dog-bone sample was loaded under uniaxial tension. Prior thermal cycling, the dog-bone sample was loaded under uniaxial tension to various load levels. Figure 4.3 shows the results of thermal actuation. Figure 4.2 shows the isobaric tensile setup for thermal actuation includes the data acquisition instrument and furnace.

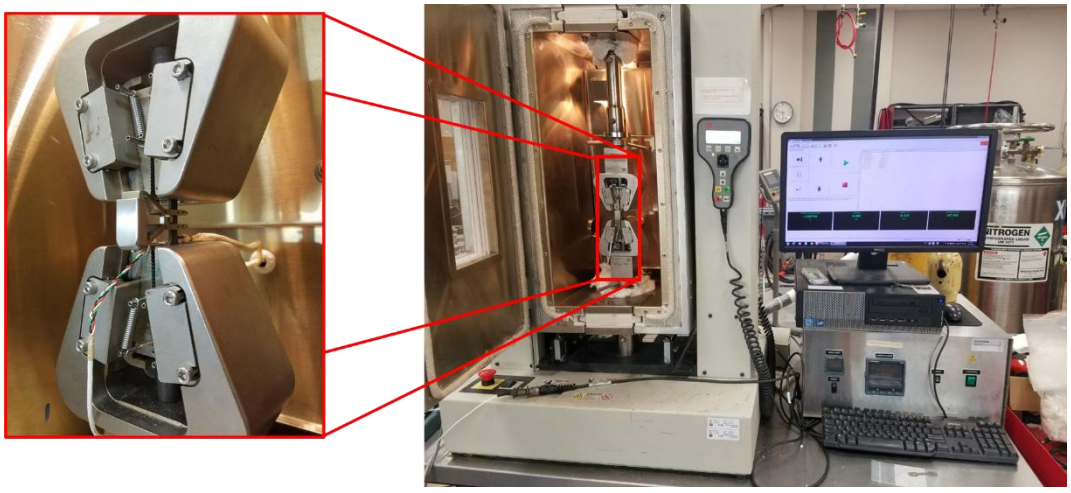

Figure 4.2 Experimental setup for thermal actuation under isobaric tensile test.

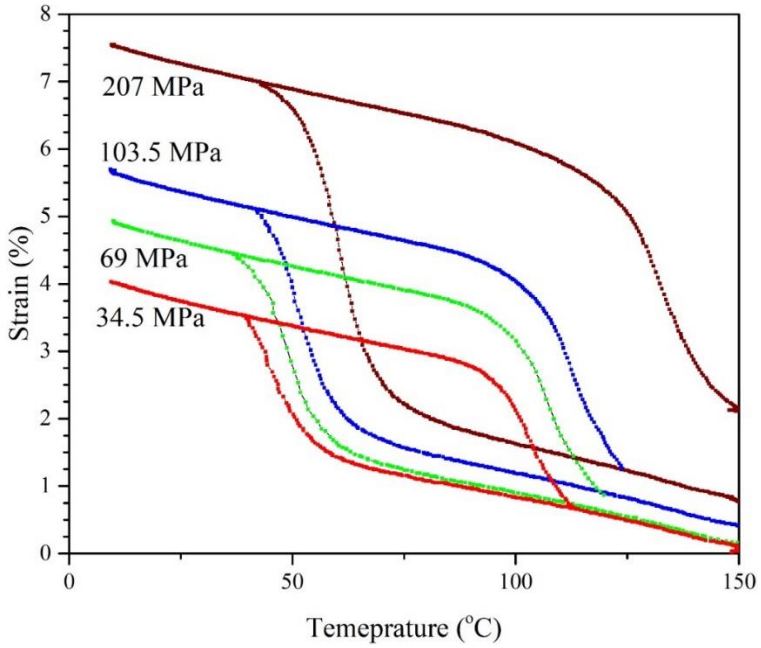

Figure 4.3 Strain-temperature response of NiTi under isobaric tensile experiment at various applied stress level.

Figure 4.4 shows a schematic of an actuation load and determined different strain during thermal cycling and the method to determine the phase transformation characteristics of NiTi SMA.

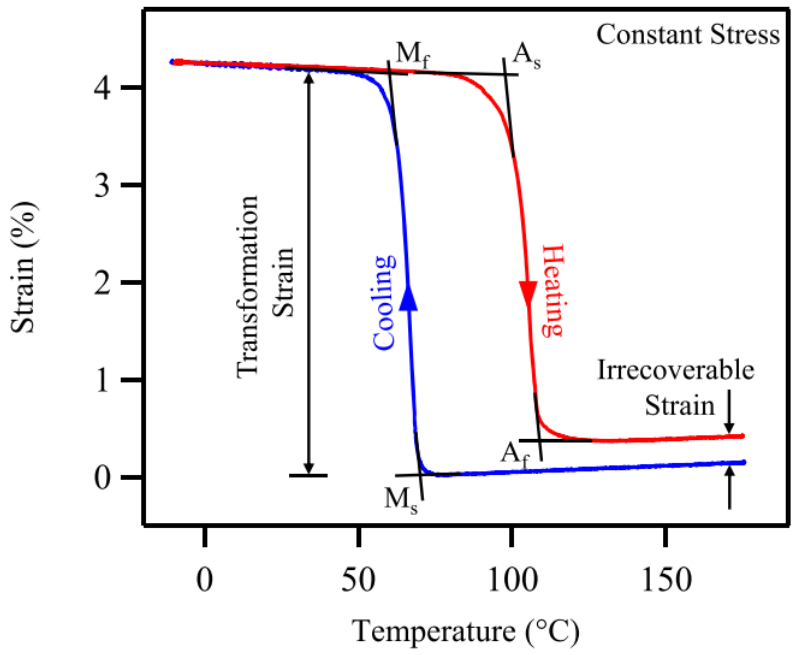

Figure 4.4 A schematic indicates the corresponding strain vs. temperature response of NiTi SMA during thermal actuation and exhibit irrecoverable strain and transformation strain. The tangent lines are used to measure the critical transformation temperatures (from figure 1 of [113], ©2019 reprinted by permission of IOP Publishing Ltd, DOI: 10.1117/12.508207).

4.2.2 Experimental methodology

Electrochemical testing was performed to characterize the changes of the surface layer during thermomechanical actuation and to investigate the interaction between thermos-mechanical loading and surface effects. The corrosion-thermomechanical actuation test was performed using CORTEST make CERT tensile testing machine in a modified Ringer's solution with the composition of 9.0 $g.l^{-1}$ NaCl, 0.42 $g.l^{-1}$ KCl, 0.24 $g.l^{-1}$ $CaCl_2$,and 0.2 $g.l^{-1}$NaHCO[28]. The Ringer's solution was used to stimulate the body fluids. The gauge length portion of the samples was polished up to 500 grit SiC paper on all the sides to remove the oxidation products from sample cutting step. Sample was heated up on the hot plate up to 130ºC and then cooled down to room temperature in air to have a fully twinned martensite at room temperature. An autoclave was pressurized at the beginning of experiment, prior to thermal cycling starting.

The electrochemical cell used includes a conventional three electrode configuration with a tungsten rod as the reference electrode, autoclave's body as a counter electrode, and NiTi SMA as a working electrode (Figure 4.5). The OCP was measured with respect to time prior each loading Measurements were performed with a Gamry Instrument Potentiostat/Galvanostat (600+). The OCP was continuously measured at each load level until stable potential values were achieved before starting the thermal cycling. Electrochemical Impedance Spectroscopy (EIS) measurements were carried out at the open circuit potential with an amplitude of 10 mV in the frequency range 10 kHz to 30 mHz at lowest and highest temperature during each cycle.

Figure 4.5 Experimental setup for thermal actuation in corrosive environment. A heating jacket was used to heat the corrosive media.

4.3 Results and Discussion

Figure 4.6 Show the results for the polarization resistance measurement at the beginning and after each cycle. The highest temperature for all cycle is at 100˚C and lowest temperature is 20˚C. At each individual cycle, the values for polarization resistance are higher at the beginning of the cycle (LT) compare to highest temperature that material was experiencing (HT). The values for the first cycle at 103 MPa are close to zero which can interpret as active dissolution of the metal oxide layer.

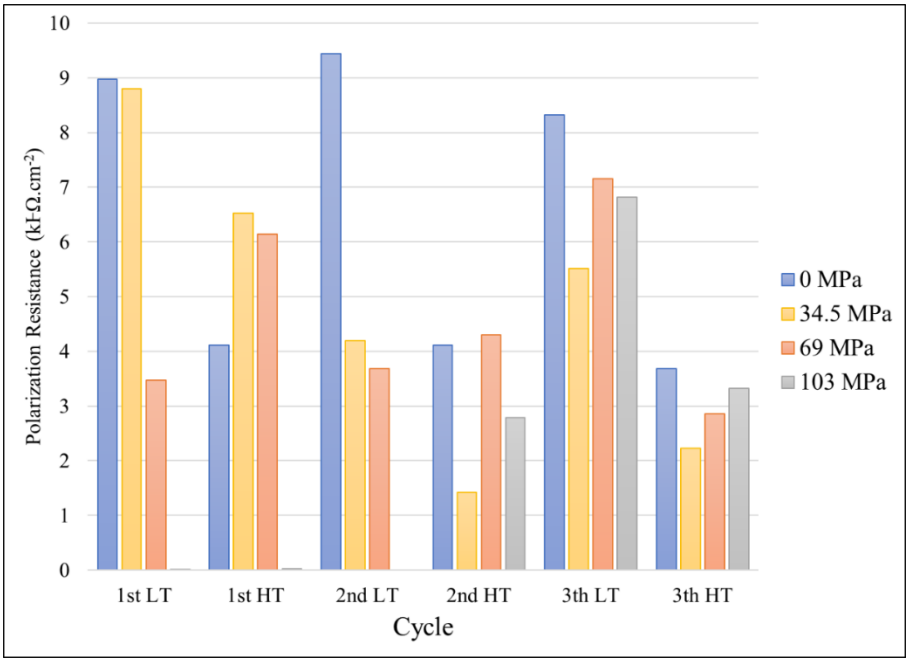

Figure 4.6 Polarization resistance measurement for the NiTi SMA sample at the beginning and end of each cycle. LT: lowest temperature (RT) and HT: highest temperature.

Figure 4.9-A shows the Nyquist plot of impedance spectra at the open circuit potential for the sample tested in modified Ringer's solution during different thermal actuation cycles. Two depressed capacitive semicircles can be seen for the Nyquist plot. The Nyquist plot indicates that increasing temperature during thermal actuations caused decrease in the diameter of the semicircles. From Figure 4.9-B, it can be seen the bode plot values at higher frequency decrease with increasing temperature. This decreasing is a consequence of increasing the solubility of the corrosion product film on the surface of sample and an increase in the conductivity of the solution between the working and reference electrodes with temperature. The bode plot values decrease considerably with temperature at lower frequencies indicates the increase of the NiTi corrosion rate at higher temperature[123]. The evolution of the phase angle with the frequency in Figure 4.9-C shows the presence of two time constants for the imposed signal during the first and second cycles. As can be seen in Figure 4.9-C, during the third cycle and after high temperature exposure, the third time constant appears in the phase angle spectra. Nigeuna investigated the effect of microstructure on the corrosion of Titanium alloy and shows the consequence of second phase on impedance spectra[124]. The presence of third capacitance can be related to the dissolution of passive layer formed from martensite phase in the passivated austenite phase.

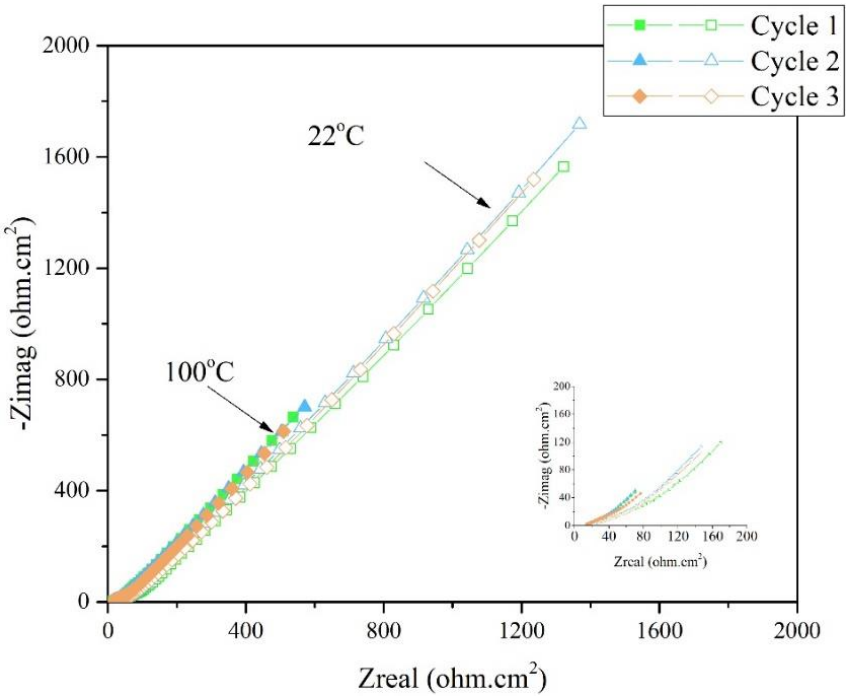

Figure 4.7 Nyquist plot of the NiTi sample in modified Ringer's solution during thermal actuation cycles under zero stress.

Figure 4.7 shows the Nyquist plot of impedance spectra at the open circuit potential for the sample tested in modified Ringer's solution during different thermal actuation cycles. Two depressed capacitive semicircles can be seen for the Nyquist plot. The Nyquist plot indicates that increasing temperature during thermal actuations caused decrease in the diameter of the semicircles.

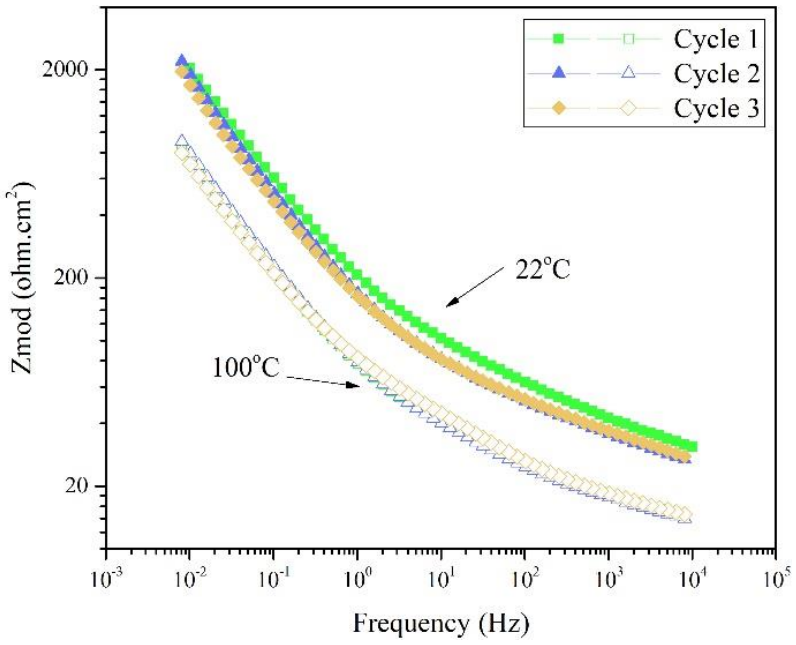

Figure 4.8 Bode plot of the NiTi sample in modified Ringer's solution during thermal actuation cycles under zero stress.

From Figure 4.8, it can be seen the bode plot values at higher frequency decrease with increasing temperature. This decreasing is a consequence of increasing the solubility of the corrosion product film on the surface of sample and an increase in the conductivity of the solution between the working and reference electrodes with temperature. The bode plot values decrease considerably with temperature at lower frequencies indicates the increase of the NiTi corrosion rate at higher temperature[123]. The evolution of the phase angle with the frequency in Figure 4.9 shows the presence of two time constants for the imposed signal during the first and second cycles. As can be seen in Figure 4.9, during the third cycle and after high temperature exposure, the third time constant appears in the phase angle spectra. Nigeuna investigated the effect of microstructure on the corrosion of

Titanium alloy and shows the consequence of second phase on impedance spectra[124]. The presence of third capacitance can be related to the dissolution of passive layer formed from martensite phase in the passivated austenite phase.

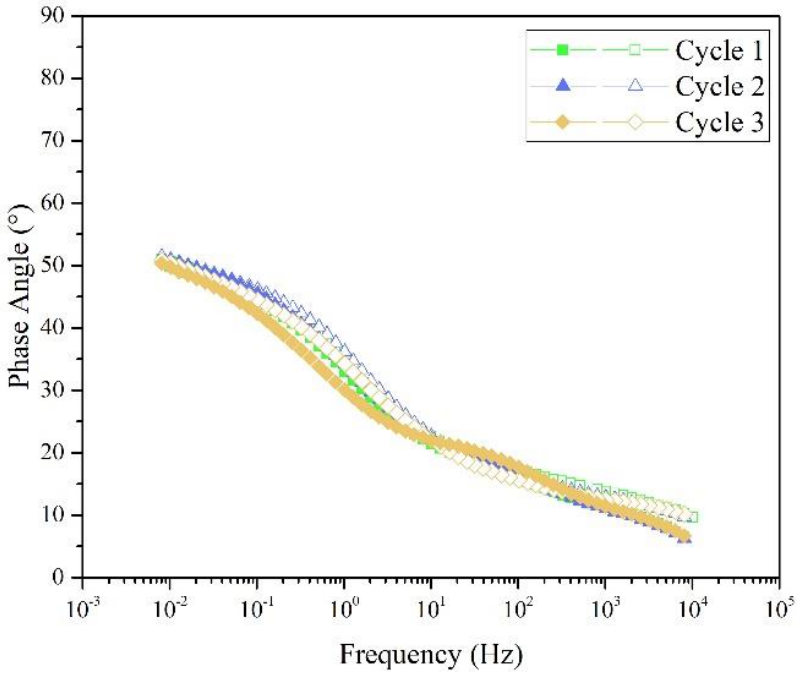

Figure 4.9 Phase angle plots of the NiTi sample in modified Ringer's solution during thermal actuation cycles under zero stress.

The EIS spectra obtained at the open circuit potential for the NiTi sample during different cycle of thermal actuation under 100MPa uniaxial stress can be seen in Figure 4.10 to Figure 4.12. EIS spectra at the beginning of the thermal actuation at room temperature (Figure 4.10) and for the second and third cycles (Figure 4.12) have two depressed semicircular shapes and have same pattern as thermal actuation at zero stress. The first

capacitive semicircle is related to the charge transfer process and at intermediate frequencies, the second capacitive semicircle is related to the corrosion product layer.

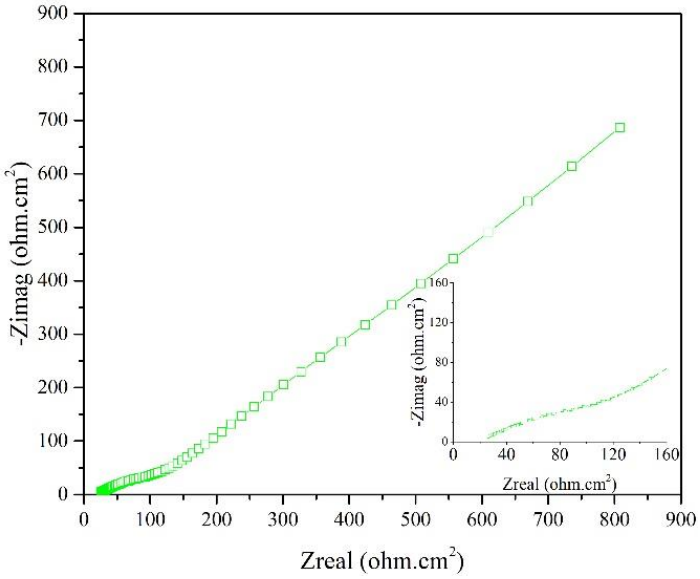

Figure 4.10 Nyquist plots of the NiTi sample in modified Ringer's solution during thermal actuation under 100MPa uniaxial stress at first cycle room temperature.

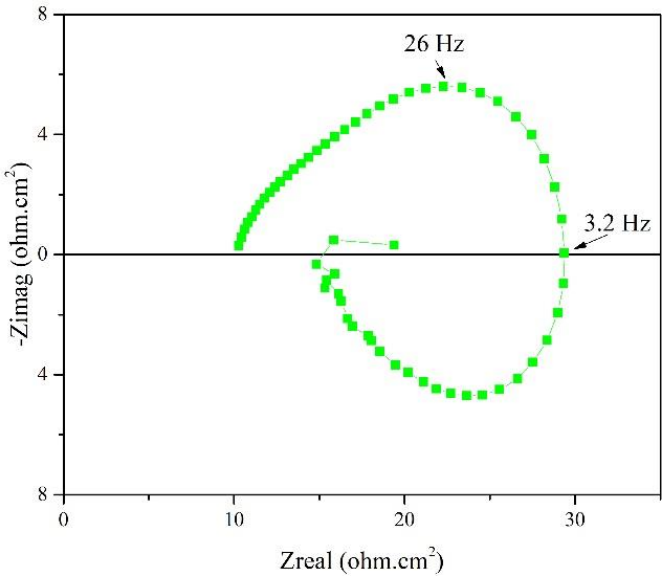

Figure 4.11 Nyquist plots of the NiTi sample in modified Ringer's solution during thermal actuation under 100MPa uniaxial stress at first cycle high temperature.

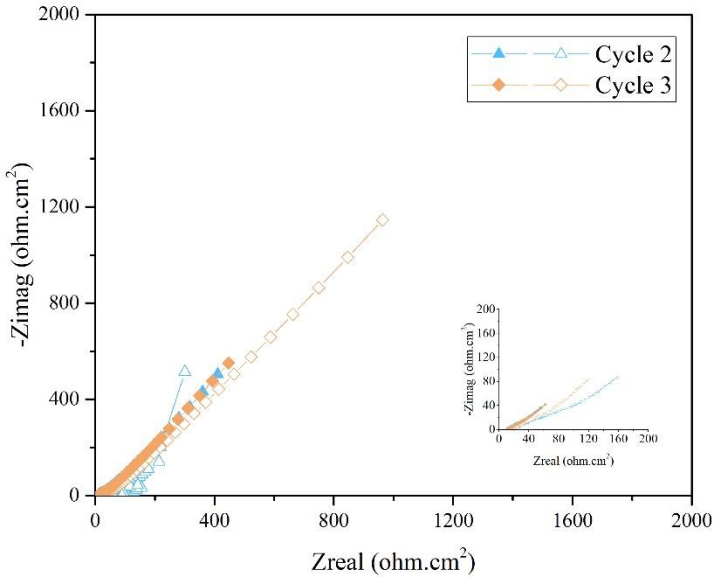

Figure 4.12 Nyquist plots of the NiTi sample in modified Ringer's solution during thermal actuation under 100MPa uniaxial stress at second and third cycles.

However, the Nyquist plot at 100˚C during first cycle (Figure 4.11) is characterized by two depressed capacitive semicircles from high to intermediate frequencies followed by an inductive arc at low frequency. The two general ideas exist about the inductive loop at lower frequencies in the chloride solution. First hypothesis, the formation of pits on the surface of oxide layer cause the appearance of the inducive loops[125]. The second hypothesis is the appearance of the inductive loop due to the adsorption of intermediate products on the surface. Figure shows the images from the surface of sample before thermal actuation and after the third cycle of thermal actuation in Ringer's solution at 100 MPa. Pits formed on the surface indicate the inductive loop at low frequencies results from the nucleation of pits.

5. SUMMARY AND FUTURE WORK

5.1 Conclusion and Summary

In chapter two, the corrosion resistance of NiTi SMA is deteriorated during loading and martensitic reorientation. The OCP remains constant during deformation in the elastic region. The EIS and SEM results indicate and show the presence of a passive layer. The passive layer breakdown is influenced by the loading, and since the repassivation is slower than the breakdown rate, it results in the activation of the surface over time. The higher cathodic slope in the elastic region suggests that the faster anodic reaction kinetics confirm the activation state. Inelastic strain during martensite reorientation significantly increases the mechanical-electrochemical effect, which can be detected by quick drops at the open circuit potential. The metal/solution interface shifts towards a more active condition in the detwinning process by a reduction in polarization resistance values. A quick drop at the OCP coincides with the plastic deformation of NiTi SMA. The change in the surface of the sample due to plastic deformation of detwinned martensite leads to a decrease in the slope of the LPR line. This change in the slope of the LPR line shows the higher possibility of local attack during martensite reorientation and in plastic deformation regions.

In chapter three, from the potentiodynamic polarization data, it was concluded that the tendency to localized corrosion may be related to the presence of different ratio of martensite and austenite phases. This tendency to localized corrosion causes by presence of higher cathodic sites and less anodic sites.

EIS and poteniodynamic polarization results with Microcapillary system indicate that the martensite phase is more corrosion resistant than austenite phase. Martensite phase

can act a cathodic side and promotes galvanic corrosion and increasing the corrosion rate of NiTi alloy during forward martensite transformation.

In chapter four of this dissertation, the results of the thermal actuation of NiTi-SMA in presence of corrosive environment show an active dissolution of protective metal oxide layer on the surface. The polarization resistance measurement and EIS results during thermal cycling indicate that thermal cycling leads to formation of new passive layer on the surface which can tolerate potential surface changes during phase transformation.

5.2 Recommended Future Research

Since, in the preliminary testing reported in this study, SMA appeared to show different corrosion behavior during phase transformation, and experience different protective oxide layer forming on the surface of the material at different temperatures.

This research proved the change on the thickness of passive oxide layer due to mechanical loads and change the metal underneath of the oxide layer. It is recommended to study the change on the properties of oxide layer during mechanical loading with different technique such as Mott-Schottky. Aside from evaluating SMA's corrosion performance, this research also exposed some problems associated with corrosion experiments and led to suggestions for future testing. The most obvious lesson learned from this research is that a high cycle corrosion-fatigue test needed for more accurate investigation of the degradation of SMA. An unstable surface during thermal actuation lead to a difficulty for corrosion measurements. Study the OCP values of the twinned martensite SMA and comparison with detwinned martensite under zero loading can lead to better understanding of crystallographic reorientation effect on corrosion behavior of

NiTi SMA. This study provides a strong understanding of the SMA phases and their relationship to corrosion behavior and corrosion-fatigue life, it would be ideal to implement a theoretical model that include SMA phases under different loading and corrosion rate of each phases using finite elemental analysis.

REFERENCES

[1] D. Hartl, D. Lagoudas, F. Calkins, J. Mabe, Use of a Ni60Ti shape memory alloy for active jet engine chevron application: I. Thermomechanical characterization, Smart Materials and Structures 19(1) (2009) 015020.

[2] D.C. Lagoudas, Shape memory alloys: modeling and engineering applications, Springer2008.

[3] J. Mohd Jani, M. Leary, A. Subic, M.A. Gibson, A review of shape memory alloy research, applications and opportunities, Materials & Design (1980-2015) 56 (2014) 1078-1113.

[4] C.S. Loh, H. Yokoi, T. Arai, New shape memory alloy actuator: design and application in the prosthetic hand, 2005 IEEE Engineering in Medicine and Biology 27th Annual Conference, IEEE, 2006, pp. 6900-6903.

[5] T. Waitz, T. Antretter, F. Fischer, H. Karnthaler, Size effects on martensitic phase transformations in nanocrystalline NiTi shape memory alloys, Materials Science and Technology 24(8) (2008) 934-940.

[6] N.M. Grande, G. Plotino, E. Silla, E. Pedulla, G. DeDeus, G. Gambarini, F. Somma, Environmental Temperature Drastically Affects Flexural Fatigue Resistance of Nickel-titanium Rotary Files, J Endod 43(7) (2017) 1157-1160.

[7] N. Schiff, B. Grosgogeat, M. Lissac, F. Dalard, Influence of fluoride content and pH on the corrosion resistance of titanium and its alloys, Biomaterials 23(9) (2002) 1995-2002.

[8] X. Li, J. Wang, E.-h. Han, W. Ke, Influence of fluoride and chloride on corrosion behavior of NiTi orthodontic wires, Acta Biomaterialia 3(5) (2007) 807-815.

[9] C. Trépanier, A.R. Pelton, Effect of temperature and pH on the corrosion resistance of Nitinol, International Conference on Shape Memory and Superelastic Technology (SMST), Baden-Baden, Germany, Oct, Citeseer, 2004, pp. 3-7.

[10] S.M. Toker, G. Gerstein, H.J. Maier, D. Canadinc, Effects of microstructural mechanisms on the localized oxidation behavior of NiTi shape memory alloys in simulated body fluid, Journal of Materials Science 53(2) (2017) 948-958.

[11] G.R. Mirshekari, a. Kermanpur, a. Saatchi, S.K. Sadrnezhaad, a.P. Soleymani, Microstructure, Cyclic Deformation and Corrosion Behavior of Laser Welded NiTi Shape Memory Wires, Journal of Materials Engineering and Performance 24(9) (2015) 3356-3364.

[12] M. Es-Souni, M. Es-Souni, H. Fischer-Brandies, On the properties of two binary NiTi shape memory alloys. Effects of surface finish on the corrosion behaviour and in vitro biocompatibility, Biomaterials 23(14) (2002) 2887-2894.

[13] L. Neelakantan, B. Monchev, M. Frotscher, G. Eggeler, The influence of secondary phase carbide particles on the passivity behaviour of NiTi shape memory alloys, Materials and Corrosion 63(11) (2012) 979-984.

[14] L. Tan, R. Dodd, W. Crone, Corrosion and wear-corrosion behavior of NiTi modified by plasma source ion implantation, Biomaterials 24(22) (2003) 3931-3939.

[15] T. Hu, C. Chu, Y. Xin, S. Wu, K.W.K. Yeung, P.K. Chu, Corrosion products and mechanism on NiTi shape memory alloy in physiological environment, Journal of Materials Research 25(2) (2011) 350-358.

[16] Y. Shen, W. Qian, H. Abtin, Y. Gao, M. Haapasalo, Effect of environment on fatigue failure of controlled memory wire nickel-titanium rotary instruments, Journal of endodontics 38(3) (2012) 376-380.

[17] Y. Shen, W. Qian, H. Abtin, Y. Gao, M. Haapasalo, Fatigue testing of controlled memory wire nickel-titanium rotary instruments, Journal of endodontics 37(7) (2011) 997-1001.

[18] G.S. Cheung, B.W. Darvell, Low-cycle fatigue of rotary NiTi endodontic instruments in hypochlorite solution, dental materials 24(6) (2008) 753-759.

[19] G.S. Cheung, Y. Shen, B.W. Darvell, Effect of environment on low-cycle fatigue of a nickel–titanium instrument, Journal of endodontics 33(12) (2007) 1433-1437.

[20] O.W. Bertacchini, D.C. Lagoudas, E. Patoor, Thermomechanical transformation fatigue of TiNiCu SMA actuators under a corrosive environment – Part I: Experimental results, International Journal of Fatigue 31(10) (2009) 1571-1578.

[21] O.W. Bertacchini, D.C. Lagoudas, E. Patoor, Fatigue life characterization of shape memory alloys undergoing thermomechanical cyclic loading, SPIE2003.

[22] D.C. Lagoudas, O.W. Bertacchini, D.C. Lagoudas, E. Patoor, Fatigue life characterization of shape memory alloys undergoing thermomechanical cyclic loading, 5053 (2003) 612.

[23] J. Racek, P. Šittner, L. Heller, J. Pilch, P. Sedlák, L. Kadeřávek, Electrochemistry of NiTi Wires/Springs Subjected to Static/Cyclic Loadings, Materials Today: Proceedings 2 (2015) S965-S969.

[24] J. Racek, P. Šittner, L. Heller, J. Pilch, M. Petrenec, P. Sedlák, Corrosion of NiTi wires with cracked oxide layer, Journal of Materials Engineering and Performance 23(7) (2014) 2659-2668.

[25] L. Petrini, F. Migliavacca, Biomedical Applications of Shape Memory Alloys, Journal of Metallurgy 2011 (2011).

[26] M.H. Elahinia, M. Hashemi, M. Tabesh, S.B. Bhaduri, Manufacturing and processing of NiTi implants: A review, Progress in materials science 57(5) (2012) 911-946.

[27] B. Haghgouyan, N. Shafaghi, C.C. Aydıner, G. Anlas, Experimental and computational investigation of the effect of phase transformation on fracture parameters of an SMA, Smart Materials and Structures 25(7) (2016) 075010.

[28] B. Haghgouyan, S. Jape, C. Hayrettin, T. Baxevanis, I. Karaman, D.C. Lagoudas, Experimental and numerical investigation of the stable crack growth regime under pseudoelastic loading in shape memory alloys, SPIE2018.

[29] C. Heintz, G. Riepe, L. Birken, E. Kaiser, N. Chakfé, M. Morlock, G. Delling, H. Imig, Corroded Nitinol Wires in Explanted Aortic Endografts: An Important Mechanism of Failure?, Journal of Endovascular Therapy 8(3) (2001) 248-253.

[30] D.a. Miller, D.C. Lagoudas, Thermomechanical characterization of NiTiCu and NiTi SMA actuators: Influence of plastic strains, Smart Materials and Structures 9(5) (2000) 640-652.

[31] E. Blasco-Tamarit, a. Igual-Muñoz, J.G. Antón, D. García-García, Comparison between open circuit and imposed potential measurements to evaluate the effect of temperature on galvanic corrosion of the pair alloy 31-welded alloy 31 in LiBr solutions, Corrosion Science 50(12) (2008) 3590-3598.

[32] A.N. Bucsek, D.C. Pagan, L. Casalena, Y. Chumlyakov, M.J. Mills, A.P. Stebner, Ferroelastic twin reorientation mechanisms in shape memory alloys elucidated with 3D X-ray microscopy, Journal of the Mechanics and Physics of Solids 124 (2019) 897-928.

[33] A. Stebner, S. Vogel, R. Noebe, T. Sisneros, B. Clausen, D. Brown, A. Garg, L. Brinson, Micromechanical quantification of elastic, twinning, and slip strain partitioning exhibited by polycrystalline, monoclinic nickel–titanium during large uniaxial deformations measured via in-situ neutron diffraction, Journal of the Mechanics and Physics of Solids 61(11) (2013) 2302-2330.

[34] P.K. Kumar, D.C. Lagoudas, Experimental and microstructural characterization of simultaneous creep, plasticity and phase transformation in Ti50Pd40Ni10 high-temperature shape memory alloy, Acta Materialia 58(5) (2010) 1618-1628.

[35] S. Manchiraju, P.M. Anderson, Coupling between martensitic phase transformations and plasticity: A microstructure-based finite element model, International Journal of Plasticity 26(10) (2010) 1508-1526.

[36] C. Yu, G. Kang, Q. Kan, Crystal plasticity based constitutive model of NiTi shape memory alloy considering different mechanisms of inelastic deformation, International Journal of Plasticity 54 (2014) 132-162.

[37] Y.S. Jiménez, M.T. Gil, M.T. Guerra, L. Baltes, J.M. Rosca, Interpretation of open circuit potential of two titanium alloys for a long time immersion in physiological fluid, Bulletin of the Transilvania University of Braşov• Vol 2 (2009) 51.

[38] D.V. Ribeiro, J.C.C. Abrantes, Application of electrochemical impedance spectroscopy (EIS) to monitor the corrosion of reinforced concrete: A new approach, Construction and Building Materials 111 (2016) 98-104.

[39] I.B. Obot, I.B. Onyeachu, Electrochemical frequency modulation (EFM) technique: Theory and recent practical applications in corrosion research, Journal of Molecular Liquids 249 (2018) 83-96.

[40] S.S. Abdel-Rehim, K.F. Khaled, N.S. Abd-Elshafi, Electrochemical frequency modulation as a new technique for monitoring corrosion inhibition of iron in acid media by new thiourea derivative, Electrochimica Acta 51(16) (2006) 3269-3277.

[41] B. Haghgouyan, C. Hayrettin, T. Baxevanis, I. Karaman, D.C. Lagoudas, Fracture toughness of NiTi–Towards establishing standard test methods for phase transforming materials, Acta Materialia 162 (2019) 226-238.

[42] A.C. Tas, The use of physiological solutions or media in calcium phosphate synthesis and processing, Acta biomaterialia 10(5) (2014) 1771-1792.

[43] E. Gutman, G. Solovioff, D. Eliezer, The mechanochemical behavior of type 316L stainless steel, Corrosion science 38(7) (1996) 1141-1145.

[44] T. Wu, M. Yan, J. Xu, Y. Liu, C. Sun, W. Ke, Mechano-chemical effect of pipeline steel in microbiological corrosion, Corrosion Science 108 (2016) 160-168.

[45] L. Jinlong, L. Hongyun, Effect of Temperature and Chloride Ion Concentration on Corrosion of Passive Films on Nano/Ultrafine Grained Stainless Steels, Journal of Materials Engineering and Performance 23(12) (2014) 4223-4229.

[46] V. Vignal, R. Oltra, M. Verneau, L. Coudreuse, Influence of an elastic stress on the conductivity of passive films, Materials Science and Engineering: A 303(1) (2001) 173-178.

[47] K. Darowicki, J. Orlikowski, A. Arutunow, Dynamic electrochemical impedance spectroscopy measurements of passive layer cracking under static tensile stresses, Journal of Solid State Electrochemistry 8(6) (2004) 352-359.

[48] K. Darowicki, J. Orlikowski, A. Arutunow, W. Jurczak, The effect of tensile stresses on aluminium passive layer durability, Electrochimica Acta 51(27) (2006) 6091-6096.

[49] Z. Cui, H. Man, X. Yang, The corrosion and nickel release behavior of laser surface-melted NiTi shape memory alloy in Hanks' solution, Surface and Coatings Technology 192(2-3) (2005) 347-353.

[50] B. Thierry, M. Tabrizian, C. Trepanier, O. Savadogo, L.H. Yahia, Effect of surface treatment and sterilization processes on the corrosion behavior of NiTi shape memory alloy, Journal of Biomedical Materials Research 51(4) (2000) 685-693.

[51] S.L.d. Assis, S. Wolynec, I. Costa, Corrosion characterization of titanium alloys by electrochemical techniques, Electrochimica Acta 51(8-9) (2006) 1815-1819.

[52] J.E.G. González, J.C. Mirza-Rosca, Study of the corrosion behavior of titanium and some of its alloys for biomedical and dental implant applications, Journal of Electroanalytical Chemistry 471(2) (1999) 109-115.

[53] W. Simka, M. Kaczmarek, A. Baron-Wiecheć, G. Nawrat, J. Marciniak, J. Żak, Electropolishing and passivation of NiTi shape memory alloy, Electrochimica Acta 55(7) (2010) 2437-2441.

[54] K.M. Kim, J.T. Yeom, H.-S. Lee, S.-Y. Yoon, J.H. Kim, High temperature oxidation behavior of Ti–Ni–Hf shape memory alloy, Thermochimica acta 583 (2014) 1-7.

[55] M. Carl, B. Van Doren, M.L. Young, In situ synchrotron radiation X-ray diffraction study on phase and oxide growth during a high temperature cycle of a NiTi-20 at.% Zr high temperature shape memory alloy, Shape Memory and Superelasticity 4(1) (2018) 174-185.

[56] M.M. Verdian, K. Raeissi, M. Salehi, Corrosion performance of HVOF and APS thermally sprayed NiTi intermetallic coatings in 3.5% NaCl solution, Corrosion Science 52(3) (2010) 1052-1059.

[57] S. Zhang, X. Pang, Y. Wang, K. Gao, Corrosion behavior of steel with different microstructures under various elastic loading conditions, Corrosion Science 75 (2013) 293-299.

[58] B. Hirschorn, M.E. Orazem, B. Tribollet, V. Vivier, I. Frateur, M. Musiani, Determination of effective capacitance and film thickness from constant-phase-element parameters, Electrochimica Acta 55(21) (2010) 6218-6227.

[59] K. Li, X. Huang, Z. Zhao, Y. Li, Y.Q. Fu, Electrochemical and corrosion behaviors of sputtered TiNi shape memory films, Smart Materials and Structures 25(3) (2016) 035039.

[60] M. Mohajeri, H. Castaneda-Lopez, B. Haghgouyan, D.C. Lagoudas, Nickel Titanium Alloy Failure Analysis Under Thermal Cycling and Mechanical Loading: A Preliminary Study, CORROSION 2018, NACE International, 2018.

[61] M. Mohajeri, H. Castaneda, D. Lagoudas, Corrosion monitoring of NiTi alloy with small-amplitude potential intermodulation technique, Behavior and Mechanics of Multifunctional Materials and Composites XII, International Society for Optics and Photonics, 2018, p. 1059616.

[62] X. Zheng, H. Castaneda, H. Gao, A. Srivastava, Synergistic effects of corrosion and slow strain rate loading on the mechanical and electrochemical response of an aluminium alloy, Corrosion Science (2019).

[63] S.K. Jindal, S.K. Raghuwanshi, Study of materials for the design of MEMS capacitive pressure sensor, AIP Conference Proceedings, AIP Publishing, 2016, p. 020118.

[64] R.W. Wheeler, O. Benafan, X. Gao, F.T. Calkins, Z. Ghanbari, G. Hommer, D. Lagoudas, A. Petersen, J.M. Pless, A.P. Stebner, Engineering design tools for shape memory alloy actuators: CASMART collaborative best practices and case studies, ASME 2016 Conference on Smart Materials, Adaptive Structures and Intelligent Systems, American Society of Mechanical Engineers Digital Collection, 2016.

[65] T. Baxevanis, A. Parrinello, D. Lagoudas, On the fracture toughness enhancement due to stress-induced phase transformation in shape memory alloys, International Journal of Plasticity 50 (2013) 158-169.

[66] M. Tabesh, B. Liu, J. Boyd, D. Lagoudas, Analytical solution for the pseudoelastic response of a shape memory alloy thick-walled cylinder under internal pressure, Smart Materials and Structures 22(9) (2013) 094007.

[67] S.R. Cornell, D.J. Hartl, D.C. Lagoudas, Experimental Validation of a Shape Memory Alloy Constitutive Model by Heterogeneous Thermal Loading Using Infrared Thermography and Digital Image Correlation, ASME 2013 Conference on Smart Materials, Adaptive Structures and Intelligent Systems, American Society of Mechanical Engineers Digital Collection, 2013.

[68] R.W. Wheeler, D.J. Hartl, Y. Chemisky, D.C. Lagoudas, Characterization And Modeling Of Thermo-Mechanical Fatigue In Equiatomic Niti Actuators, ASME 2014 Conference on Smart Materials, Adaptive Structures and Intelligent Systems, American Society of Mechanical Engineers Digital Collection, 2014.

[69] T. Baxevanis, A. Cox, D. Lagoudas, Micromechanics of precipitated near-equiatomic Ni-rich NiTi shape memory alloys, Acta Mechanica 225(4-5) (2014) 1167-1185.

[70] B. Dhakal, D. Nicholson, A. Saleeb, S. Padula II, R. Vaidyanathan, Three-dimensional deformation response of a NiTi shape memory helical-coil actuator during thermomechanical cycling: experimentally validated numerical model, Smart Materials and Structures 25(9) (2016) 095056.

[71] Q. Kan, G. Kang, Constitutive model for uniaxial transformation ratchetting of super-elastic NiTi shape memory alloy at room temperature, International Journal of Plasticity 26(3) (2010) 441-465.

[72] J.G. Boyd, D.C. Lagoudas, A thermodynamical constitutive model for shape memory materials. Part I. The monolithic shape memory alloy, International Journal of Plasticity 12(6) (1996) 805-842.

[73] D.C. Lagoudas, Z. Bo, M.A. Qidwai, A unified thermodynamic constitutive model for SMA and finite element analysis of active metal matrix composites, Mechanics of composite materials and structures 3(2) (1996) 153-179.

[74] R. Mehrabi, M. Kadkhodaei, M. Elahinia, Constitutive modeling of tension-torsion coupling and tension-compression asymmetry in NiTi shape memory alloys, Smart Materials and Structures 23(7) (2014) 075021.

[75] J.M. Jani, M. Leary, A. Subic, Fatigue of NiTi SMA–pulley system using Taguchi and ANOVA, Smart Materials and Structures 25(5) (2016) 057001.

[76] T. Baxevanis, A. Cox, D.C. Lagoudas, Micromechanics of precipitated near-equiatomic Ni-rich NiTi shape memory alloys, Acta Mechanica 225(4-5) (2014) 1167-1185.

[77] T. Kanemura, K.i. Yokoyama, J.i. Sakai, Effects of acid type on corrosion and fracture behavior of Ni–Ti superelastic alloy under sustained tensile load in physiological saline solution containing hydrogen peroxide, Corrosion Science 50(10) (2008) 2785-2795.

[78] K.i. Yokoyama, T. Ogawa, A. Fujita, K. Asaoka, J.i. Sakai, Fracture of Ni-Ti superelastic alloy under sustained tensile load in physiological saline solution containing hydrogen peroxide, Journal of Biomedical Materials Research Part A: An Official Journal of The Society for Biomaterials, The Japanese Society for Biomaterials, and The Australian Society for Biomaterials and the Korean Society for Biomaterials 82(3) (2007) 558-567.

[79] D. Hartl, D. Lagoudas, Thermomechanical characterization of shape memory alloy materials, Shape memory alloys, Springer2008, pp. 53-119.

[80] J.K. Allafi, X. Ren, G. Eggeler, The mechanism of multistage martensitic transformations in aged Ni-rich NiTi shape memory alloys, Acta Materialia 50(4) (2002) 793-803.

[81] N. Sato, A theory for breakdown of anodic oxide films on metals, Electrochimica Acta 16(10) (1971) 1683-1692.

[82] X. Zhang, Z.H. Jiang, Z.P. Yao, Y. Song, Z.D. Wu, Effects of scan rate on the potentiodynamic polarization curve obtained to determine the Tafel slopes and corrosion current density, Corrosion Science 51(3) (2009) 581-587.

[83] S. Tamilselvi, V. Raman, N. Rajendran, Corrosion behaviour of Ti–6Al–7Nb and Ti–6Al–4V ELI alloys in the simulated body fluid solution by electrochemical impedance spectroscopy, Electrochimica Acta 52(3) (2006) 839-846.

[84] R. Baboian, Corrosion tests and standards: application and interpretation, ASTM international1995.

[85] M. Ergun, A.Y. Turan, Pitting potential and protection potential of carbon steel for chloride ion and the effectiveness of different inhibiting anions, Corrosion science 32(10) (1991) 1137-1142.
[86] B. Lindholm-Sethson, B. Ardlin, Effects of pH and fluoride concentration on the corrosion of titanium, Journal of Biomedical Materials Research Part A: An Official Journal of The Society for Biomaterials, The Japanese Society for Biomaterials, and The Australian Society for Biomaterials and the Korean Society for Biomaterials 86(1) (2008) 149-159.
[87] I. Gurappa, Characterization of different materials for corrosion resistance under simulated body fluid conditions, Materials Characterization 49(1) (2002) 73-79.
[88] L. Hamadou, L. Aïnouche, A. Kadri, S.A.A. Yahia, N. Benbrahim, Electrochemical impedance spectroscopy study of thermally grown oxides exhibiting constant phase element behaviour, Electrochimica Acta 113 (2013) 99-108.
[89] P. Sun, F. Li, C. Yang, T. Sun, I. Kady, B. Hunt, J. Zhuang, Formation of a single gold nanoparticle on a nanometer-sized electrode and its electrochemical behaviors, The Journal of Physical Chemistry C 117(12) (2013) 6120-6125.
[90] R.M. Souto, M.a.M. Laz, R.L. Reis, Degradation characteristics of hydroxyapatite coatings on orthopaedic TiAlV in simulated physiological media investigated by electrochemical impedance spectroscopy, Biomaterials 24(23) (2003) 4213-4221.
[91] S. Tamilselvi, R. Murugaraj, N. Rajendran, Electrochemical impedance spectroscopic studies of titanium and its alloys in saline medium, Materials and Corrosion 58(2) (2007) 113-120.

[92] M. Aziz-Kerrzo, K.G. Conroy, A.M. Fenelon, S.T. Farrell, C.B. Breslin, Electrochemical studies on the stability and corrosion resistance of titanium-based implant materials, Biomaterials 22(12) (2001) 1531-1539.

[93] J. Pan, D. Thierry, C. Leygraf, Electrochemical impedance spectroscopy study of the passive oxide film on titanium for implant application, Electrochimica Acta 41(7-8) (1996) 1143-1153.

[94] D. Vojtěch, M. Voděrová, J. Fojt, P. Novák, T. Kubásek, Surface structure and corrosion resistance of short-time heat-treated NiTi shape memory alloy, Applied Surface Science 257(5) (2010) 1573-1582.

[95] J. Gonzalez, J. Mirza-Rosca, Study of the corrosion behavior of titanium and some of its alloys for biomedical and dental implant applications, Journal of Electroanalytical Chemistry 471(2) (1999) 109-115.

[96] S. Kuyucak, S.-H. Chung, Temperature dependence of conductivity in electrolyte solutions and ionic channels of biological membranes, Biophysical chemistry 52(1) (1994) 15-24.

[97] V.F. Lvovich, Impedance spectroscopy: applications to electrochemical and dielectric phenomena, John Wiley & Sons2012.

[98] Y. Zhao, C. Jiang, Z. Xu, F. Cai, Z. Zhang, P. Fu, Microstructure and corrosion behavior of Ti nanoparticles reinforced Ni–Ti composite coatings by electrodeposition, Materials & Design 85 (2015) 39-46.

[99] L. Jinlong, L. Tongxiang, W. Chen, D. Limin, Surface corrosion enhancement of passive films on NiTi shape memory alloy in different solutions, Materials Science and Engineering: C 63 (2016) 192-197.

[100] M. Karthega, V. Raman, N. Rajendran, Influence of potential on the electrochemical behaviour of β titanium alloys in Hank's solution, Acta biomaterialia 3(6) (2007) 1019-1023.

[101] H. Cesiulis, N. Tsyntsaru, A. Ramanavicius, G. Ragoisha, The study of thin films by electrochemical impedance spectroscopy, Nanostructures and thin films for multifunctional applications, Springer2016, pp. 3-42.

[102] P. Zoltowski, On the electrical capacitance of interfaces exhibiting constant phase element behaviour, Journal of Electroanalytical Chemistry 443(1) (1998) 149-154.

[103] J.-B. Jorcin, M.E. Orazem, N. Pébère, B. Tribollet, CPE analysis by local electrochemical impedance spectroscopy, Electrochimica Acta 51(8-9) (2006) 1473-1479.

[104] P. Córdoba-Torres, T. Mesquita, R. Nogueira, Influence of geometry-induced current and potential distributions on the characterization of constant-phase element behavior, Electrochimica Acta 87 (2013) 676-685.

[105] M.E. Orazem, I. Frateur, B. Tribollet, V. Vivier, S. Marcelin, N. Pébère, A.L. Bunge, E.A. White, D.P. Riemer, M. Musiani, Dielectric properties of materials showing constant-phase-element (CPE) impedance response, Journal of The Electrochemical Society 160(6) (2013) C215-C225.

[106] P. Córdoba-Torres, T. Mesquita, R. Nogueira, Toward a better characterization of constant-phase element behavior on disk electrodes from direct impedance analysis: methodological considerations and mass transport effects, Electrochimica Acta 92 (2013) 323-334.

[107] M.E. Orazem, N. Pébère, B. Tribollet, Enhanced graphical representation of electrochemical impedance data, Journal of The Electrochemical Society 153(4) (2006) B129-B136.

[108] C. Hsu, F. Mansfeld, Concerning the conversion of the constant phase element parameter Y0 into a capacitance, Corrosion 57(9) (2001) 747-748.

[109] M. Stern, A.L. Geary, Electrochemical polarization I. A theoretical analysis of the shape of polarization curves, Journal of the electrochemical society 104(1) (1957) 56-63.

[110] J. Xu, L. Jiang, J. Wang, Influence of detection methods on chloride threshold value for the corrosion of steel reinforcement, Construction and Building Materials 23(5) (2009) 1902-1908.

[111] A.Y. Musa, A.A.H. Kadhum, A.B. Mohamad, A.R. Daud, M.S. Takriff, S.K. Kamarudin, A comparative study of the corrosion inhibition of mild steel in sulphuric acid by 4, 4-dimethyloxazolidine-2-thione, Corrosion Science 51(10) (2009) 2393-2399.

[112] D.C. Lagoudas, O.W. Bertacchini, E. Patoor, Surface crack development in transformation induced fatigue of SMA actuators, Residual Stress and Its Effects on Fatigue and Fracture, Springer2006, pp. 209-222.

[113] B. Haghgouyan, S. Jape, T. Baxevanis, I. Karaman, D.C. Lagoudas, Stable crack growth in NiTi shape memory alloys: 3D finite element modeling and experimental validation, Smart Materials and Structures 28(6) (2019) 064001.

[114] B. Haghgouyan, B. Young, I. Karaman, D. Lagoudas, Fracture toughness of martensitic NiTiHf high-temperature shape memory alloy, Behavior and Mechanics of Multifunctional Materials XIII, International Society for Optics and Photonics, 2019, p. 109680A.

[115] M.M. Hasan, T. Baxevanis, Actuation Fatigue Life Prediction of Notched Shape Memory Alloy Members, Journal of Applied Mechanics 86(6) (2019) 064501.

[116] L. Xu, A. Solomou, T. Baxevanis, D.C. Lagoudas, A three-dimensional constitutive modeling for shape memory alloys considering two-way shape memory effect and transformation-induced plasticity, AIAA Scitech 2019 Forum, 2019, p. 1195.

[117] L. Xu, T. Baxevanis, D. Lagoudas, A three-dimensional constitutive model for polycrystalline shape memory alloys under large strains combined with large rotations, ASME 2018 Conference on Smart Materials, Adaptive Structures and Intelligent Systems, American Society of Mechanical Engineers Digital Collection.

[118] O. Prymak, A. Klocke, B. Kahl-Nieke, M. Epple, Fatigue of orthodontic nickel–titanium (NiTi) wires in different fluids under constant mechanical stress, Materials Science and Engineering: A 378(1-2) (2004) 110-114.

[119] C.-W. Chan, A study on the corrosion fatigue behaviour of laser-welded shape memory NiTi wires in a simulated body fluid, Surface and Coatings Technology 320 (2017) 574-578.

[120] G. Cheung, B. Darvell, Fatigue testing of a NiTi rotary instrument. Part 1: strain–life relationship, International endodontic journal 40(8) (2007) 612-618.

[121] A. Standard, E8/E8M, Standard test methods for tension testing of metallic materials 3 (2011) 66.

[122] Y. Liu, Z. Xie, J.V. Humbeeck, L. Delaey, Y. Liu, On the deformation of the twinned domain in Niti shape memory alloys, Philosophical Magazine A 80(8) (2000) 1935-1953.

[123] H.H. Hassan, Inhibition of mild steel corrosion in hydrochloric acid solution by triazole derivatives, Electrochimica Acta 53(4) (2007) 1722-1730.

[124] T. Nishimura, Effect of Microstructure on the Electrochemical Behavior of Ti-10 Mass% Mn Alloys in High Chloride Solution, Journal of Materials Engineering and Performance 25(2) (2015) 443-450.

[125] M.A. Jingling, W. Jiuba, L.I. Gengxin, X.V. Chunhua, The corrosion behaviour of Al–Zn–In–Mg–Ti alloy in NaCl solution, Corrosion Science 52(2) (2010) 534-539.

APPENDIX A

Electrochemical Frequency Modulation

The over potential expression for a dual-frequency sinusoidal potential signal:

(4) $$\eta = U_0 \sin \omega_1 t + U_0 \sin \omega_2 t$$

The substitution Eq.(4) in Stern-Geary expression resulting in:

(5) $$i = i_{corr}[\exp(\frac{U_0 \sin \omega_1 t}{\beta_a}) \exp(\frac{U_0 \sin \omega_2 t}{\beta_a}) - \exp(\frac{U_0 \sin \omega_1 t}{\beta_c}) \exp \frac{U_0 \sin \omega_2 t}{\beta_c})$$

By using the Taylor series for exponential parts to the third order and invoking trigonometric relationships, the Eq.(5) yields the following form:

(6) $$\begin{aligned} i = {} & i_{fr} + i_{\omega_1} \sin \omega_1 t + i_{\omega_2} \sin \omega_2 t - i_{2\omega_1} \cos 2\omega_1 t - i_{2\omega_2} \cos 2\omega_2 t - i_{3\omega_1} \sin 3\omega_1 t - \\ & i_{3\omega_2} \sin 3\omega_2 t + i_{\omega_2 \pm \omega_1} \cos(\omega_2 t - \omega_1 t) - i_{\omega_2 \pm \omega 1} \cos(\omega_2 t + \omega_1 t) + i_{2\omega_2 \pm \omega_1} \sin(2\omega_2 t - \omega_1 t) - \\ & i_{2\omega_2 \pm \omega 1} \sin(2\omega_2 t + \omega_1 t) + i_{2\omega_1 \pm \omega 2} \sin(2\omega_1 t - \omega_2 t) - i_{2\omega_1 \pm \omega_2} \sin(2\omega_1 t + \omega_2 t) \end{aligned}$$

where i_{fr} is the Faraday rectification current at zero frequency. The harmonic and intermodulation currents in Eq.(6) are equal to:

(7) $$i_{\omega_1} = i_{\omega_2} = i_{corr}(\frac{U_0}{\beta_a} + \frac{U_0}{\beta_c})$$

(8) $$i_{2\omega_1} = i_{2\omega_2} = \frac{1}{4} i_{corr}[(\frac{U_0}{\beta_a})^2 - (\frac{U_0}{\beta_c})^2]$$

(9) $$i_{3\omega_1} = i_{3\omega_2} = \frac{1}{24} i_{corr}[(\frac{U_0}{\beta_a})^3 + (\frac{U_0}{\beta_c})^3]$$

(10) $$i_{\omega_1 \pm \omega_2} = \frac{1}{2} i_{corr}[(\frac{U_0}{\beta_a})^2 - (\frac{U_0}{\beta_c})^2]$$

(11) $$i_{2\omega_2\pm\omega_1} = i_{2\omega_1\pm\omega_2} = \frac{1}{24} i_{corr}[(\frac{U_0}{\beta_a})^3 + (\frac{U_0}{\beta_c})^3]$$

i_{corr}, β_a and β_c are obtained by solving Eq. (7) to (11) in the following form:

(12) $$i_{corr} = \frac{i^2_{\omega_1.\omega_2}}{2\sqrt{8 i_{\omega_1.\omega_2} i_{2\omega_2\pm\omega_1} - 3 i^2_{\omega_2\pm\omega_1}}}$$

(13) $$\beta_a = \frac{i_{\omega_1.\omega_2} U_0}{i_{\omega_2\pm\omega_1} + \sqrt{8 i_{\omega_1.\omega_2} i_{2\omega_2\pm\omega_1} - 3 i^2_{\omega_2\pm\omega_1}}}$$

(14) $$\beta_a = \frac{i_{\omega_1.\omega_2} U_0}{-i_{\omega_2\pm\omega_1} + \sqrt{8 i_{\omega_1.\omega_2} i_{2\omega_2\pm\omega_1} - 3 i^2_{\omega_2\pm\omega_1}}}$$

The causality factors are defined in the following forms:

$$Casualityfactor(2): \frac{i_{\omega_2\pm\omega_1}}{i_{2\omega_1}} \text{ and } Casualityfactor(3): \frac{i_{2\omega_2\pm\omega_1}}{i_{3\omega_1}}$$

where the following relationships exit among the harmonic and intermodulation components:

(15) $$i_{\omega_2\pm\omega_1} = i_{2\omega_1} = i_{2\omega_2}$$

(16) $$i_{2\omega_2\pm\omega_1} = i_{2\omega_1\pm\omega_2} = i_{3\omega_1} = i_{3\omega_2}$$